A Fully 3D-printed Integrated Electro-chemical Sensor System

by

Yue Dong

B.Sc., Simon Fraser University, 2015

Thesis Submitted in Partial Fulfillment of the
Requirements for the Degree of
Master of Applied Science

in the
School of Mechatronic Systems Engineering
Faculty of Applied Science

SIMON FRASER UNIVERSITY

Summer 2017

Approval

Name:	**Yue Dong**
Degree:	**Master of Applied Science**
Title:	A Fully 3D-printed Integrated Electro-chemical Sensor System
Examining Committee:	**Chair:** **Dr. Siamak Arzanpour, P. Eng** Associate Professor
	Dr. Woo Soo Kim, P. Eng Senior Supervisor Associate Professor
	Dr. Jiacheng (Jason) Wang Supervisor Assistant Professor
	Dr. Ash M. Parameswaran, P. Eng Internal Examiner Professor School of Engineering Science
Date Defended/Approved:	30 August 2017

Abstract

This thesis investigates the design, fabrication and characterization of a 3D printed electro-chemical sensor as well as compact potentiostat circuit on Printed Circuit Board (PCB) for portable electro-chemical sensing applications. Conductive 3D printing technologies are investigated as well as the advances in sensors and electronics applications. An optimized Directly Ink Writing (DIW) technique is adapted in a novel 3D-PCB fabrication platform using silver nanoparticle ink for electronics applications. An electrochemical device called potentiostat is designed based on an open source system. Its prototype is 3D printed on FR4 substrate. Using the same 3D platform, a lactate sensor which is comprised of 3-electrodes is printed on the flexible substrate. Together, the 3D printed system demonstrates the electrochemistry test including cyclic voltammetry (CV) and amperometry. Results of this research demonstrate that 3D-PCB technology can significantly accelerate the fabrication process of conventional electronics, and merge its capability into electrochemical applications.

Keywords: 3D printing; electrochemical devices; biosensors; 3D printed circuits; flexible printed circuits

I would like to dedicate this thesis to my loving family

Acknowledgements

I wish to thank my advisor, Dr. Woo Soo Kim, for his support on this project, as well as the other members of my thesis committee.

To the staff of the SFU MSE department, a heartfelt thank you for all of your hard work keeping the program operating.

Finally, it has been an honor working with all of the other members of the stretchable devices laboratory, and our many conversations, on topic or off, were always a pleasure.

Table of Contents

List of Tables

List of Figures

List of Acronyms

ABS	Acrylonitrile Butadiene Styrene
ADC	Analog To Digital Converter
AgNW	Silver Nanowire
AgNP	Silver Nanoparticle
AuNP	Gold Nanoparticle
BSA	Bovine Serum Albumin
CAD	Computer-Aided Design
CE	Counter Electrode
CV	Cyclic Voltammetry
DAC	Digital To Analog Converter
DIW	Directly Ink Writing
FDM	Fused Deposition Modeling
GA	Glutaraldehyde
GUI	Graphical User Interface
LOD	Lactate Oxidase
LOM	Laminated Object Manufacturing
PA	Polyamide
PBS	Phosphate Buffer Saline
PC	Polycarbonate
PCB	Printed Circuit Board
PDMS	Polydimethylsiloxane
PET	Polyethylene Terephthalate
PLA	Polylactic Acid
PU	Polyurethane
RE	Reference Electrode
SLA	Selective Laser Apparatus
SLS	Selective Laser Sintering
SMD	Surface Mounted Devices
STL	Stereo Lithography
WE	Working Electrode

Chapter 1.

Introduction

The applications for 3D printing, also known as additive manufacturing (AM) are exploding since 3D printing technology was first introduced in 1984 with the invention of an innovative stereolithographic device by Charles Hull [1]. However, it was not until the commercialization of 3D Systems' stereolithography (STL) based 3D printer that commercial 3D printers began to take off [2]. Following this, several other technologies for AM were commercialized including Laminated Object Manufacturing (LOM) and Selective Laser Sintering (SLS) in 1986, and Fused Deposition Modeling (FDM) and MIT's inkjet binder-based 3D printing in 1989 [2-3]. As new and more advanced technologies have emerged, the possibility to produce end-use productions on AM systems has become a reality, and the potential to create designs that are impossible to produce through other means has emerged. The process of 3D-printing starts with the creation of a virtual model of the object to be printed. This can be achieved by using computer-aided design (CAD) software, a three-dimensional scanner, or using photogrammetry where the model is obtained through the combination of several images of the object taken from different positions. Once the 3D model is created, it needs to be converted to the STL file format which stores the information of the model's surfaces as a list of coordinates of triangulated sections. This file format is universally recognized as it can be read by all 3D printer software, which then converts the data to a G-code file after a slicing process. The slicing procedure consists of the generation of several 2D cross section layers of the entire object. Finally, the printer starts depositing the material following the successive sequencing of such 2D layers, which are printed on top of the other, until the desired 3D object is created [4].

3D-printing enables almost unlimited possibilities for rapid prototyping and even massive manufacturing in some specific applications, such as fabricating thermofomring unit. Therefore, it has been considered for applications in numerous research fields such as mechanical engineering, medicine, and chemistry. Electrochemistry is one of the potential applications that can certainly benefit from 3D-printing technologies, paving the way for the design and rapid prototype of cheaper, higher performing, and ubiquitously

available electrochemical devices include sensor elements and backend electrochemical measurement electronics. Electrochemistry is the branch of physical chemistry studies the relationship between electricity, as a measurable and quantitative phenomenon, and identifiable chemical change [5]. The modern electrochemical system consists of two major parts: an electrochemical cell/sensor and an electrochemical signal acquisition electronics. Developing such electronics system usually take months or even years of time. Developers have to work from designing to prototyping back and forth in several cycles; it is a very time-consuming process. Particularly during the prototyping stage, the developer needs to send their design to off-site manufacturing service and the waiting periods are quite long. Therefore, prototyping efficient can be significantly increased by 3D printing technology if it has capability to fabricating both the electronics device and electrochemical sensors.

Usage of 3D printing for electronics device still remains largely unexplored, mainly because the lack of capability to fabricate the printed circuit boards (PCBs). A PCB is used primarily to create a connection between components, such as resistors, integrated circuits (ICs), connectors [6]. Together they deliver the functionality in any electronics today. Not surprisingly, the 3D printed electronics industry is in its early stage, more or less at the same level of adoption as regular 3D prototyping was in 2009 [7-8]. The slow adoption is not from a lack of interest or need; instead, it is because creating 3D printing technology for PCBs is exceedingly complex and previously developed 3D printing method did not solve these challenges. A suitable method and printer must be able to print conductive traces, which is the domain of printed electronics and produce components that meet the demanding performance requirements of consumer electronics, internet of things and even wearables.

1.1. Motivation

According to the 3D PCB printer readiness survey which garnered responses from nearly 300 electronics manufacturers and designers around the world [9]. 16% of respondents said their companies spend more than $100,000 each year on PCB prototypes, and 17% spend between $50,000 and $100,000. 44% of respondents noted PCB spending of between $10,000 and $50,000 annually. Just 23% of respondents said their companies spend less than $10,000 on PCB prototyping each year. 93% of all survey participants said their companies work with short-run, low-volume external PCB

prototyping services at some point each year. 62% of survey respondents noted the PCBs which their companies create and use have high layer counts, which means their designs are more complex and the PCB prototyping process is expensive. 63% of the survey respondents worry about the security of their intellectual property when they send out their designs to third parties for prototyping. Other concerns companies typically cite when sending their prototype designs to outside firms include turnaround time, expenses, and potential delays in getting their products to market, particularly if prototypes need to be reworked several times [9-10].

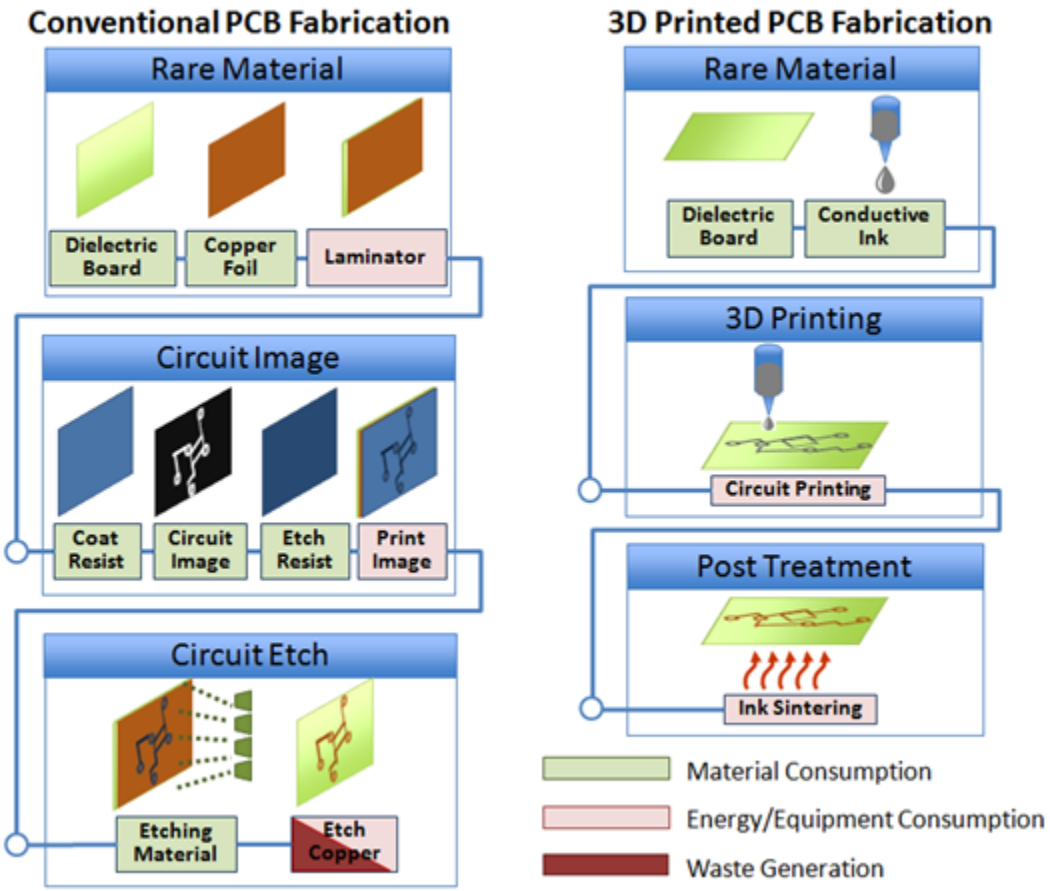

Figure 1.1 Fabrication comparison between conventional PCB (left) and 3D PCB (right)

According to the big data from this research, the global market for electronics contract manufacturing (ECM) services reaches almost $560 billion by 2016 and $845 billion by 2021. The conventional PCB manufacturing method first laminates copper foil on both sides of a dielectric substrate which mainly contain glass-reinforced epoxy. This requires machining and lamination processes. Next, multiple chemicals resists mask

layers with designed circuit pattern are applied on the copper foil layer via lithography method. Finally, chemical etching process removes the exposed copper area to form the circuit trace (Fig. 1a). This subtractive manufacturing process is well-known as an energy-intensive and chemical-intensive industry, which involves many chemical processes and materials that are potentially harmful to the environment. To the developers, it is expensive, time-consuming, and it puts intellectual property at risk. There is a huge demand now for engineers to print their quality PCB prototypes in-house cheaply and quickly. The possibility of using 3D printing to create professional PCBs offers manufacturers the flexibility of printing their circuit board prototypes in-house for rapid prototyping, R&D, or even for custom manufacturing projects [11].

While it is unlikely that 3D printing technology for electronics will replace all of the traditional processes for in-house development of high-performance electronic device applications, they will be particularly useful for prototyping. Researchers and manufacturers adopting this 3D printing technology can expect a variety of gains, including cutting their time to market with new products and speeding iterations and innovation around PCBs. With a 3D PCB printer, they can even build and test PCBs in hours. For many, one of the most exciting developments in this technology is that they will no longer need to send out their intellectual property to be manufactured off-site by specialist contractors, which essentially put their IP at risk. For others, the promise of rapid prototyping, significant reductions in the development costs and increased competitive edge are the most important benefits (Figure1.1). And perhaps most importantly, 3D printing for circuit boards offers nearly limitless design flexibility.

Electrochemistry bio-sensing systems enable continuous monitoring of individual's physiological biomarker such as glucose and lactate [12-20]. They provide useful information related to human physiological and metabolical status. Thus, the electrochemical sensor system has become spotlighted recently combined with increased interest in personal healthcare technologies. Portable biosensors have become essential to the world of medicine, a need that materialized due to an ever increasing population and as a means to provide health care to all. Leland Clark of the Children's Hospital Research Foundation in Cincinnati developed the first glucose biosensor in 1962, but it was not until 1975 that his discovery was commercialized [12]. As such, the development of new biosensors for disease detection is of great interest. Electrochemical information is conventionally acquired via the clinical point-of-care system. However, such systems

do not support continuous and real-time measurement due to lack of portability and high manufacturing cost [13-15]. Moreover, any electronics system including an electrochemistry system typically undergoes several re-designs and transformations of circuits and sensors before becoming available for the accurate monitoring. To small companies and lab searchers, these steps are a time-consuming significant obstacle for their projects.

As previously mentioned, development of the electrochemical system can certainly benefit from the use of 3D-printing technologies because they facilitate the construction of custom made complex measurement systems not only due to the fast prototyping of analyzing the circuit. Also, 3D-printing can be employed to produce a conductive sensor with complex shapes or compositions to be used for redox and catalytic processes and build liquid handling systems, such as voltammetric cells or microfluidic systems, which can then be combined with electrodes. A sensor is an object that detects events or changes in its environment and sends the information to other electronics, such as a computer. The 3D-printing process can be started and stopped to incorporate complementary fabrication processes or to embed subcomponents manufactured using traditional methods. Thus, the 3D-printed sensors can be fabricated by either embedding a sensor into printed structures or intrinsically printing the entire sensor [21]. A large amount of current research on 3D-printed sensors has focused on selected areas such as force, motion, optics, etc. Unlike force or motion sensors, which normally use capacitance change as the transduction mechanism, an electrochemical sensor requires much complex material for transduction. The ability of 3D print technology to achieve this function is critical to delivering electrochemistry application.

1.2. Objectives

This research project aims towards integration of 3D printing technology with prototyping of a portable lactate electrochemical system that could perform electrochemical measurements for the purpose of medical diagnostics. The objectives of this projects are as follows:

1. To design a fabrication metod for single layer double sided PCB using 3D printing technology
2. To design and develop a portable electrochemical system known as a potentiostat which can measure current from a lactate biosensor
3. To develop a 3D printed flexible electrode on the thin substrate for monitoring lactate concentration utilizing perspiration.
4. To fabricate the potentiostat on 3D-PCB and characterize the 3D printed potentiostat performance compare with a circuit using traditional PCB method.
5. To verify the capability of 3D fabrication for electronics applications by demonstrating voltammetry and amperometry tests for lactate measurement

1.3. Contribution

For this work, Stretchable Devices Laboratory (SDL) at Simon Fraser University has expanded on the research in 3D printing technology for printed circuit boards, flexible sensor electrodes, and application of electrochemistry. This work lays the foundation for further fabrication optimization of 3D-PCB for complex electronics. The immobilization procedure of enzyme for working electrode and method for incorporating the in-sensor reference electrode was originally contributed by previous lab memebers in “Bendable Electro-chemical Lactate Sensor Printed with Silver Nanoparticles” by Md Abu Abrar [22]. In this work, 3D printing of sensor electrodes and 3D-PCB based potentiostat circuit was successfully demonstrated. This work has also been submitted to the journal of *IEEE Sensors*: Y. Dong, and W. S. Kim, “A Fully 3D-printed Integrated Lactate Sensor System.”

1.4. Thesis Organization

The research presented in this thesis focuses on the design and fabricate a 3D printed portable potentiostat system as well as the flexible lactate sensor electrodes to achieve electrochemical analysis of lactate acid. Chapter 2 provides an overview of electrochemistry background and 3D printing technology. Chapter 3 introduces the 3D PCB printing method, material, and platform. Followed with the design and 3D printing fabrication of the potentiostat as well as the flexible sensor electrode. Chapter 4 provides the verification of the 3D printed device's functionality and performance of the electrochemical test. Finally, Chapter 5 draws a summary of this work and provides insights into what steps to follow for a future opportunity for further improvement of the 3D-PCB printing.

Chapter 2.

Electrochemistry and 3D Electronics Printing

Electrochemistry can certainly benefit from the use of 3D-printing technologies because they facilitate the construction of custom made complex measurement systems with great versatility. To date, several 3D-printing technologies have been invented, each with methodology differing in the way the 2D layers of material are deposited. In order to merge the most suitable 3D-printing technology with PCB fabrication as well as electrochemical application, both fields must be fully understood. In this chapter, an overview of electrochemistry and its technology are provided. Next, the most commonly available 3D-printing methods are provided along with a review of recent developments in electronics and sensors adopting 3D-printing as a possible rapid prototyping fabrication tool.

2.1. Electrochemistry and its Application

The electron transfer plays the fundamental role in chemical reactions to produces the current pathway. Electrochemical methods offer the ability to investigate the speed and size of the electron movement directly by the detection of the electrical signals generated by a chemical reaction for analytical purposes [23]. Particular interests for electrochemistry are the redox reactions, whereby one molecule undergoes oxidation (releasing electrons), and the other undergoes reduction (gaining electrons). When both reactions are present within a single system, a spontaneous current can be generated. In its simplest form, two solid metals which are called an electrode, that is submerged in the same electrolyte solution. No reaction takes place inside the system until a conducting path joins the two electrodes. Then, the electrodes are connected via an external circuit through which the electrons may travel. Alessandro Volta invented the first battery in 1800 using the same structure by alternating stacks of copper and zinc disk separated by paper soaked in the acid solution. This setup is known as a voltaic cell [24] (Figure 2.1). The electrical energy released during the reaction always have a positive voltage. This electrochemical current produced between the two electrodes can be measured by a potentiometer or other analog measurement devices.

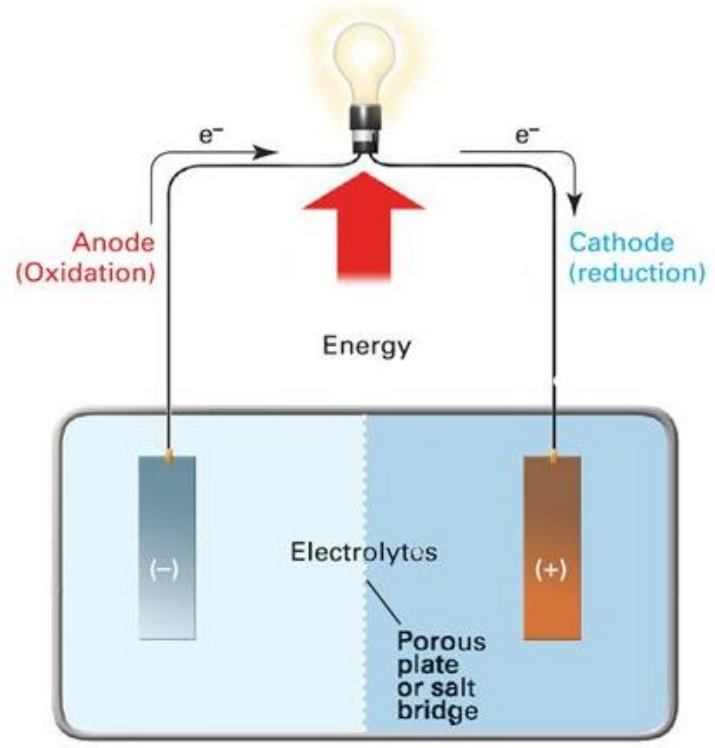

Figure 2.1. A voltaic cell transforms the energy released by a spontaneous redox reaction into electrical energy [24]. Licensed under by CC 3.0.

A voltaic cell consists of two compartments called half-cells. One half-cell where oxidation occurs is known as the anode. The other half-cell, where reduction occurs, is known as the cathode. The electrons in voltaic cells always flow from the negative electrode to the positive electrode, which is from the anode to cathode. The electrolyte solution contains cations of the electrode metal and anions to balance the charge of the cations. In principle, a half-cell contains a metal in two oxidation states; inside an isolated half-cell, there is an oxidation-reduction (redox) reaction that is in chemical equilibrium, the condition is written as follows equation:

$$O + ne^{-} \leftrightarrow R \tag{2.1}$$

where $[O]$ is the oxidized species, $[R]$ is the reduced species, and n is the number of electrons exchanged between $[O]$ and $[R]$.

In the voltaic cell, the reaction is spontaneous and always have a positive potential, such as a battery. On the contrary, the electrochemical cell is called an electrolytic cell where a current or potential must be applied to drive the chemical reaction (Figure 2.2).

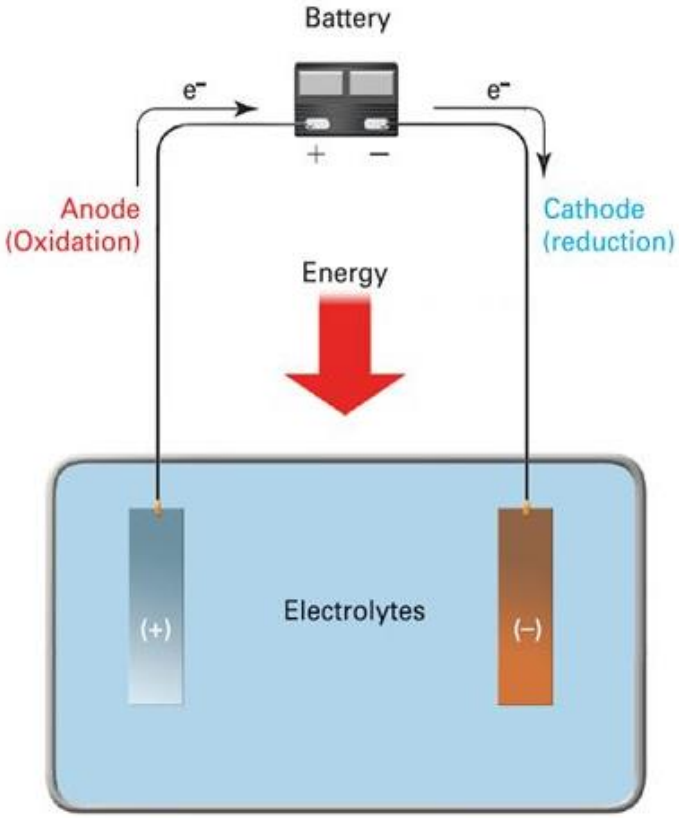

Figure 2.2. An electrolytic cell, an external electrical source is used to generate a potential difference between the electrodes that forces electrons to flow, driving a nonspontaneous redox reaction[24]. Licensed under by CC 3.0.

The electrochemistry deals with cell potential as well as the energy of chemical reactions. The energy of a chemical system drives the charges to move, and the driving force gives rise to the cell potential of the cell. The energy aspect is related to the chemical equilibrium, which is the relationship between the concentration of oxidized species [O], concentration of reduced species [R], and free energy ($\Delta G[J \cdot mol^{-1}]$).

$$\Delta G = \Delta G^0 + RTln\frac{[R]}{[O]} \tag{2.2}$$

where R is the gas constant (8.314 $J \cdot mol^{-1}K^{-1}$) and T[K] is the temperature. The critical aspect of this equation is that the ratio between reduced and oxidized species can be related to the Gibbs free energy change (ΔG), which the half-cell potential ($E[V]$) can be derived as

$$\Delta G = -nFE \tag{2.3}$$

here E is the maximum potential between cathode and anode electrodes, also known as the open-circuit potential (OCP) or the equilibrium potential, which is present when no current is flowing through the cell. F is Faraday constant. If the reactant and product have unit activity, and R is the reaction in the direction of reduction, then equation (2.3) can be written as

$$\Delta G^0 = -nFE^0 \tag{2.4}$$

This potential is known as the standard electrode potential ($E^0[V]$). As previously described, a voltaic cell always deliver a positive potential. It can be explained by the minus sign in the equation (2.4), thus spontaneous reaction in voltaic cell have a positive standard electrode potential ($E^0 > 0$). electrochemical cell has a negative standard electrode potential ($E^0 < 0$).

When combining equations (2.2) - (2.4). All these relationships are tied together in the concept of Nernst equation. Its mathematical expression describes the correlation between cell potential and concentration for a cell reaction as:

$$E = E^0 + \frac{RT}{nF} ln \frac{[O]}{[R]} \tag{2.5}$$

where $E^0$the standard electrode potential, *n* is the number of electrons transferred in the half-reaction, R is the gas constant, T is temperature, and F is the Faraday constant. At any specific temperature, the Nernst equation derived above can be simplified into a simple form. At the standard condition of 298 K (25°C), the Nernst equation becomes:

$$E = E^0 + \frac{0.05916}{n} ln \frac{[O]}{[R]} \tag{2.6}$$

With the know standard electrode potential (E^0), the resulting cell voltage (E) can be used to determine chemical composition in the reaction.

As previously mentioned, anodic currents are generated by ions (anions) diffusing toward the anode and cathodic currents by ions (cations) diffusing toward the cathode. The mathematical signs of currents and potentials measured at the anode and cathode depend on the type of electrochemical cell being investigated. For a reaction to occur spontaneously, certain conditions must be met, where the free energy change $\Delta G^0 < 0$ ($E^0 > 0$). When a chemical reaction does not occur spontaneously, the cell requires

external energy input in order to occur $\Delta G^0 \geq 0$ ($E^0 < 0$). This can be done by applying potential between electrodes

$$E_{cell} = E_{cathode} - E_{anode} \quad (2.7)$$

This process is called electrolysis [25]. During electrolysis, the applied potential can be controlled. The analyte is an electroactive species which can give up or accept electrons while interacting with the electrochemical cell's surface.

2.1.1. Electrochemical Cell

Working Electrode

An electrochemical cell consists of two electrodes regardless the type of cell. There is a working electrode (WE) where the half-cell corresponding to the reaction under study take place. The working electrode, typically a cathode, represents the most critical component of an electrochemical cell. The selection of a WE material is critical because electron transfers occur at the interface between the WE and the analyte solution. Several important factors should be considered. First, the material should exhibit favorable redox behavior with the analyte, ideally fast, reproducible electron transfer without electrode fouling. Secondly, the potential window over which the electrode performs in a given electrolyte solution should be as broad as possible to allow for the greatest degree of analyte characterization. Additional considerations include the cost of the material, its ability to be machined or formed into useful geometries, the ease of surface renewal following a measurement, and toxicity [25]. Common materials for working electrodes are platinum, gold, and various forms of carbon, such as glassy carbon and graphite. They are inert, and, therefore do not participate in the reaction; their sole purpose is to transmit electrons to and from entities in the solution. WEs sometimes can be chemically modified in order to increase their sensitivities toward specific species.

Reference Electrode

An electrolytic cell can have either two-electrode or three-electrode configuration. Regardless the configuration, it must contain a reference electrode (RE), typically an anode. It holds a stable potential during the redox reaction so that the resulting potential may be measured with respect to a known potential [25-26]. There are several types of reference electrodes such as Saturated Calomel Electrode (SCE), silver/silver

chloride(Ag/AgCl), mercury/mercurous sulfate (Hg/Hg_2SO_4) Mercury/Mercury Oxide, and Normal Hydrogen Electrode (NHE), etc. Mercury based REs possess their disadvantages because of using Hg which is not biocompatible. Hg/HgO could be used ideally for basic solutions. In many applications, even a small amount of electrolyte solution leaking from the reference electrode can immediately compromise the electrochemical reactions. Primary among these applications is non-aqueous electrochemistry. In these applications, it may be possible to use what is called a pseudo-reference electrode. The simplest pseudo-reference electrode is a metal wire, like platinum, inserted directly into the analyte solution.

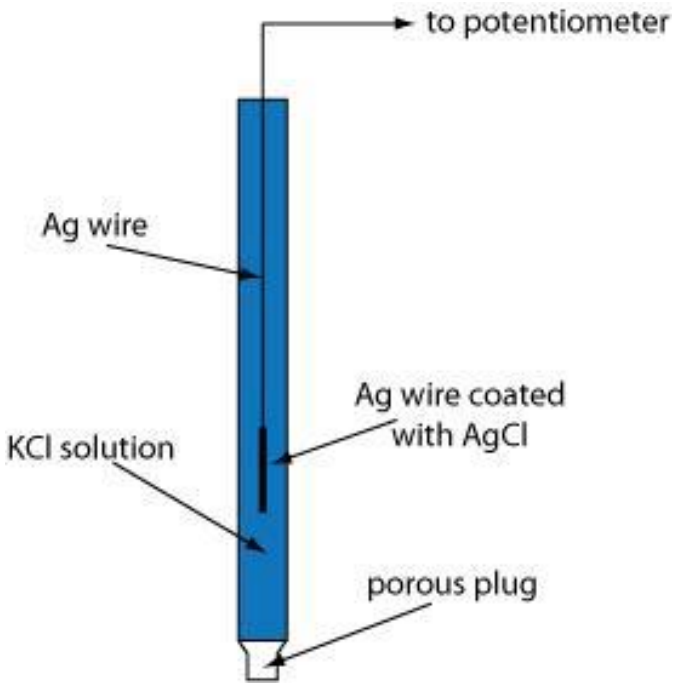

Figure 2.3. Schematic of an Ag/AgCl reference electrode [27]. Licensed under by CC 3.0.

The silver/silver chloride reference electrode is the most regularly used RE duo to its simplicity, inexpensive design and nontoxic components [27]. The simplicity of the Ag/AgCl lends many features to make it a great candidate to be used in biomedical and biosensor applications. Ag/AgCl electrode is a silver wire coated with silver chloride immersed in a rich Cl^- solution (typically saturated KCl solution). If an electron flows to the electrode, Ag^+ from AgCl coating is going to be reduced to Ag and Cl- dissolves into the solution (Figure 2.3). If electron flows in the reverse direction, Ag coated with AgCl will give up the electron to get oxidized to Ag^+ which later combines with Cl- from the solution to make insoluble AgCl. The controlling redox process is:

$$AgCl + e^{-} \leftrightarrow Ag + Cl^{-} \quad (2.8)$$

It has a standard potential $E^{0}_{Ag/AgCl} = 0.222V$ versus NHE (25 $^{\circ}C$) [22].

Counter Electrode

The only purpose of the reference electrode is to retain an essentially constant composition and therefore provides a stable potential. However, in most cases, REs can be damage by the presence of large current densities and may lose their ideal non-polarizable behavior. Therefore, a three-electrode configuration is often used in the modern electrochemical cell. The third electrode called counter electrode (CE) or auxiliary electrode (AE). The purpose of the counter electrode is to provide a pathway for current to flow in the electrochemical cell without passing significant current through the RE [28]. There are no specific material requirements for the electrode beyond it not adversely influencing reactions occurring at the working electrode (WE). Care should be taken that CE does not interfere with the WE reaction.

Thus when implementing a three-electrode configuration sensor as an electrochemical cell. A controllable potential is applied between the WE and RE during electrolysis, while a current run between the WE and CE is monitored. Studying the relationship between the current and potential, analyte solution can be characterized [28-29]. The device that applies this potential and monitors the resulting current is called a potentiostat.

2.1.2. Potentiostat

Simply speaking, potentiostats are amplifiers used to control a voltage between two electrodes (WE and RE) to a constant value or patterns. Figure 2.4 shows a principle schematic diagram for a potentiostat. The potential of the working electrode is measured relative to a constant-potential reference electrode that is connected to the WE through a high-impedance potentiometer E. To set the WE's potential constantly, a feedback loop control is essential. If the working electrode's potential begins to drift, the feedback amplifier can return the potential to its initial value. The current flowing between the CE and the WE is measured with an ammeter. Modern potentiostats include waveform generators that allow us to apply a time-dependent potential profile, such as a series of potential sweep pattern to the working electrode.

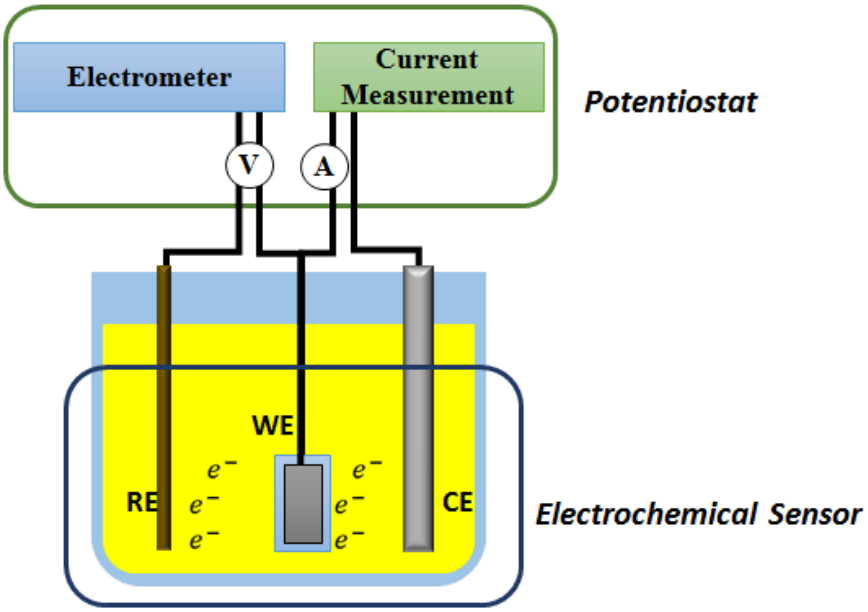

Figure 2.4. Schematic diagram of a general potentiostat and connection with an electrochemical cell

2.1.3. Method of Analysis

Electrochemical techniques can be classified into several categories depending on the experimental conditions and the analytical signal. In a static technique, no current is allowed to pass through the analyte's solution. Dynamic techniques, in which current is allowed to flow through the analyte's solution. Figure 2.5 provides one version of a summary highlighting the experimental conditions, the analytical signal, and the corresponding electrochemical techniques. Among the experimental conditions under control are potential or the current, and whether the analyte solution is stirred [29]. Among them, amperometry and voltammetry, in which we measure current as a function of a fixed or variable potential, are the most important quantitative electrochemical methods.

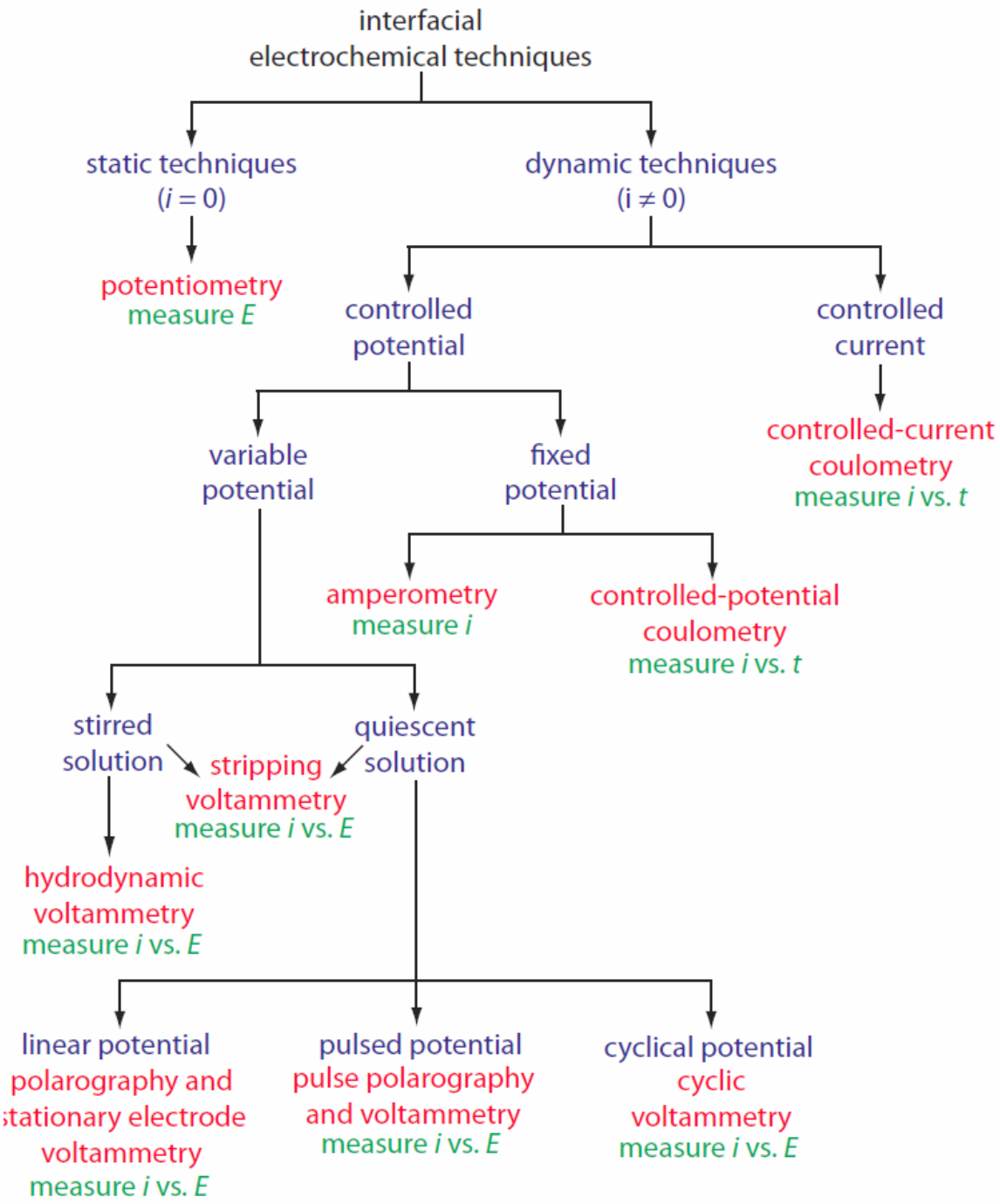

Figure 2.5 **Summary of interfacial electrochemical techniques. The specific techniques are shown in red, the experimental conditions are shown in blue, and the analytical signals are shown in green [24]. By LibreTexts is licensed under CC 3.0.**

Amperometry in biosensor is the study of the current response or change in current response based on analyte concentration when a certain potential is applied. For

electrochemical detections, amperometry could be defined as change in current response due to presence of electrons in the solution. Either way, it's the change in current response when a fixed step potential is applied. In general, amperometry is the measurement of electrode current between a pair of electrodes that are driving an electrolysis reaction. In this reaction, the reactants is the intended analyte and the measured current is proportional to the concentration of the analyte.

In order to grasp what is taking place in amperometry, the concept of how the current changes when a stimulus is applied must be understood. As previously described, Nernst equation predicts the relationship between the potential of an electrochemical cell and concertation of analyte species. When we oxidize an analyte at the WE, the resulting electrons pass through the potentiostat to the CE, reducing the solvent or some other component of the solution matrix. If we reduce the analyte at the WE, the current flows from the CE to the cathode. In either case, the current from redox reactions at the WE to CE is called a faradaic current. In an unperturbed solution, when a potential step is applied that causes as surface reaction to occur, the current decays according to the equation called Cottrell equation as [30]:

$$\mathrm{i} = \frac{nFAD_0^{1/2}C_0^*}{\pi^{1/2}t^{1/2}} \quad (2.9)$$

where D_0 is the diffusion coefficient for the species, A is the surface area of electrode, n is the number of electrons transferred per electroactive molecule or ion, C_0 is the concentration of the oxidized species in $\mathrm{mol/cm^3}$ and t is the time in seconds.

There are four major factors that effect the reaction rate and current at electrodes: (i) mass transfer to the electrode surface (ii) kinetics of electron transfer; (iii) preceding and ensuing reaction; (iv)surface reactions. The slowest process will be the rate-determining step [30]. As shown in Figure 2.6, the simple redox reaction may be considered as a set of equilibria involved in the migration of the reactant toward the electrode, the reaction at the electrode, and the migration of the product away from the electrode surface into the bulk of the solution [30].

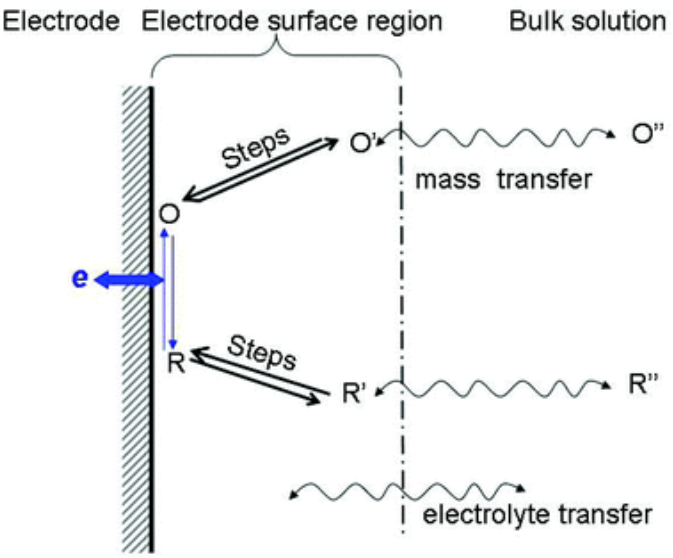

Figure 2.6. Close look of reaction at surface of electrode, both chemical transfer and mass transfer are involved [29]. Reprinted with permission.

Unfortunately, amperometry cannot determine the kinetics of the electron transfer and hence the kinetics of the reaction. That is, it cannot determine whether a surface confined or diffusion controlled reaction has occurred; information obtained from amperometry is limited compared to that of voltammetry.

On the contrary, voltammetry is an electrochemical technique to study current response as a function of applied voltage to the electrolytic cell; or in simple words- current response at varying potential. Cyclic voltammetry (CV) is perhaps the most versatile electroanalytical technique for the study of electroactive species and is often the first experiment performed in an electrochemical study of a compound, biological material, or an electrode surface. The effectiveness of CV results from its capability for rapidly observing the redox behavior over a wide potential range. The resulting voltammogram is analogous to a conventional spectrum in that it conveys information as a function of an energy scan. The cyclic voltammetry completes a scan in both directions in either to more positive potentials or more negative potentials. Figure 2.7a shows a typical potential-excitation signal; the potential is first scanned to more positive values, resulting in the oxidation reaction for the species R. This is known as forward scan in equation (2.2). When the potential reaches a predetermined potential value, the direction of the scan is reversed toward more negative potentials. The species O is generated on the forward scan, during the reverse scan it is reduced back to R. This is known as reverse scan in equation (2.1)

Because cyclic voltammetry is carried out in an unstirred solution, the resulting CV, as shown in Figure 2.7, has peak currents. As the voltage is decreased and swept towards the reduction potential of the system, electron transfer between the electrode and the oxidized species begins. This current continues to increase until a cathodic peak $i_{p,c}$ is observed, corresponding to a peak potential of $E_{p,c}$. Past this potential, the oxidized species becomes depleted and the current decreases [24]. The voltage is then reversed and swept towards the oxidation potential. This change in potential forces the reverse reaction whereby the reduced species becomes oxidized, resulting in an anodic current peak $i_{p,a}$ at $E_{p,a}$.

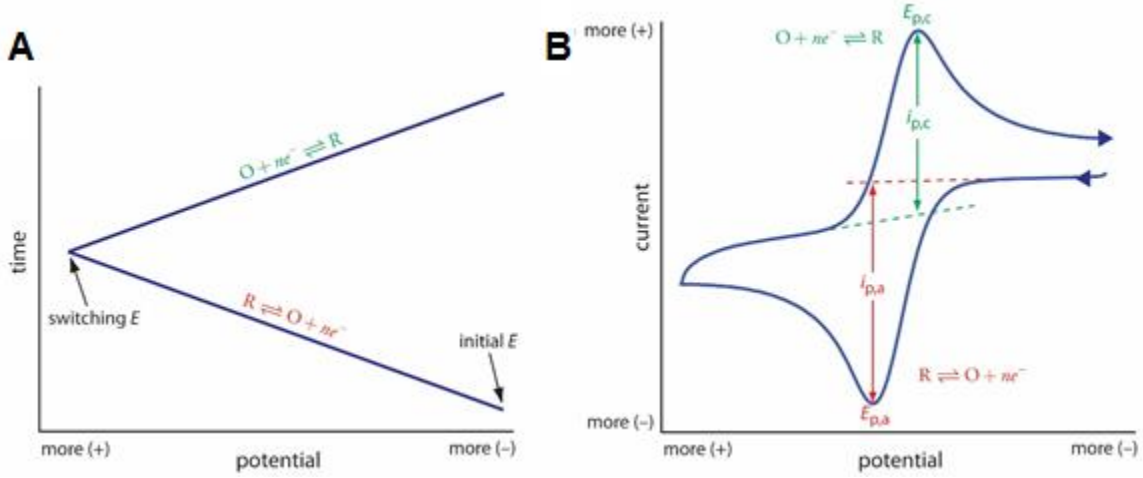

Figure 2.2.7. Typical potential sweep execution signal (A) and an ideal CV curve (B) [24]. By LibreTexts is licensed under CC 3.0.

The peak current in cyclic voltammetry can be predicted by Randles-Sevcik equation [29]

$$i_p = 2.69 \times 10^5 n^{3/2} A D^{1/2} C v^{1/2} \quad (2.10)$$

where n is the number of electrons in the redox reaction, A is the area of the working electrode, D is the diffusion coefficient for the electroactive species, v is the scan rate, and C is the concentration of the electroactive species at the electrode. For a well-behaved system, the anodic and cathodic peak currents are equal, and the ratio $i_{p,a}/i_{p,C}$ is 1.00. The half-wave potential, E_0, is midway between the anodic and cathodic peak potentials.

$$E_0 = \frac{E_{p,a}+E_{p,C}}{2} \quad (2.11)$$

Scanning the potential in both directions provides users with the opportunity to study the electrochemical behavior of species generated at the electrode. This is a distinct advantage of cyclic voltammetry over other voltammetric techniques. Figure2.8 shows the cyclic voltammogram for the same redox couple at both a faster and a slower scan rate. At the faster scan rate we see two peaks in Figure 2.8A. At the slower scan rate in Figure 2.8B, however, the peak on the reverse scan disappears. One explanation for this is that the products from the reduction of R on the forward scan have sufficient time to participate in a chemical reaction whose products are not electroactive [30].

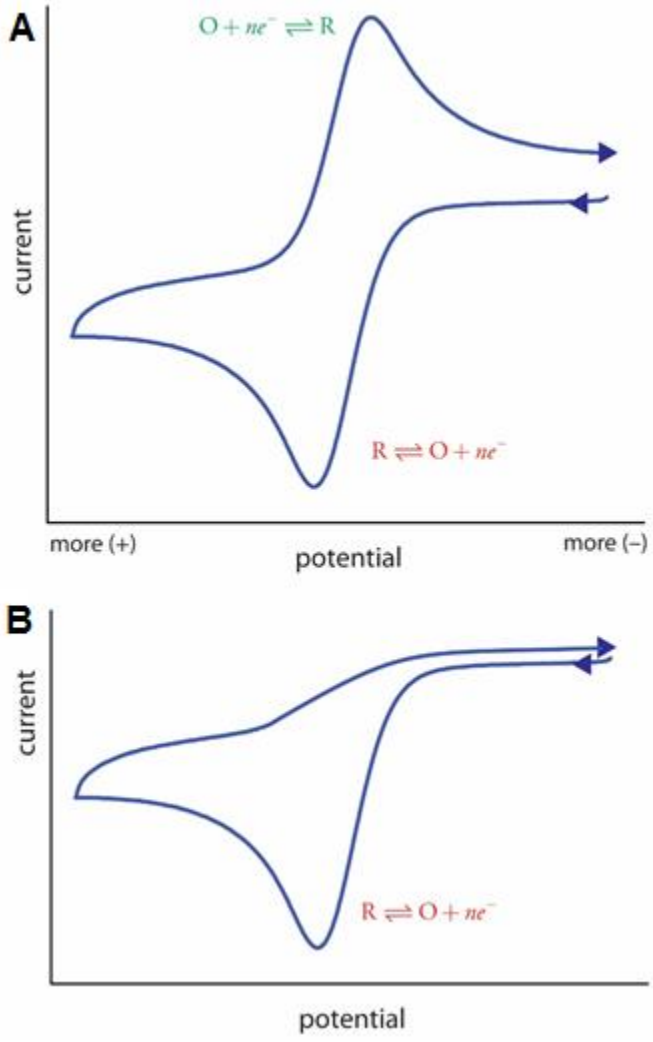

Figure 2.8. Cyclic voltammograms for R obtained at (A) a faster scan rate and (B) a slower scan rate [24]. By LibreTexts is licensed under CC 3.0.

2.1.4. Biosensor and Principle of Lactate Sensing

Biosensors are used for the detection of biological analytes, such as lactate. The development of the first biosensor is closely associated with the names of Leland C. Clark and Champ Lyons. Clark and Lyons created the first enzyme based glucose biosensor at the Cincinnati Children's Hospital in 1962 [31]. The primary structure of a biosensor includes two main elements, the biological element, and the transducer element. These two elements are connected to an electronic display that converts the signal into a readable format for the viewer. The biological recognition element (number 2 in Figure 2.9) detects the desired analyte (number 3 in Figure 2.9). The desired analyte can be any biological element, from nucleic acids to proteins. This is a selective element that should only detect the desired analyte [32-36]. The biological element is what drives the selection of the transducer element. The transducer converts the biological event into an electrical signal. The transducer element can be electrochemical or biological. Electrochemical transducers include nanotubes and nanoparticles while biological transducers include enzymes other biological components [37]. Transducers can be combined to strengthen the biosensor's signal. The signal is then amplified and sent to a display where it is processed into a readable format for the viewer to use.

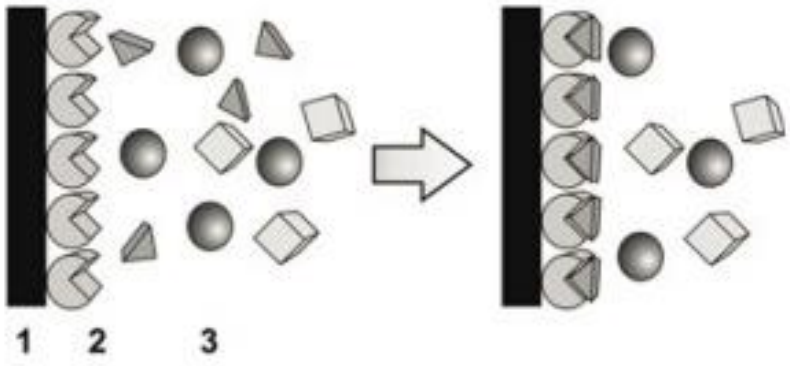

Figure 2.9. Illustration of the immobilized enzyme [29]. Reprinted with permission.

Lactate is the conjugate base of a lactic acid, also known as 2-hydroxy propanoic acid. Being produced continuously from pyruvate. Lactate plays a cardinal role in several biochemical processes. Hence lactate could be found in body fluids such as saliva [38], interstitial fluids [39], tear [40] and exhaled breath [41]. Lactate could as well be found in urine and sweat [42]. Sweat demonstrates a great prospect for continuous lactate measurement being easily accessible to offer real-time physiological information. Sweat

is composed of various dissolved salts, lactate, urea, amino acids, bicarbonate, etc. [43-48]. Human perspiration has been estimated to contain at least 61 different constituents with varying concentrations. During normal metabolism, eccrine sweat gland obtains ATP through oxidative phosphorylation. Under conditions such as ischemia or anaerobic metabolism, glycolysis becomes the main pathway to produce ATP and gives rise to lactate. The intensive exercise ends up leading to increasing in lactate production in sweat from ~10 mM to as high as ~25 mM [49-50]. Therefore, lactate sensors can be useful for measuring lactate level in sports medicine. The quest for non-invasive and continuous lactate monitoring led researches to search for utilizing alternative body fluids. In an article entitled, “Bendable Electro-chemical Lactate Sensor Printed with Silver Nanoparticles” by M. A. Abrar outlines a flexible amperometric biosensor based on silver nanoparticles for monitoring lactate concentration utilizing perspiration along with the demonstrate an immobilization procedure of enzyme [22]. Lactate oxidase (LOD) enzyme was used for lactate measurement due to its reaction simplicity and easy biosensor design. As the name suggests, Lactate Oxidase (LOD) is an enzyme which catalyzes lactate by oxidation to produce pyruvate. The enzyme can be reoxidized in the presence of O_2 to release hydrogen peroxide (H_2O_2). H_2O_2 gets oxidized at the electrode surface, restores O_2 concentration and gives a current proportional to the amount of lactate. Reactions involved in LOD-based sensor could be summarized as [22]:

$$L - lactate + LOD_{ox} \rightarrow pyruvate + LOD_{red} \quad (2.12)$$

$$LOD_{red} + O_2 \rightarrow LOD_{ox} + H_2O_2 \quad (2.13)$$

$$H_2O_2 \rightarrow O_2 + 2H^+ + 2e^- \quad (2.14)$$

The oxidation reaction of H_2O_2 that occurs on the electrode's surface allows the biosensor to detect the lactate concentration by the current it produces. The current given off by the electrode is linearly proportional to the H_2O_2 concentration. Because the enzymatic induced reaction has a one-to-one molar ratio of L-lactate and H_2O_2, the current recorded by the biosensor is also proportional to the detected the lactate concentration. Therefore, the lactate concentration is also linearly proportional to the current given off by the electrode.

2.2. 3D Printing Technologies for Sensors and Electronics

In this section, a brief review of existing techniques of 3D printing is introduced along with an overview of current 3D-printed sensors and electronics. The advantages and limitations in the different 3D fabricating processes are discussed in order to select the best method for 3D-PCB and sensor printing.

2.2.1. Current 3D Printing Technology

The 3D-printing process starts with a digital model of the object. Its digital virtual model can be generated using a three-dimensional scanner, computer-aided design (CAD) software, or by photogrammetric technology. Then 3D model needs to be converted into an STL file. This STL file contains a list of coordinates of triangulated sections which store the information about the model's surfaces. All 3D printer software can read STL files, and then slice the object to obtain a series of 2D cross section layers by a Z direction discrete approach. Finally, the desired 3D object is created using layer by layer printing. A specific 3D printing process is shown in Figure 2.10 [51].

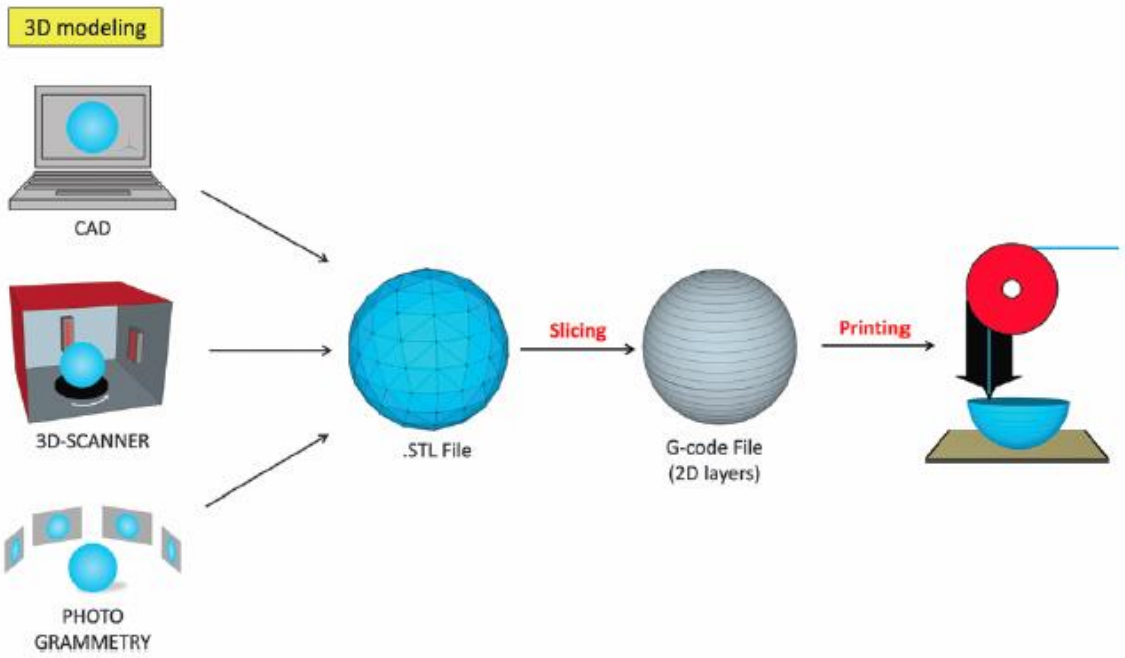

Figure 2.10. 3D-printing process. A digital model of the object is obtained through CAD software or 3D scanner. The 3D model design is then converted to the STL format to G-code file. Finally, the printer starts depositing the material following the layer-by-layer sequence [51]. Reprinted with permission.

Depending on the manufacturing principles and materials, 3D printing technologies can be divided into six main categories: fused deposition modeling (FDM), directly ink writing (DIW), laser-based stereolithography (SLA) and digital light processing (DLP), Laminated object manufacturing (LOM), laser sintering and laser melting (SLS, SLM), and photopolymer jetting (Ployjet) [52-63].

2.2.1.1 Fused Deposition Modeling (FDM)

FDM was first introduced by Crump [52]. The working principle of FDM 3D printers involves melting and extruding a thermoplastic filament through a nozzle (Figure 2.11). The melted material deposited on the fabrication platform then cools down and solidifies, and this process is repeated in a layer-by-layer fashion to build up a 3D structure. Thermoplastic materials such as polyamide (PA), polylactic acid (PLA), acrylonitrile butadiene styrene (ABS), polycarbonate (PC), etc. are usually employed and provided as a filament for FDM 3D printers [53]. FDM has been widely used for its low material cost and open source nature, but it is limited by its low printing resolution and slow printing speed.

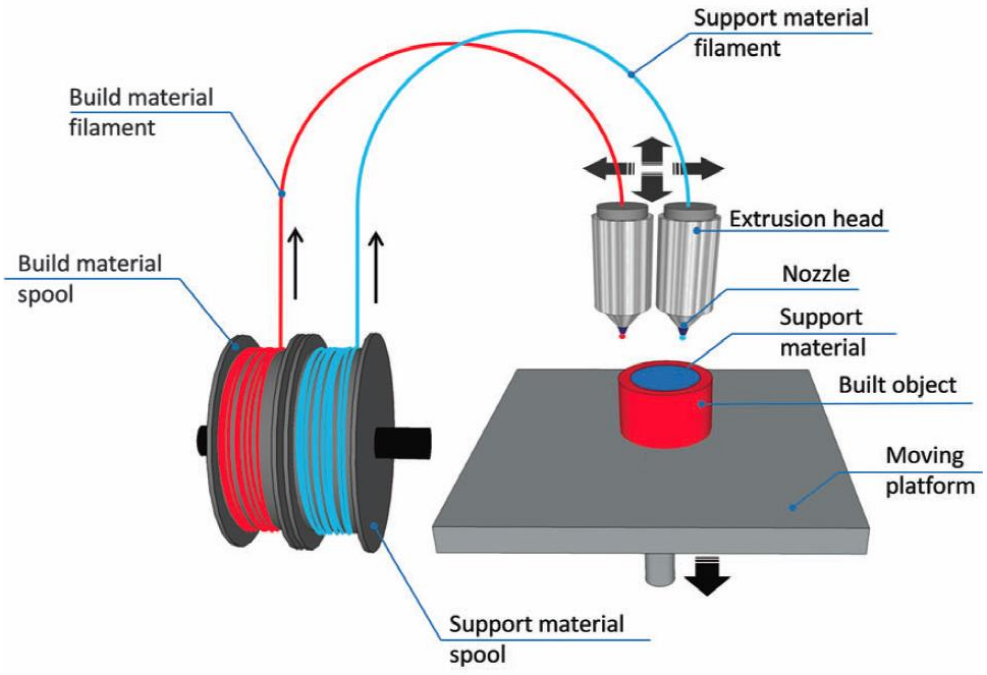

Figure 2.11. Schematic diagram of fused deposition modeling (FDM). A nozzle fed with a thermoplastic wire is moved in three dimensions across the building platform onto which molten voxels of a polymer are applied [51]. Reprinted with permission.

2.2.1.2Direct Ink Writing (DIW)

Direct ink writing printers use nozzles that directly extrude materials onto a fabrication platform (Figure 2.12). This technology allows the controlled deposition of materials in a highly viscous liquid state, which allows them to retain their shape after deposition. Direct ink writing technology is extremely versatile because a large variety of materials can be deposited, ranging from ceramics, plastics, foods, hydrogels and conductive ink [53-54]. The nozzle size, viscosity, and density of the material, scanning speed, eject speed, and other parameters can be adjusted to obtain an optimal deposition object. A post-fabrication process may need to harden the created object and improve its mechanical properties via sintering, heating, UV curing and drying step.

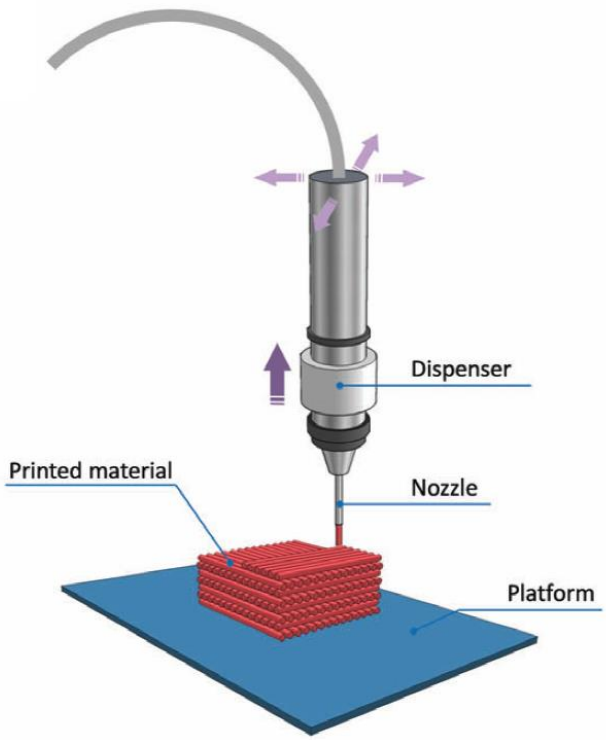

Figure 2.12. Schematic diagram of direct ink writing. A material dispenser connected to a computer-controlled robot, scans across the building platform, depositing the ink material in a layer-by-layer manner[51]. Reprinted with permission.

2.2.1.3. Photocuring (SLA, DLP)

Photocuring uses ultraviolet (UV) light to cure liquid polymers in a layer-by-layer manner, building 3D structures on the platform. There are two types of photocuring technologies: stereo lithography apparatus (SLA) [55] and digital light processing (DLP) [56].

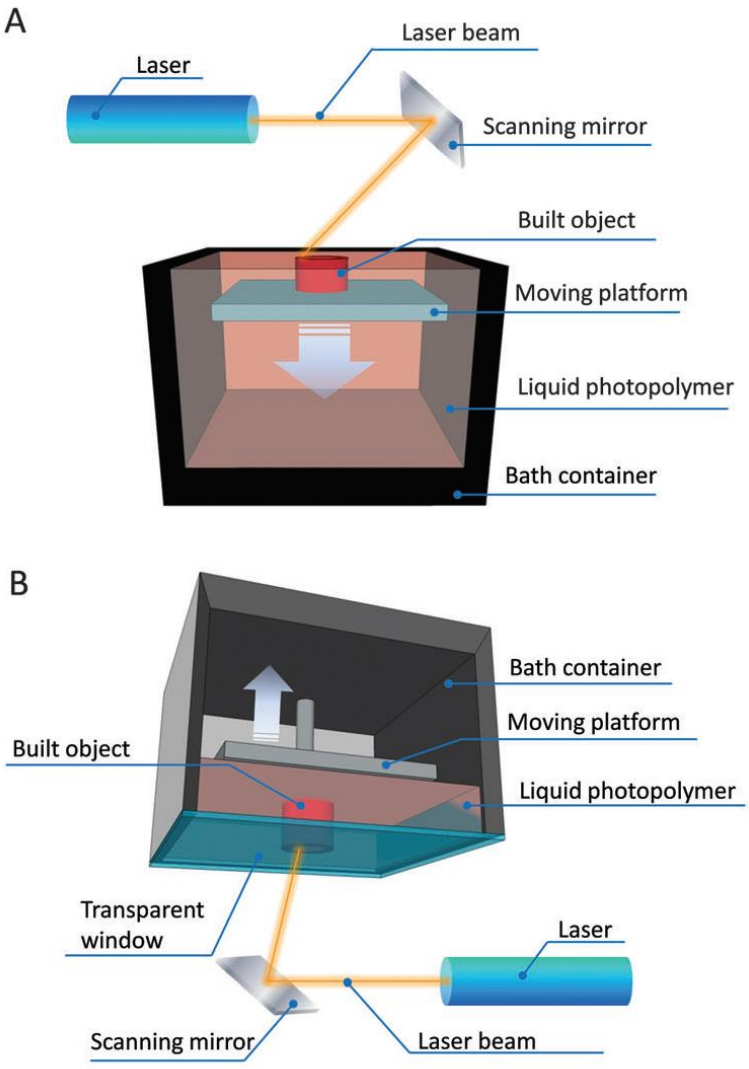

Figure 2.13. (A) Stereolithography (SLA) in a bath configuration where a laser beam is scanned across the liquid surface to polymerize the resin. Successive layers are created by lowering the movable table, allowing the fresh liquid resin to be exposed. (B) DLP in a layer configuration in which a laser beam is scanned from the bottom of the liquid tank through a transparent window. The polymerized layer attaches to the table, which is then moved upwards to refill the gap between the first layer and the window with fresh resin[51]. Reprinted with permission.

Figure 2.13A shows the fundamental principle of SLA. A tank is filled with a liquid photosensitive resin, which changes from liquid to solid when exposed to a certain ultraviolet light wavelength. The laser scanning of the layered cross section under the control of the computer leaves the layer cured. The cured layer is covered with a layer of the liquid resin after the platform reduces the height of a layer. [57]. Then a new layer is ready to be scanned, and the new cured layer is firmly glued on the preceding layer. The steps above are repeated until all the parts of the digital model are completed, and a 3D model is obtained. SLA cures the photosensitive resin by means of a moving laser directly, whereas DLP uses a laser or UV lamp as the light source. The light shines through special patterns on a digital mirror device, then the exposed parts are cured and a layer is finished. The platform rises a height of a layer and the next exposure period starts. A 3D solid model is obtained when all the layer have been exposed to the light [58]. Figure 2.13B shows the fundamental principle of DLP. The digital mirror device used as a dynamic mask is the main difference between SLA and DLP. SLA and DLP can produce highly accurate structures with complex internal features, but have the disadvantage of being limited to the use of a single-material.

2.2.1.4. Lamination (LOM)

Laminated object manufacturing (LOM) [59] uses lasers or knives to cut sheet materials. When a layer is cut, another sheet is added. The new layer can be firmly adhered to the completed parts by a roller that compacts and heats/glues the sheets together. The above steps are repeated until the process is completed. Finally, a 3D solid model is finished after removing the useless sections [59-60]. Figure 2.14 shows the fundamental basis of LOM system.

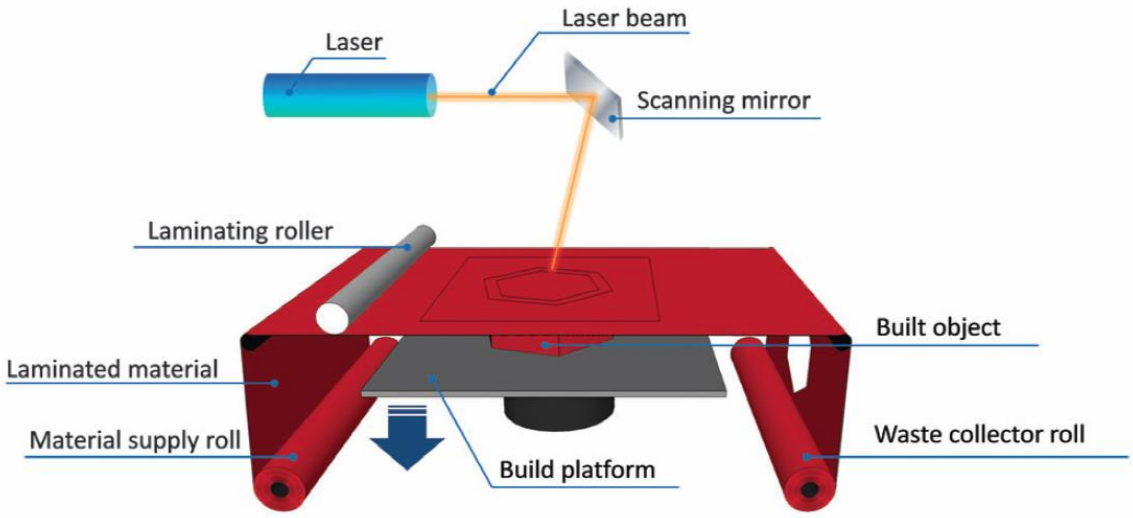

Figure 2.14. Schematic diagram of laminated object manufacturing (LOM). The first sheet of material is loaded onto the building platform. A PC-controlled cutting system consisting of a laser beam (or a mechanical blade) is then used to define the layer contour. Once the excess material is removed, a new sheet is loaded with a laminating roller which ensures good adhesion of the layers [51]. Reprinted with permission.

2.2.1.5. Selective Laser Sintering and Selective Laser Melting (SLS, SLM)

Selective Laser Sintering (SLS) [61] or Selective Laser Melting (SLM) [62], use powdery materials, mainly including plastics, metals, ceramics, and waxes. A layer of powder is laid on the workbench. A high-strength laser is used to scan the profile to melt and coat a layer of powder onto a fabrication platform (Figure 2.15). Following the sintering of one layer, the fabrication platform is lowered, and the powder is tiled on top of the previous layer before sintering the next layer. By repeating this process, the layers of the 3D structure are built up on the fabrication platform. SLA and SLM technologies can print things with high enough strength and density to meet aerospace or military standards.

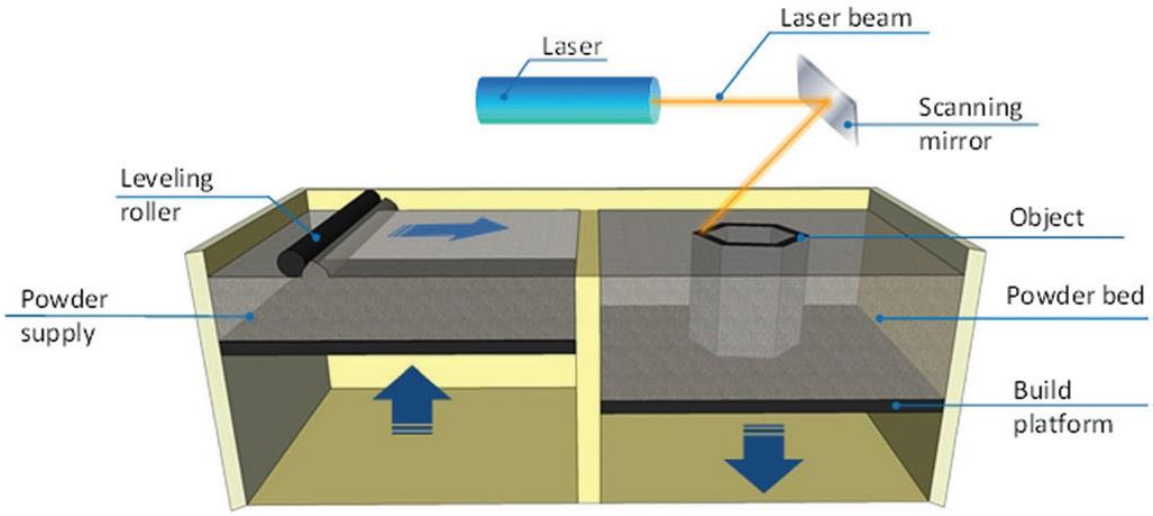

Figure 2.15. Schematic diagram of Selective Laser Sintering and Selective Laser Melting (SLS, SLM) [51]. Reprinted with permission.

2.2.1.6. Photopolymer Jetting (Ployjet)

Photopolymer jetting was originally introduced by Gothait [63]. For Ployjet, a photosensitive resin is used as printing material. This photosensitive resin is ejected from an inkjet nozzle and deposited on a mobile platform, then cured by UV light and solidified (Figure 2.16). This approach allows layer-by-layer fabrication. A 3D product can be obtained after curing all layers of the entire model. This method can print products with multiple materials and colors simultaneously. Ployjet is suitable for printing small and delicate objects due to its high-resolution. The strength of parts produced by this process is however weak.

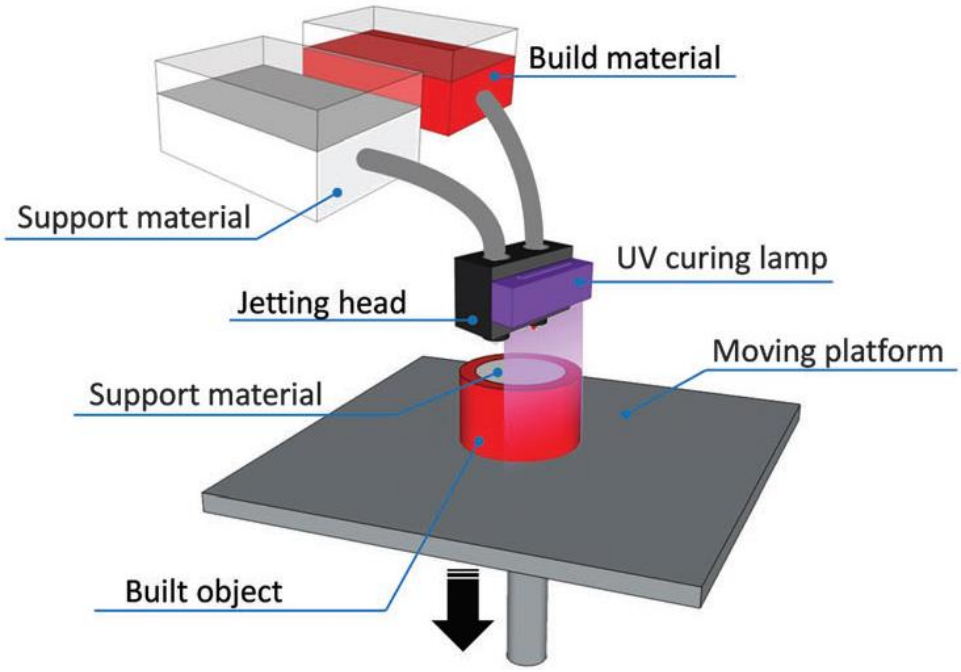

Figure 2.16. Schematic diagram of Photopolymer jetting (Ployjet) [51]. Reprinted with permission.

Table 2.1. Summary of each printing methods

Technique	Principle	Material	Advantage	Limitation
Fused deposition modeling (FDM)	Extrusion-based	Thermoplastics (ABS, PLA, PC, PA, etc.); glass (new); eutectic metal; ceramics; edible material, etc.	Simple using and maintaining; easily accessible; multi-material structures; low cost	Rough surface low resolution; high cost (for glass and metal)
Directly ink writing (DIW)	Extrusion-based	Plastics, ceramic, food, living cells, composites	Versatile	Low resolution; requires post-processing
Stereo lithography apparatus(SLA) & (Digital light procession)DLP	Photocuring	Photopolymers	High accuracy; simple	Single material; biocompatible
Laminated object manufacturing (LOM)	Lamination	Sheet material (paper, plastic film, metal sheets, cellulose, etc.)	Versatile; low cost; easy to fabricate large parts	Time-consuming; limited mechanical properties; low material utilization; design limitations
Selective laser sintering(SLS) Selective laser melting(SLM)	Powder based laser curing	Powdered plastic, metal, ceramic, PC, PVC, ABS wax, acrylic styrene, etc.	High accuracy; wide adaptation of materials; high strength	Limited mechanical properties; high cost
Photopolymer jetting(Ployjet)	Inkjet-based	Liquid photopolymers	High accuracy	High cost

2.2.2. 3D Biosensor Applications

Table 2.2. Summary of 3D-printed sensors

Application of Sensor	Method	Material	Transduction Mechanism	Ref.
Strain sensors	DIW	Carbon-based ink	Resistance	[64]
	LOM	Silicone rubber	Resistance	[65]
	DIW	Graphene aerogel	Resistance	[66]
Pressure sensors	FDM	ABS-based material	Capacitance	[67]
	FDM	PVDF	Capacitance	[68]
	FDM	ABS	Optical absorbance	[69]
Accelerometers	3DP	Silver nanoparticles	Capacitance	[70]
	FDM,SLA	Thermoplastics	Gravity	[71]
EEG sensors	FDM	PLA, ABS	Resistance	[72]
	FDM	PLA	Resistance	[73]
Antennas	DIW	Silver nanoparticle ink	RF reception	[74]
	FDM	Dupont 5064H	RF reception	[69]
	3DP	EPOLAM resin	RF reception	[75]
	SLA	Steel	Patch antenna	[76]
	inkjet	Silver nanoink	Patch antenna	[77]
Biosensors	DLP	Spot-A materials	Chemiluminescent	[78]
	DIW	PDMS, Hydrogel	Resistance	[79]
Temperature sensors	Inkjet printed	Exfoliated graphite and latex solution	Resistance	[80]
	SLA	Photopolymer	Electro-chemiluminescence	[81]

The greatest difference between biosensors and other sensors is that the signal detection of biosensors contains sensitive layers such as an enzyme. In recent decades, we have witnessed a tremendous number of activities in the area of biosensors. Due to characteristics such as intelligence, miniaturization, and specificity, biosensors offer exciting opportunities for researchers and corporations in applications from situ analysis to home self-testing. The biomaterial patterning of biosensor fabrication is one of the most promising techniques for improving biosensor stability. 3D-printing technology is reliable and efficient for facilitating controllability over the entire process and represents an authentic breakthrough for the development and mass production of biosensors. A detailed summary of 3D sensors including 3D printing technologies, transduction mechanism, application, printing materials is listed in Table 2. Among them, flexible electrochemical sensors were reported previously fabricated by conducting polymers inorganic, and carbon nanotubes [82-88] have been reported. Conventional fabrication approaches mostly involve screen-printing which produce electrode pattern. A flexible amperometric lactate biosensor using silver nanoparticle (AgNP)-based conductive

electrodes have been reported. This biosensor is designed and fabricated by modifying silver electrode with lactate oxidase immobilized by bovine serum albumin (BSA). The silver electrodes are fabricated via stamping in conjunction with a simple spray coating of AgNP ink [88]. AgNP inks normally have low resistance in order of $10^{-6}\Omega/cm$ [84]. Figure 2.17 summarizes conductivity of conductive materials including bulk silver, copper, and solder alloy which are not easy to be adapted in 3D-printed electronics. AgNP inks show a great potential in 3D-printing.

2.2.3. 3D Electronics Applications

3D printing technologies have also been expanded to electronics field as early stage. Previous works such as inkjet printing, directly fused deposition modeling (FDM) [89], and 3D molded interconnect device technology (3d-MID) [90]. Several 3D technologies have been demonstrated for patterning of electronic circuits. The combination of direct writing of conductive inks onto solid freeform fabricated structures was introduced by Palmer et al. [91] and Medina et al. [92], in which modest circuits were implemented to demonstrate functionality by integrating a dispensing system into a stereolithography (SL) machine using 3D linear stages with a dispensing head. Lopes et al. [92] demonstrated a simple prototype temperature sensor with nine components including an integrated circuit in a low-pin-density package, and in the same fashion. Others have demonstrated a similar circuit as well as several clever electromechanical applications all created by an open-source fabrication system [91–93]. Navarrete et al. [93] described improvements to conductor density by introducing channels into the SL substrate for containing the conductive material in order to reduce the possibility of line-to-line shorting and improve the cross-sectional area for improved performance. Line spacing was thus controlled by the precision of the SL laser beam as opposed to the dispensing system. Additionally, this demonstration included not only digital logic and control but also radio frequency (RF) wireless functionality [94]. The system was implemented in the form of a hidden-in-plain site rock to highlight the possibility of fabricating a line of systems—each of which could be altered in CAD to provide unique form similar to a snowflake and aiding in the deception by providing irregularities among the sensor systems. Ram et al. [95] reported electronics embedded in 3D-printed metal structures. More recently, collaborative work performed by Stratasys and Optomec

reported the use of FDM with aerosol-sprayed conductors but used large pin pitch packaging [96, 97]. Most of the reported circuits to date fall into three categories:

Firstly, direct writing of viscoelastic conductive metallic nano materials such as silver nanoparticle ink to form passive RLC radio-frequency electronic in small-scale, which can be resonated into certain frequency bandwidth by varying printed RLC demission. Secondly, a hybrid additive manufacturing process involves the fused deposition modeling of the thermal plastic substrate structure, and direct embedding of a conductive material has been demonstrated. This type of AM technology can fabricate a substrate in any arbitrary form, while the embedded conductive material is used as electrical interconnects through the precise printing of conductive inks or wires to realize circuit traces between components. Thus, functional 3D-printed electronic devices can be achieved by utilizing this capability along with insertion of electronic components include microchips, batteries, and antennas. Thirdly, a conductive ink, in most cases, the conductive AgNP ink is ink-jetted or screen printed into desired flat circuit trace pattern on flexible substrates. Thus, the complex circuit design can be achieved by stacking multiple circuit layers through interconnecting vias. This process type is more accurately described as a 2D layered electronic device.

All the previously reported 3D-printed electronics from fabrication above technologies show the capability to perform electronic functions. However, the majority of these printed circuits are used for the very preliminary electronic task, such as blink LEDs [88-90], because little of these 3D-printed electronics actually realize sophisticated circuit design comparable to a conventionally embedded electronic devices. An electronic device typically composed of several ICs and passive components in a compact design includes a low power microcontroller unit (MCU), a power supply, a voltage regulator, a communication chip, and many inductors, resistors, and capacitors. In order to integrate these components, PCB with high density interconnect (HDI) based assemblies are commonly used to build such systems using small surface mount devices (SMD). Only a few of 3D-printed electronics PCBs have been demonstrated with a high density of ICs (Figure 2.18).

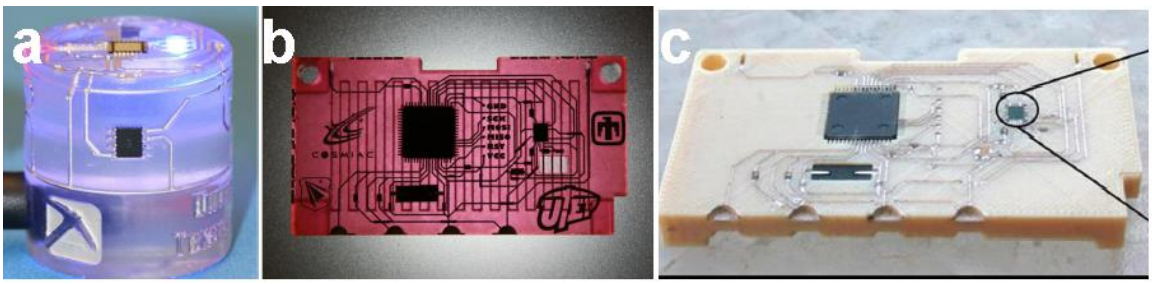

Figure 2.17. 3D printed electronics (a)magnetic flux sensor system with curved surfaces and modern miniaturized electronic components[98] (b)CubeSat 3D-printed module produced by using stereolithography and direct print technologies[98] (c) 3D-printed CubeSat module produced by using fused deposition modeling [98]. Reprinted with permission.

Given the tight dimensional requirements of electronic components including pin pitch and miniaturized package volume, the 3D-PCB fabrication technology must provide high spatial resolution. Whereas stereolithography has sufficient spatial resolution given the small beam width of the laser, FDM produces feature sizes at or larger than 254 μm and is not small enough to deliver circuit pad for regular IC components in electronics fabrication. For example, with a 0.65-mm pitch 144-pin TQFP package common in contemporary electronics, the chip cavity requires a flush encapsulation with pin features including 450-μm openings with 200-μm separation fins—to provide mechanical support and electrical access to the packaged silicon. Therefore, to provide the feature resolution necessary in the context of FDM fabrication, the multi3D system implements additional high-resolution subtractive methods. When conductive inks are still appropriate, the PCB substrate must have superior surface finish with minimal porosity—otherwise, the porosity will result in shorts between electrical lines as the conductive inks will spread before curing. Consequently, the multi3D system includes FDM build parameter for printing with improved density to maintain separation of conductive ink traces. In cases where the interconnect is required to provide high current densities with bulk level conductivity ($1.6810^{-6}\,\Omega/cm$ as a reference), wires can be introduced providing performance which is impossible to achieve with cured conductive inks (or even the solder-based approach described previously). In the multi3D system, wires are embedded with a novel patent-pending thermal embedding technique that submerges wires as small as 80 μm in diameter firmly into the thermoplastic substrates fabricated with FDM—leaving a planar surface to continue the interrupted fabrication process.

2.2.4. Conductive Nano-Material Printing

There are several challenges which should be overcome while using conductive NPs as the functional component of conductive inks. First, NPs in ink should be stable against aggregation and precipitation to provide reproducible performance. Therefore, the addition of a stabilizing agent, which is usually a polymeric material or a surfactant, is required. This stabilizer is especially important for dispersions with high metal loading, 20–60 wt%, which are required for obtaining printed patterns with a high density of metal to provide high conductivities.

Furthermore, NPs-based conductive inks should provide good electrical conductivity of printed patterns. It is obvious that the best candidates for conductive material are the highly conductive metals, such as Ag ($\sigma = 6.3 \cdot 10^{-7}\Omega/cm$), Cu ($\sigma = 5.96 \cdot 10^{-7}\Omega/cm$), Au ($\sigma = 4.42 \cdot 10^{-7}\Omega/cm$), and Al ($\sigma = 3.78 \cdot 10^{-7}\Omega/cm$). Currently, silver is the most reported material for conductive ink, and also the most utilized in industrial applications. Due to their high cost, a major challenge in this field is to replace silver and other noble metals with cheaper ones, such as copper and aluminum. This would depend on the success in avoiding their oxidation at ambient conditions, otherwise an inert atmosphere would be required.

Another challenge in using metallic nanoparticles is the need for a post-printing process in order to sinter the NPs for obtaining continuous metallic phase, with numerous percolation paths between metal particles within the printed patterns. This is usually an obligatory stage since the presence of stabilizing agents and other ink components prevents close electrical contacts of NPs due to the existence of organic insulation layers that surround the NPs. The conventional approach for sintering metallic NPs is heating. However, in the case of heat-sensitive substrates (e.g., paper, plastics), heating at temperatures above 120–150℃ is not applicable and, therefore, non-destructive methods of sintering are required.

Nanoparticles can also be used for effective electrical wiring of LDH or LOD enzyme for L-lactate detection. Various nanomaterials such as carbon nanotubes(CNT) and gold(Au) nanoparticles have been used as electrical connectors between the electrode and the redox center of the enzyme. A wide variety of nanoparticles has been used in lactate biosensors due to their advantage both regarding stability and in improving

the sensitivity. As a result of valuable properties of large surface- to-volume ratio, excellent surface reaction activity, high electro catalytic efficiency and highly adsorbing property, nanomaterials are an important candidate for enzyme immobilization in the fabrication of lactate biosensors.

Silver nanowires (AgNWs) and nanoparticles (AgNPs) have been extensively studied for fabricating stretchable electrodes lately. Silver (Ag) is known to be the best conductive metal, and it is also cheaper compared to noble metals such as gold or platinum. It is chemically more stable in air than copper and aluminum, syntheses of AgNWs and AgNPs have been well-established. The lower sintering temperature promotes easiness of a manufacturing process, for example, a sintering temperature of bulk gold is 1,063 °C while it is only about 130 °C with gold nanoparticles in 2 nm size Also, the addition of conductive nano-fillers in a polymeric matrix can provide an electrical property to the composite. Enormous kinds of conductive nano-composite composed of various fillers have been reported as an alternative for using conductive bulk metals or alloys thanks to the previously stated advantages brought by nanomaterials. Silver nanomaterials have been demonstrated to design and fabricate highly conductive electrode for stretchable electronics [101-107].

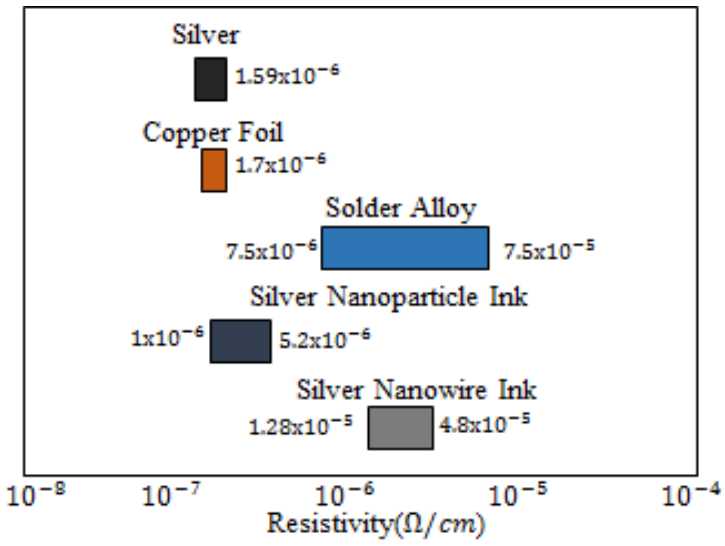

Figure 2.18. Electrical resistivity properties of conductive materials [101-107]

Chapter 3.

Development of 3D Printed Electrochemical System

After considering all the available 3D printing technology and studying previously reported 3D sensor and electronics PCBs. Direct Ink writing with AgNP was selected as the best candidate for 3D-PCB.

3.1. 3D Printing of Conductive Ink

The 3D printing system used in this research is a commercially available dispensing printer (V-one, Voltrea). It is originally designed as a fast prototyping tool for simple PCB. It consists of three parts: an XYZ axis linear motion platform and an embedded heat-bed with clampers (Figure 3.1).A lead-screw type paste extrusion head with replace syringe can be mounted on the carriage (Figure 3.2a). V-one has very limited motion range in Z axis (less than 500um). This is due to the PCB has only one layer of the conductive trace on the surface. The height can be neglected. An aluminum nozzle with 200um diameter is selected as the printing nozzle (Figure 3.2d) and is attached to the syringe head.

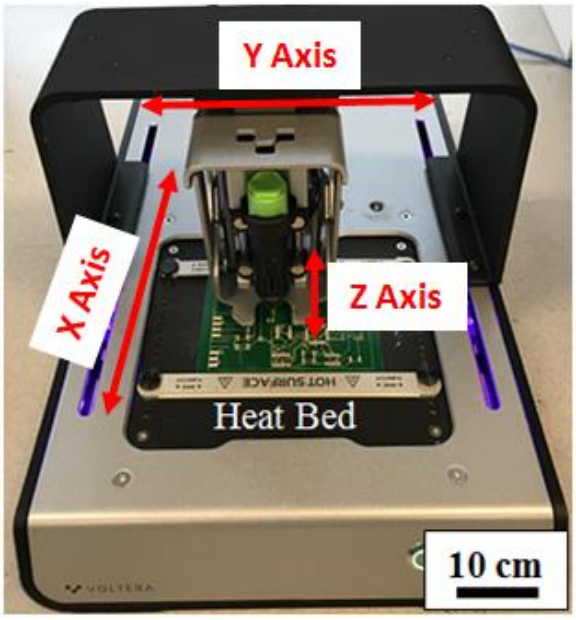

Figure 3.1. Voltera V-ONE direct ink printer

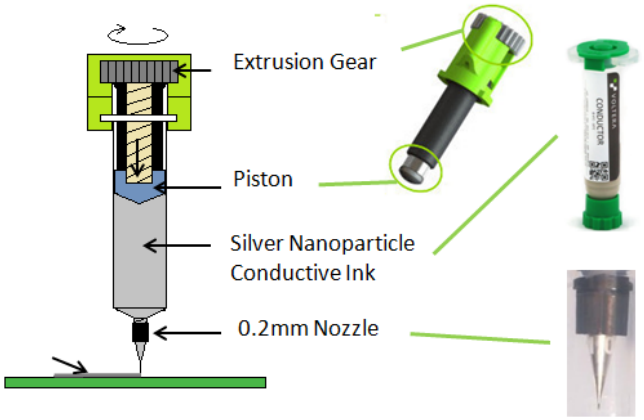

Figure 3.2. Direct ink writing mechanism detail

A silver nanoparticle ink is used as the conductive ink for printing. It has high electrical conductive and high viscosity. These properties ensure users can control the dispensed ink shape through a tiny nozzle. The control of the V-one printer is done with an interface software (Voltera). The purpose is to convert the conventional PCB Gerber file from any PCB design software to a machine recognized g-code. The user can import their PCB file, such as.GTL (Gerber top layer) and.TXT (drill file) to the Voltera interface software. Then the geometry design can be sliced depending on slice parameters (feeding and gap). As previously mentioned, the nozzle has 200 um diameter, which means the width of each single dispensed ink trace us 200 um. For regular PCB trace, average width is 12 mil, which is around 300 um. Thus one or two slices can be generated. For much bulk part, such as a large electrode and conductive pads, more slices is generated to fulfill the necessary area (Figure 3.3). The XYZ motion of extrusion head is executed by three servo motors via conveyor belt. The resolution of each axial motion is 50 um.

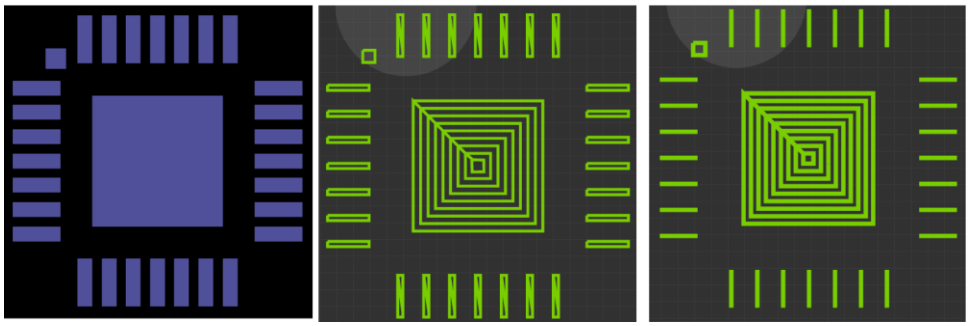

Figure 3.3. Voltera Software Slicing Feature of SMD circuit pattern (left) SMD QFN28 footprint (middle) sliced STI file with 0.15 line space (right) 0.1 line space.

3.2. Building Processes for PCB Printing

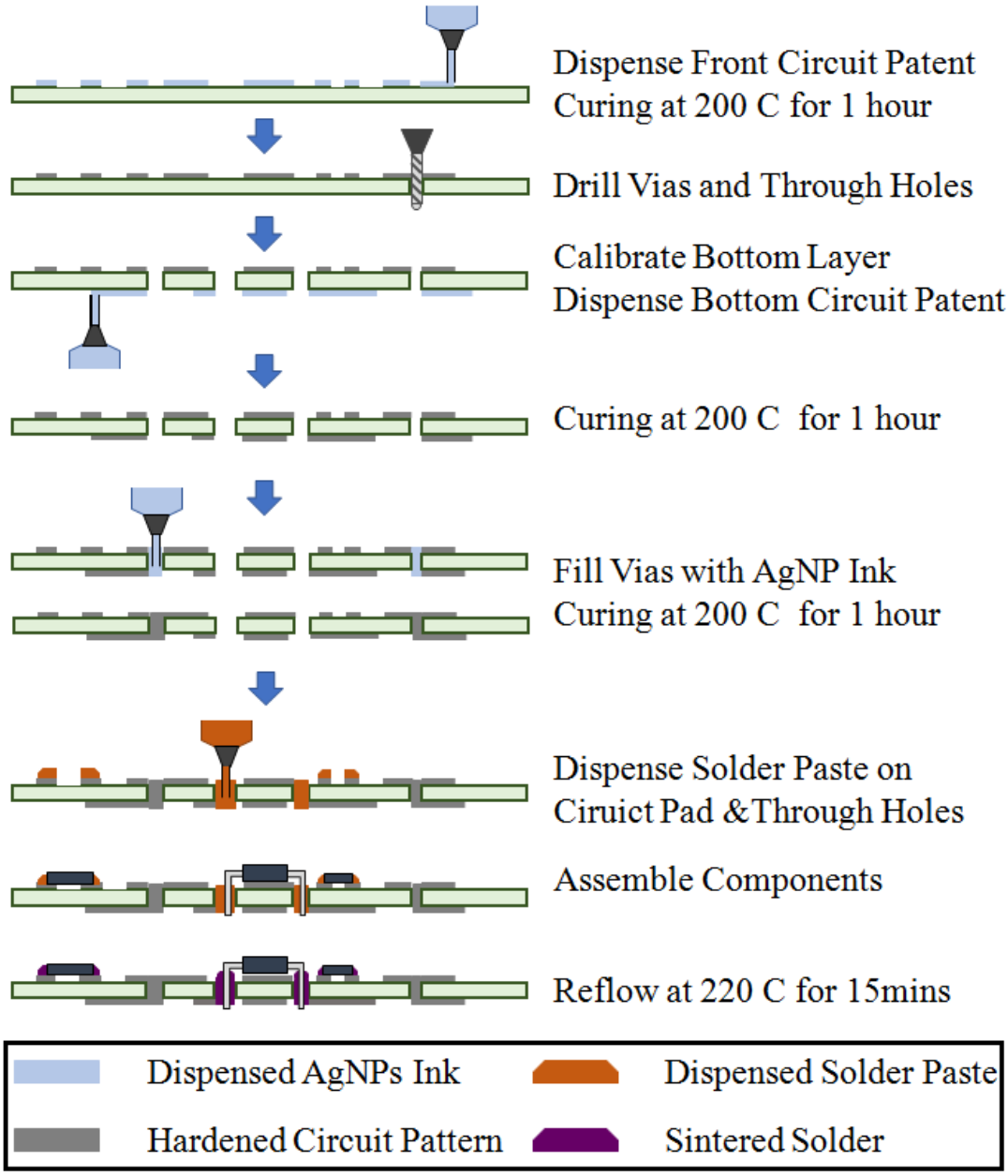

Figure 3.4. Flow chart of the additive manufacturing of- of 3D printed PCB

3.2.1. Pre-calibration

Considering a simple electronics with a single layer double sided PCB. There are several steps involved in 3D printing using V-one. After interface software converts PCB Gerber Top Layer file (GTL). A clean and flat substrate is placed and clamped on the heat bed area, no heat is applied at this moment. The detection probe is mounted XYZ motion platform first. The purpose is to calibrate the substrate surface height and position by contacting multiple checking points on the substrate surface. These checkings are all located on the path of circuit trace and pads. In this way, a temporary height profile in Z axis is generated in case the substrate is not flat (Figure 3.5).The second step is removing the probe and mounting the lead screw extrusion head with Ag conductive ink syringe. One thing should be noticed that all the air left inside of nozzle tip must be pushed out. Otherwise, it can cause discontinuity of printed ink. Manually rotating the lead screw can provide pressure inside of syringe. Thus conductive ink can be pushed out. However, too much pressure will cause excess ink keeping leaking. (Figure 3.6).Therefore extra attention must be paid.

Figure 3.5. Calibration procedures for substrate height profile

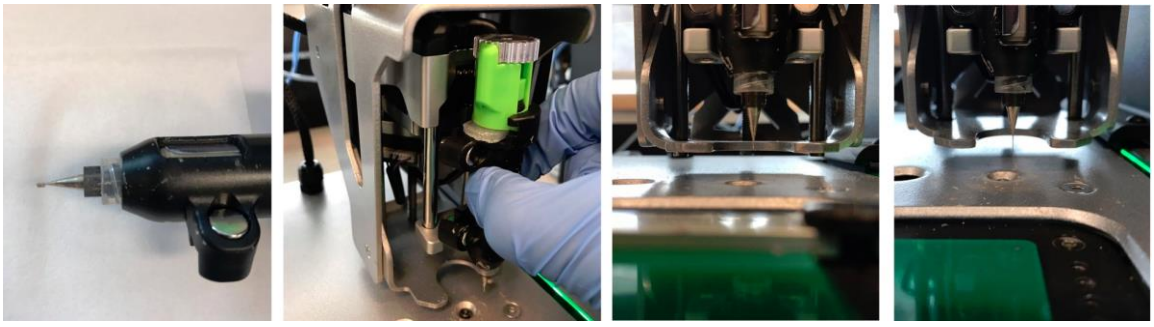

Figure 3.6. Ink level calibration procedure before printing

3.2.2. Top Layer Circuit Printing

Now V-one is ready to 3D print the PCB. Silver conductive ink is dispensed on the top layer of the substrate. First, the extrusion head is controlled by the motion platform which follows the sliced g-code in the software. This is a straight-forward procedure. After the top layer circuit is fully printed, the extrusion head and ink syringe are removed from the platform. At this moment, the printed ink is not conductive yet. Therefore the next step is baking the printed circuit trace on the embedded heat bed. The temperature and time are the important parameters and can be varied in the interface software depending on the substrate material property. The detail is explained next section. The baking process sinters Ag Nanoparticle and thus generates the conductive path.

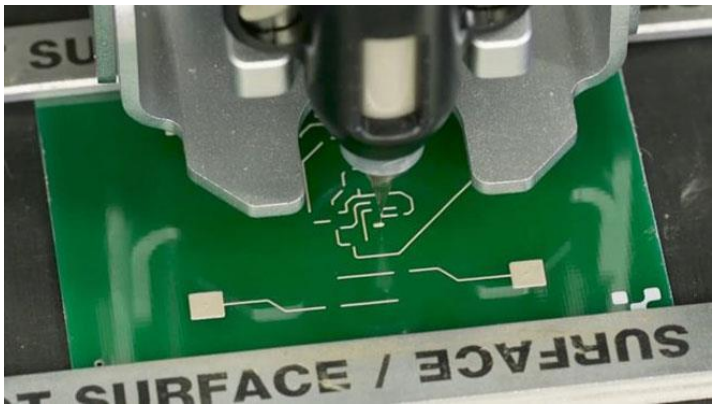

Figure 3.7. Top layer circuit printing procedure

3.2.3. Drilling

As previously mentioned, V-one leaves a donut geometry for any via and through-hole design (Figure 3.8). In order to make sure the bottom side circuit can be printed in the correct alignment with a top side, the drilling is necessary before printing bottom side circuit. In general PCB design, via the through-hole diameters are from 8mil to 12mil, only 6mil or even smaller in some extreme designs. A high-speed press driller (Dermer)(Figure 3.9a) and standard PCB driller bit kit (Figure 3.9b) are used in the drilling process. The donut ring is easy for manually drilling without requiring the CNC drilling. In the time-efficient point of view, this is a great advantage (Figure 3.9c).

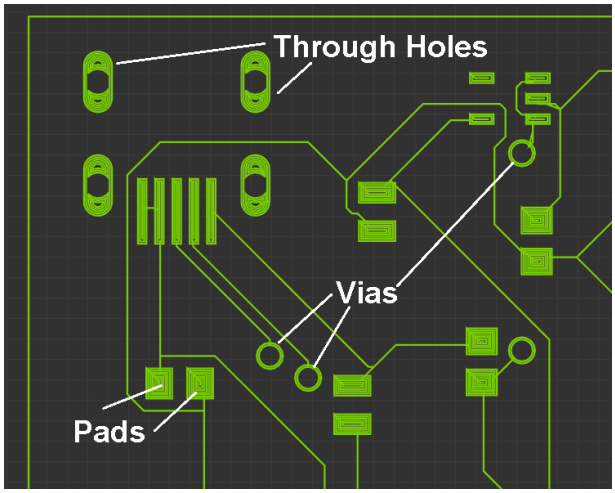

Figure 3.8. Circuit patterns of through-hole, vias, and pads for printing

Figure 3.9. (left) Dermer Mode 3000 press driller (middle) PCB drill bits set (right) image of drilling process for through-hole and vias

3.2.4. Bottom Layer Circuit Printing

There is one more calibration that must be done before actually printing the bottom layer circuit. As commonly known, circuits on the top layer and bottom layer are interconnected by the vias. Thus, any mismatch of the position of the printed circuit will ruin the whole 3D-PCB. It is crucial to make sure that every single via on bottom layer is aligned with drilled vias.

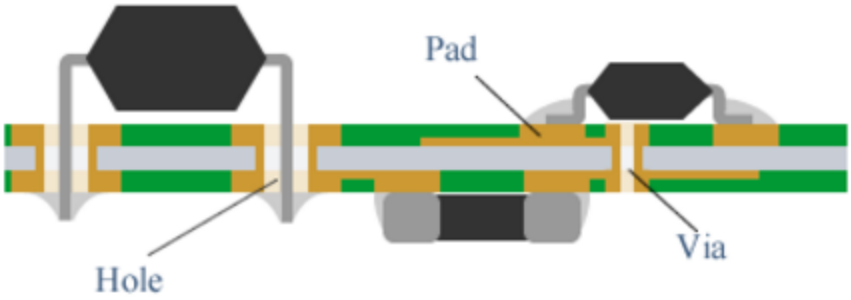

Figure 3.10. Illustration of cross section of PCB with vias and through-hole

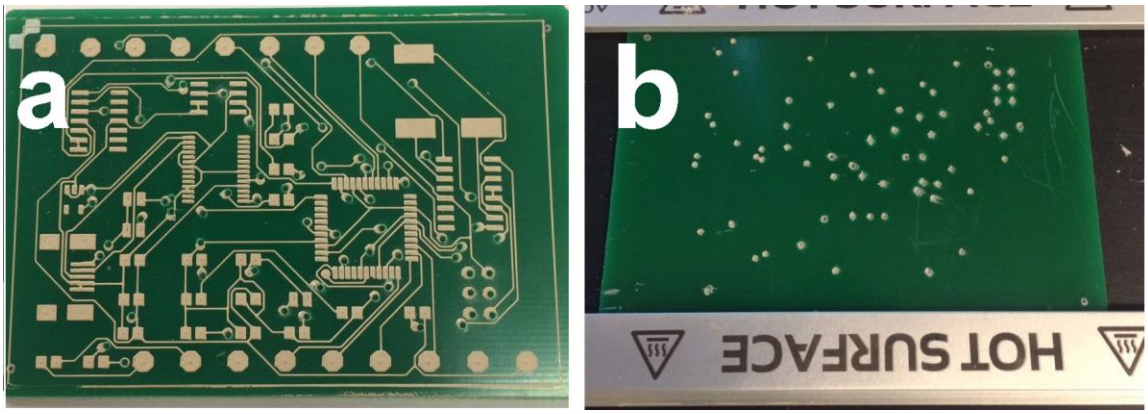

Figure 3.11. (a) Printed circuit pattern with vias on top layer after drilling (b) vias on bottom layer after drilling

To do so, the Gerber Bottom Layer file (GBL) is input in the interface software, and the detection probe is mounted on the XYZ platform. The XY coordination for the bottom layer can be calibrated by visually checking if the probe is located in the center of any two drilled vias (Figure 3.11). Now the new xy coordination is confirmed. Extrusion head with conductive ink syringe is remounted, same as printing the top layer, bottom layer circuit is dispensed following the same procedure and baked under the same condition (Figure 3.11).

3.2.5. Filling

Until this moment, both top layer circuit and bottom layer circuit are printed and fully sintered. Vias and through-hole are proper drilled. In order to connect the circuit on two layers. Vias must be filled with conductive ink. This done by manually operating the dispensing plunger. After all the vias are filled, the 3D-PCB is placed on the heat bed once again for the final baking (Figure. 3.12)

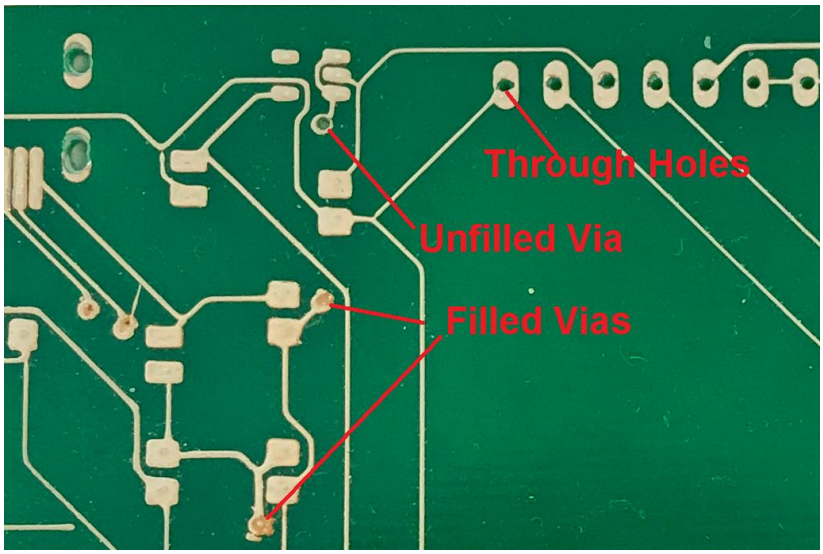

Figure 3.12. Image of filled vias, unfilled vias, and open through-holes on 3D-PCB

3.2.6. Solder Paste Printing

The 3D-PCB is fully printed, and individual circuit trace and via are checked in good connecting condition. Next step is placing electronics components on the 3D-PCB. For the surface mounted devices (SMDs), solder paste can be dispensed on the top of circuit pads using V-one. The only difference is the material in the syringe is no longer conductive ink, instead of the conventional solder paste. Gerber Top/Bottom Paste file (GTP/GBP) is input in interface software. The extrusion head dispenses the proper amount of solder paste (Figure 3.13). Placing the SMD components gently on top of the printed pad. The 3D-PCB is ready for reflow process.

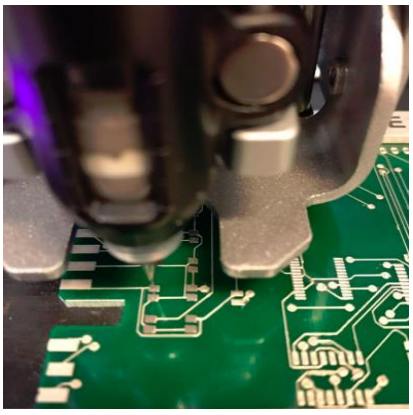

Figure 3.13. Image of dispensed solder paste on printed circuit pads

3.2.7. Reflow

Reflow soldering is a process in which a solder paste is used to temporarily attach one or several electrical components to their contact pads, after which the entire assembly is subjected to controlled heat, which melts the solder, permanently connecting the joint. Leaving the 3D-PCB with pre-assembled SMD on the heat bed. Reflow temperature profile can be varied according to different scenarios. Average reflow time is 25 minutes. The ideal temperature profile is usually based on three factors: peak temperature; maximum rate of change of temperature; time above liquidus. For a solder with a melting point of 179–183°C, the maximum allowable peak temperature is usually 220–230°C, and the minimum peak 195–205°C (Figure 3.14). If the board gets too hot, the board edges may turn brown and damage may be caused to SMT components.

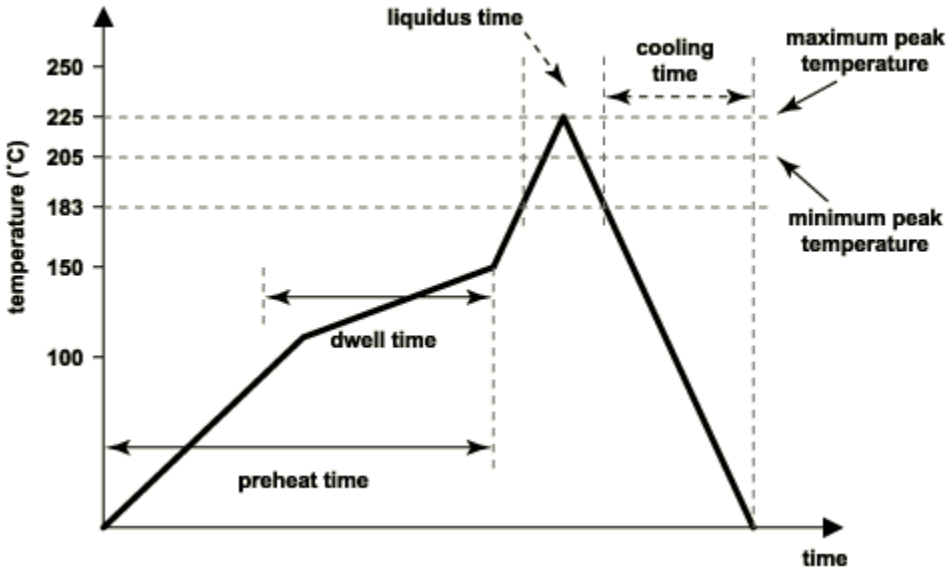

Figure 3.14. Reflow profile used for 3D-PCB

3.3. Parameter Control for PCB Printing

One of the most important step in this project is tuning the printing parameters. The nozzle diameter is 200 um. When AgNP ink is extruded from the nozzle, the printing parameter could affect the quality of printed ink significantly. There are three major parameters: slicing pass spacing, extrusion rate, nozzle tip height. A PCB circuit can be treated as a 2D layer, thereby the slicing procedure consists of the generation of several 1D lines covers the desired object area. Change this parameter will not affect the slicing of single trace, however large value of slicing pass spacing will generate relative fewer lines in the pad area. If the value is too large, the printed ink cannot cover the gap between each slice (Figure 3.15). On the contrary, if the value is too small, newly printed ink may overlap on previously printed ink. Thus the ink material may waste. 0.15mm was eventually selected as the optimal line space value

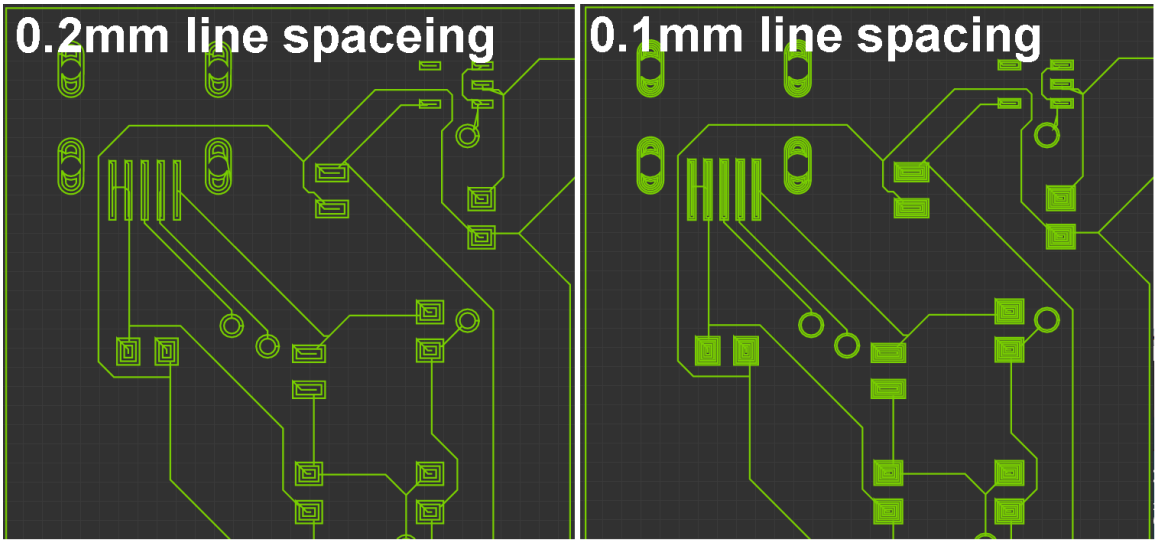

Figure 3.15. Sliced PCB G-code using different line spacing value

Extrusion amount and nozzle tip z position are two interference parameters. In order to printed perfect circuit track, the 3D printer must dispense complete ink patterns (Figure 3.16a). If the nozzle tip is too far away from the substrate or extrusion amount is too small, dispensed ink may not stick on the surface following exact design (Figure 3.16b). If the nozzle tip is too low or extrusion amount is too large, the dispensed ink may be squeezed between the nozzle and substrate, which two individual traces may accidentally connect (Figure 3.16c). This brought a challenge to PCB layout design for high-density circuit.

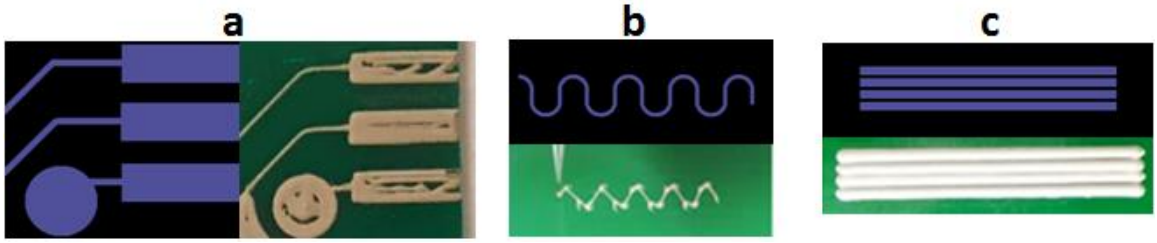

Figure 3.16. Printing quality comparison (a) large uncoverd area when line space is too high (b) bad dispense when nozzle position is too high or ink extrusion amount is too small (c) over pressed ink when nozzle position is too low or ink extrusion amount is too large

Figure 3.17. Extruded ink pattern with optimized printing parameters

The optimzied printing parameters are proposed as slicing line space (0.15 mm), extrusion rate 500 mm/min, and nozzle tip height (0.15mm). The printed ink pattern can be garenteed using these parameters (Figure 3.17).

As described in the last section. Printed AgNPs ink circuit requires baking to form electrical conductivity. The Baking temperature is one of the most important parameters which must be optimized. If the temperature is too low, the silver nanoparticle may not melt completely and cause low conductivity of overall circuit. It can bring a significant negative effect on the high current density application and small signal measurement applications, such as electrochemical sensing. On the contrary, baking under temperature way too high is also unnecessary, too much thermal energy may cause unwanted deformation or even damage of the PCB substrate. A rigid substrate such as FR4 epoxy board has high thermal property. However, when flexible materials usually do not have such good thermal property. The common flexible substrate such as PET has a melting temperature at 240 ℃ and glass transit temperature at 110℃. Baking temperature higher than 110℃ can ruin the substrate if PET is used. Thus, electrical conductivity and deformation degree during baking process are investigated.

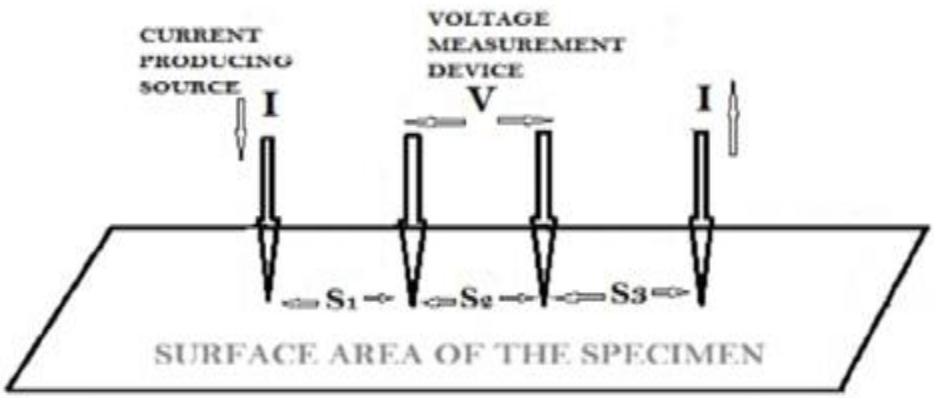

Figure 3.18. Electrical resistivity measurement by four point probe method [108]. Reprinted with permission.

A four point probe method is the most common used method for measuring the electrical conductivity/resistivity of thin depth (Figure 3.18). The four point probe contains four thin collinearly placed tungsten wires probes which are made to contact the sample under test. Current I is made to flow between the outer probes, and voltage V is measured between the two inner probes, ideally without drawing any current. If the sample is of semi-infinite volume and if the inter-probe spacings are s1= s2 = s3 = s, then it can be shown that the resistivity of the semi-infinite volume is given by

$$R = k\,(\frac{V}{I}) \tag{3.1}$$

Where k is the a geometric factor. In the case of a thin sheet, k = 4.53 [108]. However, this method requires four probe stations, which was not available in the lab. Therefore, a alternative method was implemented. Two probe method is the simplest method of measuring resistivity and is illustrated in Figure 3.19. In this method, voltage drop V across the sample and current through the sample I are measured. Then the resistivity is given as

$$R = \frac{VA}{IL} \tag{3.2}$$

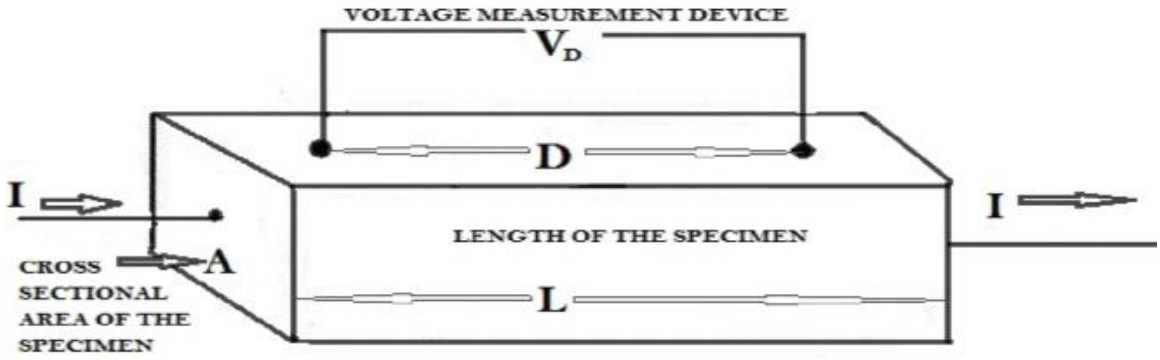

Figure 3.19. Electrical resistivity measurement by two probe method [108]. Reprinted with permission.

where A is the cross sectional area of the specimen. In order to minimize the error, seven identical samples (10mm× 3mm) were printed by V-one on PET substrate with a thickness of 50 μm. Each sample is baked under 30℃, 50℃, 70℃, 100℃, 130℃, 160℃, and 190℃ for 1 hour (Figure 3.20a). Their resistivity was calculated according to the two probe method. Each printed specimen was measured by the probe station inside of a vacuum chamber (Figure 3.20b). According to data from figure 3.18, the optimized temperature with 70℃ is lower than a glass transit temperature of PET (110℃). Thus, annealing process does not cause unexpected curvature of the sensor substrate.

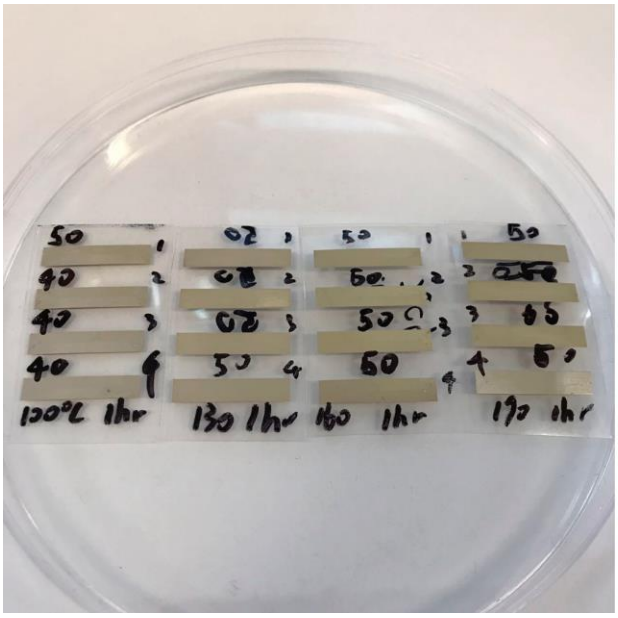

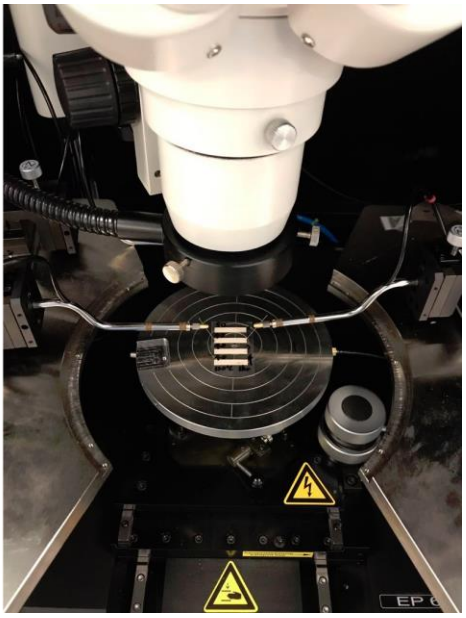

Figure 3.20. (left) Printed ink specimen on PET substrate with different baking temperatures (right) resistivity measurement setup using the probe station

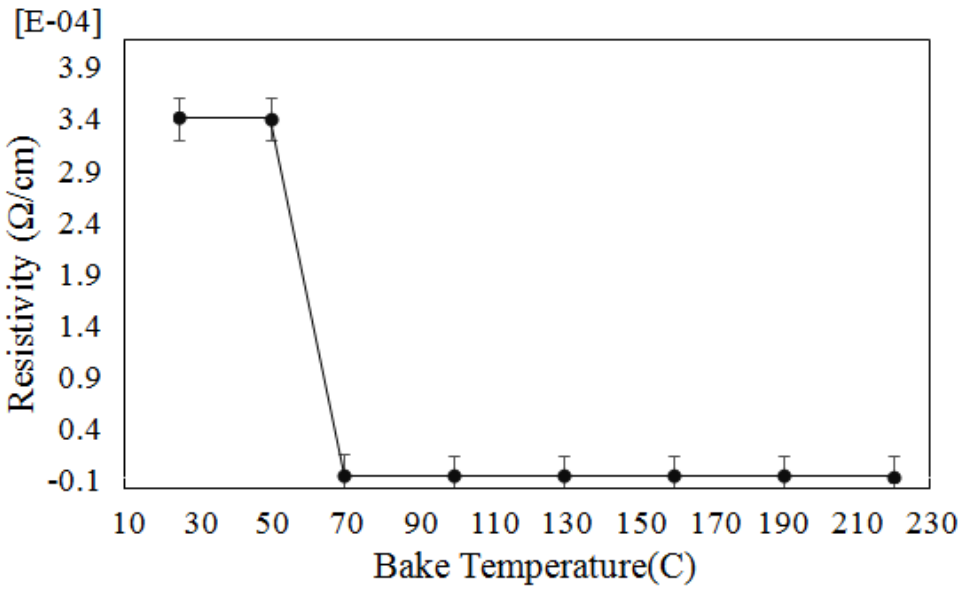

Figure 3.21. Electrical resistivity of printed silver ink under different baking temperature

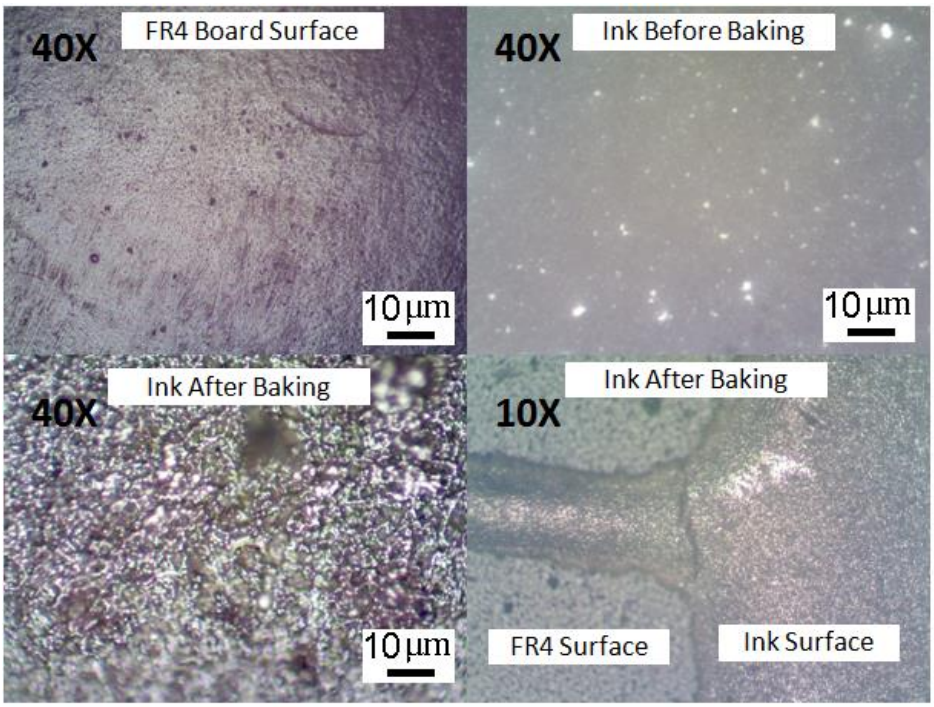

Figure 3.22. Micro images of printed AgNP ink before baking and after baking using optimized baking temperature

3.4. 3D Printed Flexible Electro-chemical Sensor

Several designs of sensor electrode were tested in term of mechanical durability and space efficiency. The very first sensor was printed on FR4 substrate without considering the physical connection between itself and potentiostat. As a result, printed electrode pattern with conductive ink was fine, but soldering process a thin wire on the electrode destroyed the printed electrode because of the high temperature of soldering gun (Appendix A). Later, optimized electrode design adapted a feature of card edge connector (Figure 3.19). In this way, the sensor can be inserted into a three-pin card edge connector without the risk of damage. The final design of the proposed flexible lactate sensor patch is shown in Figure 3.20 which contains two three-electrode electrochemical sensors that include two individual working electrodes (WE, 2mm dia.), a sharing reference electrode (RE, 4mm × 0.5mm), and a sharing counter electrode (CE, 4mm × 3mm). The electrodes are fabricated with AgNP ink on flexible PET substrate via a 3D-printing process using AgNPs by using a 3D-printer from Voltera. In order to enhance the printed electrodes' conductivity, a thermal annealing process is optimized as described in section 3.3. The baking temperature was 70℃.

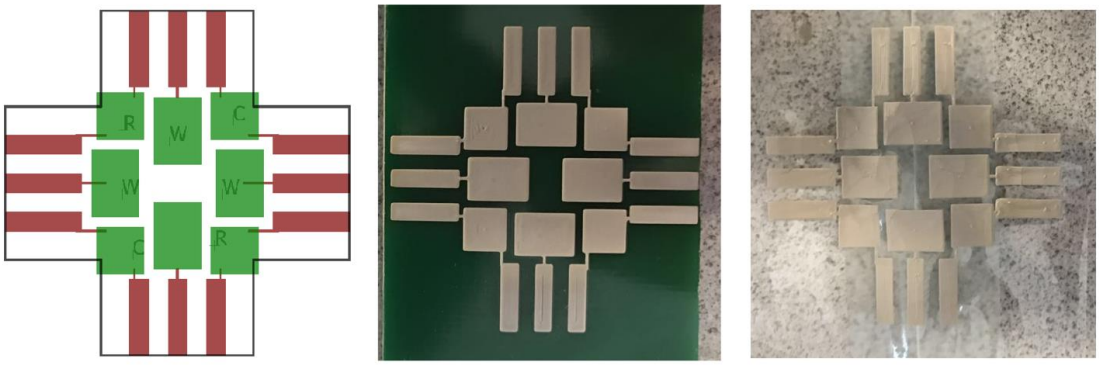

Figure 3.23. First sensor design with card edge connection feature (left) CAD deisgn (middle) printed electrodes on rigid FR4 board (right) printed electrodes on PET substrate

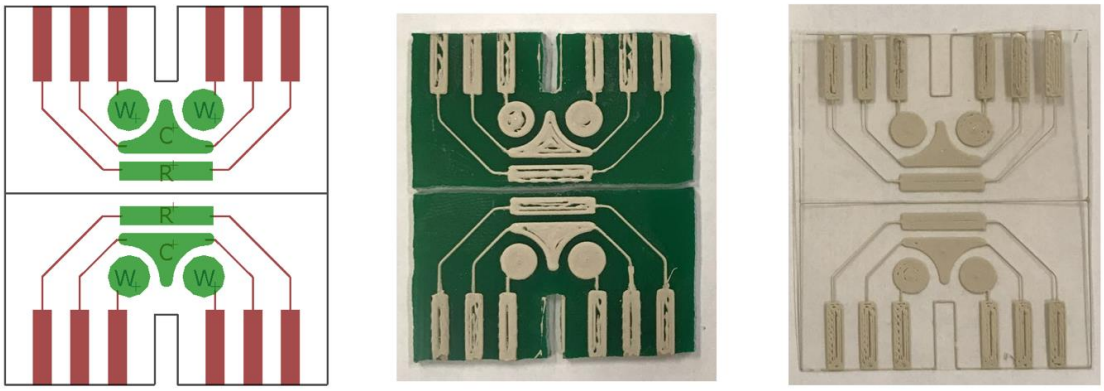

Figure 3.24. Final sensor design with card edge connection feature (left) CAD design (middle) printed electrodes on rigid FR4 board (right) printed electrodes on PET substrate

3.4.1. Formation of Working Electrode

Nafion has received substantial attention as electrolyte polymer in Chlor-alkali electrolyzers replacing sodium amalgam or diaphragm cells and in proton exchange membrane (PEM) fuel cells due to unique ionic selectivity, chemical resistance, excellent thermal and mechanical stability. Perfluorosulfonic membrane Nafion was first developed by Dupont de Nemours in 1962. Sulfonated fluoropolymer has a hydrophobic backbone of polytetrafluoroethylene (PTFE) with side chains containing hydrophilic sulfonate ionic group[109-110]. The chemical formula is:

$$-\left[\begin{array}{c}CF-CF_2-\left(CF_2-CF_2\right)_n\\ |\end{array}\right]_m-$$
$$O-\underset{\underset{CF_3}{|}}{CF}-CF_2-O-CF_2-CF_2-SO_3^-\,H^+$$

Nafion is an artificial polymer well-known for its excellent biocompatibility and perm-selectivity. According to work done by M.A. Abrar [22]. The negatively charged Nafion shows its ability to eliminate anionic interferences such as ascorbic acid and nitrite. However, a significant decrease in sensitivity has been observed both for sensors incorporating Nafion as mixed with enzyme matrix and used as a separate layer on the sensor surface. Thus an optimum concentration of the selective membrane needs to come of age. Diluted Nafion solution with a concentration of 5% has been showed recently to permit maximum hydrogen peroxide to pervade through while still effectively acting as an impermeable membrane to block ascorbate.

Nafion was received as a 20 wt. % mixture of lower aliphatic alcohols and water. It was dissolved in ethanol to prepare diluted (5% v/v) Nafion solution. To prepare the Nafion selective membrane, 20 µL of the solution was drop cast on the electrode surface and left it to dry for an hour.

Glutaraldehyde (GA) - as a cross-linking agent; was used to immobilize Lactate Oxidase (LOD) in conjunction with Bovine Serum Albumin (BSA) as stabilizing reagent. 50 U of LOD was dissolved in 500 µL of Phosphate Buffer Saline (PBS) and was equally separated into 25 aliquots; each containing 2 U of LOD. All aliquots were stored at -200C A total mass of 6 mg of BSA was dissolved in 40 µL of PBS and stored at 40C. Prepared BSA solution was mixed with 20 µL of LOD solution and stored at 40C. Glutaraldehyde (GA) was diluted into 10% solution with DI water, and a 30 µL of diluted GA solution was concocted with LOD/BSA mixture and 20 µL of LOD/BSA/GA of the solution was drop cast on Nafion coated electrode surface. After waiting for 2 hours, the prepared sensor was gently rinsed with PBS to get rid of excess GA.

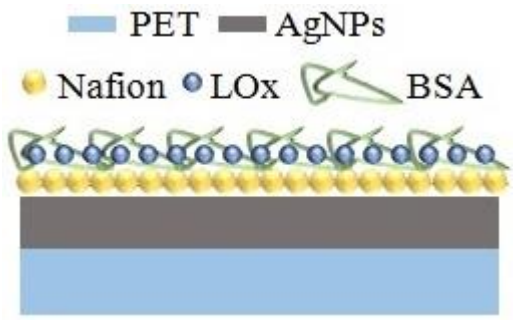

Figure 3.25. Cross sectional structure of the working electrode with enzyme layer

3.4.2. Generation of Reference Electrode

One of the most common reference electrode used for electrochemical measurements is silver/silver chloride (Ag/AgCl) electrode. These are quite stable, robust, usable under a wide variety of conditions and cheap to fabricate. A most common technique to chloridized silver is to electroplate it in a chloride containing the solution. Electroplating of a silver wire could be achieved by placing it in a cell containing 0.1~1 M HCl or KCl and applying about 0.5 mA/cm2 for 30 minutes. If chloridized in the absence of light, the color should turn in to reddish dark brown or pale tan otherwise. Periodic reversal of the polarity of the electrode while plating tends to yield a more stable reference

electrode. After washing with water, the color of the coating ranges from pink to shade of plum.

An easy and inexpensive alternative method could be employed to soak silver in hypochlorite solution that obviates the need for an electrochemical cell. Commercial household bleach can be used in this regard. Ag/AgCl reference electrodes for the lactate sensor were prepared by dunking 3D printed electrodes in 8.25% Clorox bleach for 30 second and then they were washed with DI water. The final fabricated lactate sensor can be inserted into a 3-pin card edge connector (Figure 3.22).

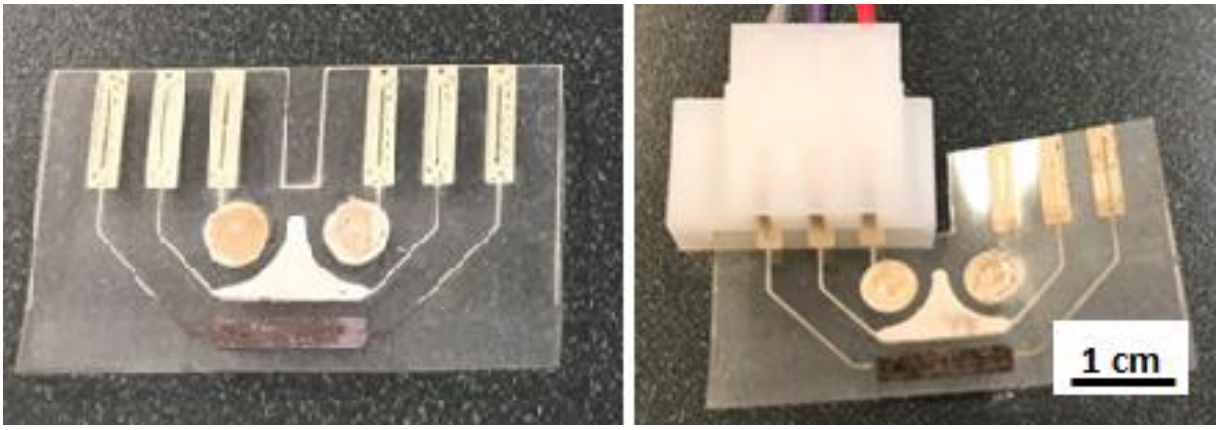

Figure 3.26. (left) proposed printed lactate biosensor prototype with WE covered by the enzyme and chloridized RE (right) lactate biosensor connected with a 3-pin card edge connector

3.5. Design of 3D Printed Potentiostat

Numerous commercial instruments are available; unfortunately, commercial potentiostats are expensive and operate with limited design information available to users about their circuitry and behavior. Thus, most potentiostats impose significant constraints on researchers who are developing new measurement techniques and application.

Benchtop potentiostat systems can perform numerous electrochemical analysis techniques within a wide range of parameters including variations of signal output and data interpretation. However, our initial potentiostat system design focus on performing cyclic voltammetry and amperometry. As such, many costs were omitted by minimizing

system requirements and controls; these design parameters also allowed for minimization of the device size.

To perform cyclic voltammetry, a voltage is applied to the working electrode, momentarily held at an initial voltage, and linearly decreased until a vertex voltage is reached. The voltage is then reversed and swept back towards the initial value. Throughout this cycle, electron transfer occurs within the electrochemical cell; this current is measured at the working electrode and recorded for analysis. This section discusses how the potentiostat was designed to accomplish these tasks.

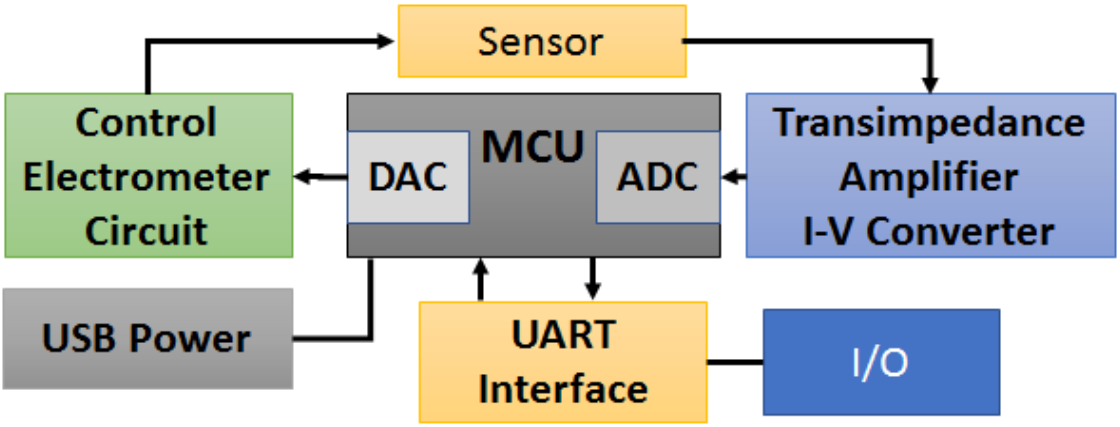

Figure 3.27. Block diagram of the potentiostat

3.5.1. Design and Fabrication of Potentiostat Circuits

The potentiostat circuit had endured several redesigns before a final design was established. However, in every design, the potentiostat circuit must embed the necessary components to execute electrochemical functionalities. The major tasks are voltammetric for the potential sweep and current conversion for small signal acquisition. Meanwhile, to assure the durability and reliability of physical implementation of 3D printing, its PCB design has to be as lean as possible.

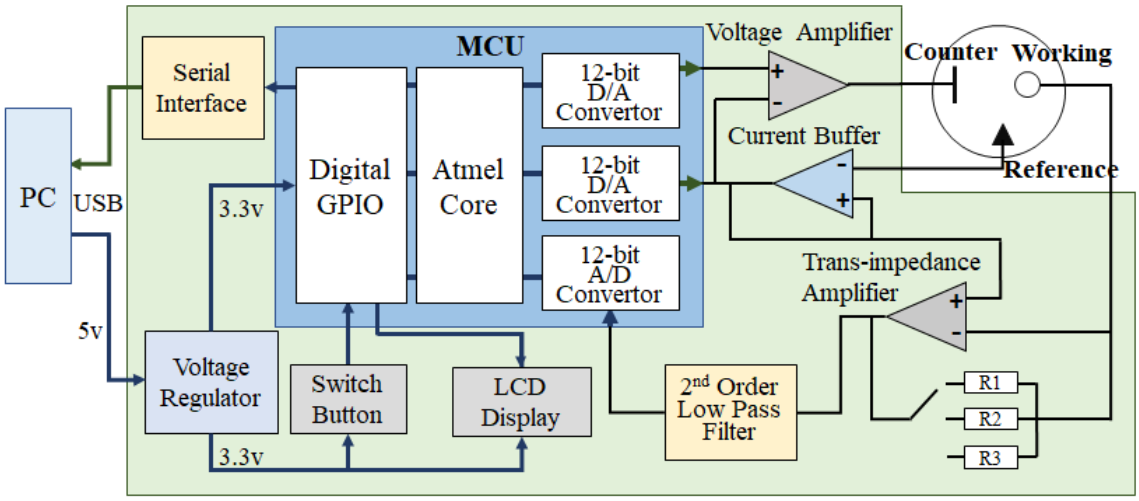

Figure 3.28. Detail schematic diagram of the proposed potentiostat system design

A single channel potentiostat based on a similar circuit architecture to the CheapStat [109] is designed. The schematic diagram of the fabricated potentiostat circuit and is shown in Figure 3.24. In order to study the electrochemical behavior of analytes, careful control of the interfacial potential between WE and RE from an electrochemical cell is essential to allow electrochemical current to be measured at a stable level during a short period. In order to apply potential, RE with constant potential is required. A low-power microcontroller (ATXMEGA32, Atmel) serves as the core for generation of voltammetric excitations. In order to realize the electrochemical test function such as cyclic voltammetry, the potentiostat has to generate a sweep potential in desired range and scan rate in both forward and reverse directions. Thus, a comparison circuit with a bidirectional switch in Figure 3.25 is connected to a digital-to-analog converter (DAC). It generates the potential in a range from -1.65V to 1.65V across the WE and RE with a resolution of 0.8 mV. In the meantime, an operational amplifier (TLC2264ID, Texas Instrument) serves as a current buffer due to its infinity high input impedance to limit any current that might flow through RE. Therefore, the current is forced to flow between WE and CE. Thereby, RE remains in proper polarity to keep the WE potential at a constant value with respect to the RE.

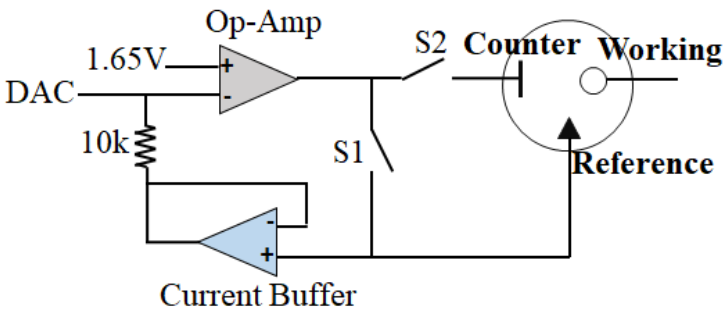

Figure 3.29. Electrometer generator circuit

The lactate sensor output current is usually in the range of 10^{-6} µA. The common approach of current measurement in voltammetric cells is the use of a trans-impedance amplifier instead of an operational amplifier. A feedback resistor (R_f) is placed between the inverting input and the output, while the non-inverting input is grounded. Fabricated potentiostat design includes a transimpendace amplifier (OPA380, Texas Instrument), because of its ultra-low input impedance and a high output impedance as shown in Figure 3.26. The converted voltage at the output is

$$V_{output} = V_{ref} + IR_f \tag{3.3}$$

where R_f is the gain in the feedback path. Thus, measurement ranges of electrochemical currents are adjusted via onboard jumper as ±10 µA, ±50 µA, and ±100 µA with resolution of 4.88 nA, 24 nA, and 48.8 nA respectively.

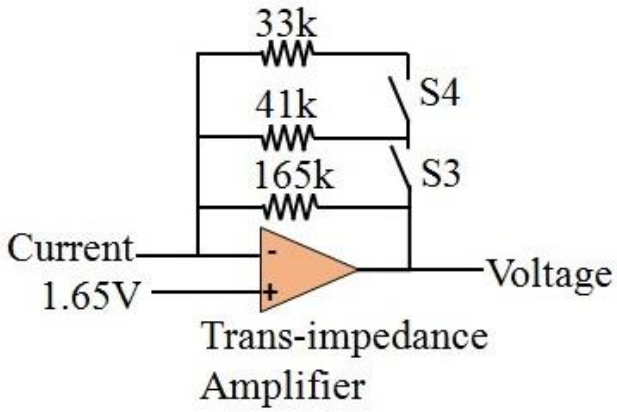

Figure 3.30. OPA380 trans-impedance amplifier i-v converter

A 2nd order Sallen-Key low pass filter is implemented to wipe out any noise signal larger than 60 Hz, because of its high selectivity as shown in Figure 3.27. Also, the

microcontroller circuit is powered by a USB cable connected to a computer. It is entirely feasible to directly display the results on the LCD screen by implementing simple data analysis algorithms in the firmware of the microcontroller. The principal circuit (Figure 3.28) and its PCB were designed using Eagle PCB software by EagleCAD

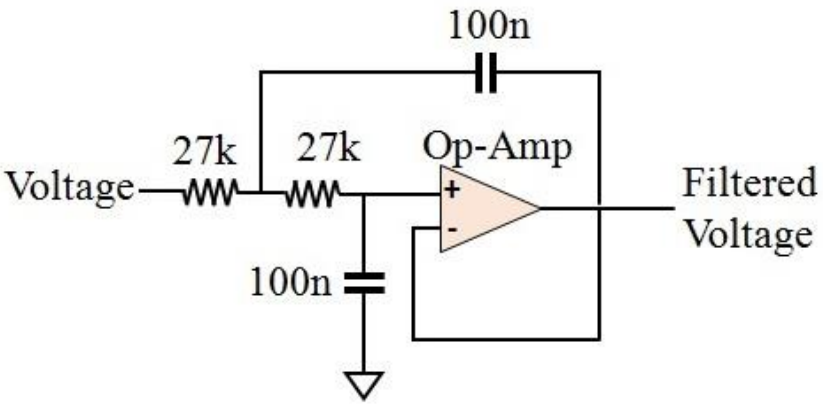

Figure 3.31. 2nd order Sallen-Key low pass filter circuit

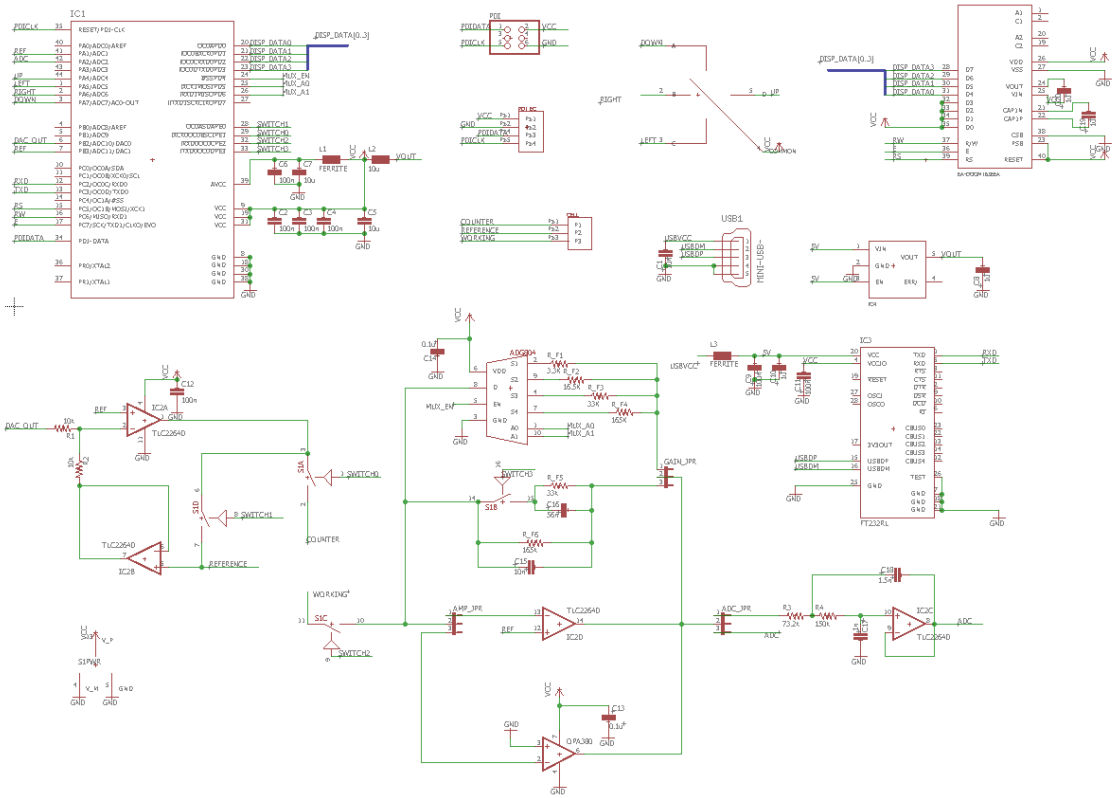

Figure 3.32. Schematic of potentiostat circuit design using Eagle PCB. Zoom in detail is in appendix C

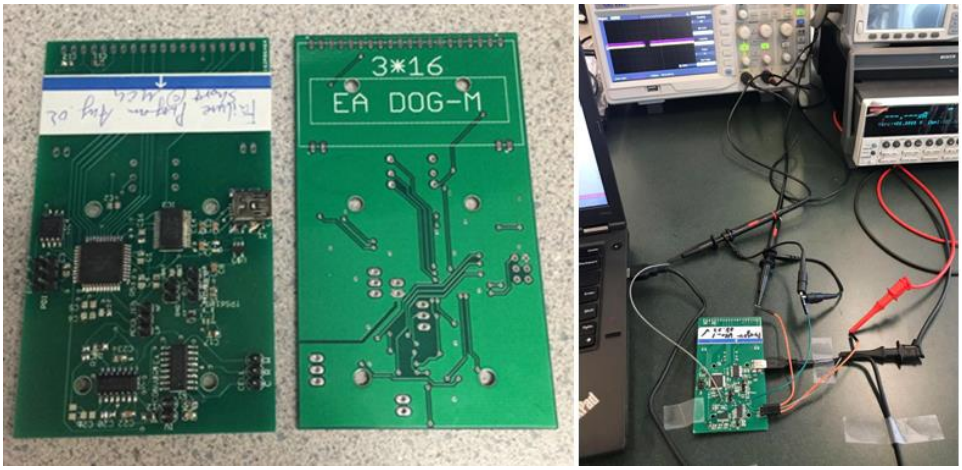

Figure 3.33. (left)Test potentiostat PCB fabricated by the conventional method (right) Test setup for the conventional potentiostat

3.5.2. Development of Potentiostat Firmware

Two software programs were written to control the portable potentiostat: the software used to program the microcontroller and the digital circuit, and the software used to capture the output data and plot the results in real time. Appreciated to the open source firm from 'CheapStat.' The microcontroller firmware was updated on the original architecture in the AVR Studio 4 using C language. The c. project file must be converted to hex file using WinAVR in order to burn the firmware into the MCU (Appendix C). The full program is provided in Appendix D contains all code and comments in further detail. An overall program is a state machine, which can switch the functions(CV or amperometry) depending on user's input parameter. To execute electrochemical functionalities, it is established with a counter and a while loop. Once the user has input an initial and peak voltage, and the start button has been pushed, the counter begins counting until the initial voltage (corresponding to a number between 0 and 255) is reached. At this moment, the output of the counter is enabled. The counter continues to count down until the peak voltage is reached and then begins to count upwards. Once the initial voltage is once again achieved, the loop terminates. The second task is accomplished by a series of analog reads and an averaging algorithm. The output of the ADC is read eight times per step of the voltage sweep; the weighted average is computed for both the applied voltage as well as the resulting current. The communication software, described in the following section, retrieves these values and creates a plot in real time.

The graphical user interface (GUI) was programmed in JavaScript which is used to upload data retrieved by a microcontroller to an Excel spreadsheet in real time. The GUI was implemented to allow the user to see what values are being selected by the potentiometers, as well as to initiate and terminate the connection with the device. The voltage applied to the electrochemical cell, as well as the current generated at the working electrode, were updated to an Excel spreadsheet and plotted in real time. The user may also clear the data from the spreadsheet at any time.

3.6. 3D Printed Potentiostat on Epoxy Board

3.6.1. Design Optimization of Potentiostat PCB

The design process needs to follow previous circuit requirements to guarantee electrochemical functionality. Although the use of conventional PCB CAD design software for layout and routing of 3D-printed electronic devices is possible when the flat-board design is involved, the software still lacks the support on 3D-printing feature and design routine checking. Therefore, multiple 3D-printing routings and pad optimizations are manually done. Firstly, a 3D-PCB shall perform excellent electrical conductivity in the printed circuit trace pattern to avoid disturbance of electrical signals from resistance loss. Secondly, the resolution of printed traces and clearances need to meet the requirements for modern electronic packages. Thirdly, minimizing the physical connection on board with possible force applied (e.g. jumper pins, cable socket) is critical because unlike soldering ICs on foiled copper, it is much weaker when soldering ICs on the silver pad. Falling off any ICs from PCB may cause system failure.

In PCB design, the term of design rule is a categorization of parameters based on capabilities of the equipment and the overall process. Design rule checking (DRC) makes sure the physical PCB layout of a particular chip layout satisfies design rules parameters including minimum trace width, minimum trace spacing, drilling/via diameter. The general design rule limitations of conventional PCB technology are trace width of 6 mil (0.15 mm), trace space of 6 mil, and minimum finished drill of 12 mil (0.3 mm). As mentioned in section 3.1. The printhead nozzle diameter is 200 um (8mil). The pattern resolution of the printing system is 150 μm (6mil) [110]. The minimum pin-to-to pitch which printing system can achieve is 500um. Both parameters can satisfy conventional PCB design rules and modern IC packaging.

3.6.2. Prototyping of 3D Printed Potentiostat

Several versions 3D-PCB layout were designed. In the early attempts, SMD components and DIP components were separated on two 3D-PCBs with connection by jumper cable (Figure 3.32). The purpose was to reduce the density of ICs and traces on the board, thereby reduced the possibility of error and increased the printing quality by V-ONE. Moreover, the LCD screen is sensitive to high temperature, which cannot be soldered using reflow process.

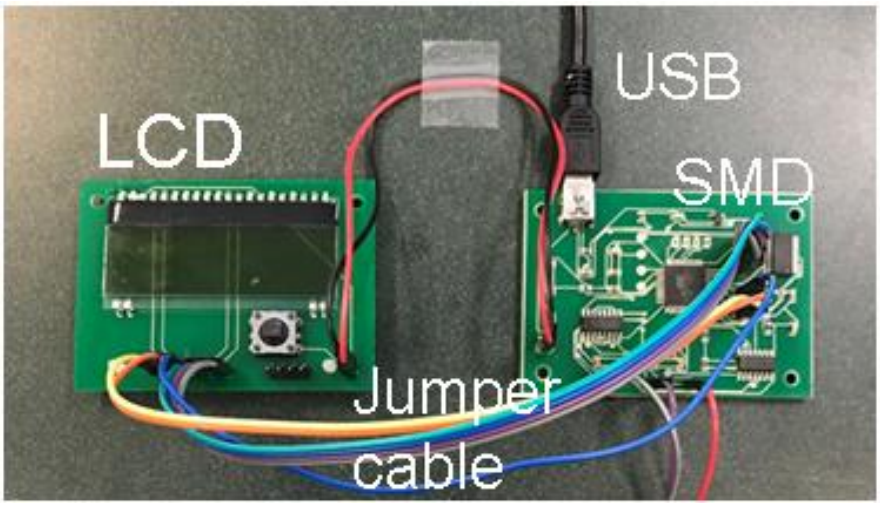

Figure 3.34. Early potentiostat prototype on separated 3D-PCBs

After the printing process and optimal printing parameter were secured, more integrated 3D-PCB was designed (Figure 3.33), both SMD component and DIP component were on the same board. Two card edge connection pad (3-pin and 4-pin) were designed to replace dip connection for programmer and sensor. Figure 3.33 showed the latest PCB layout in EagleCAD and proposed connection feature between 3D-PCB potentiostat and sensor. The final 3D-PCB was printed using parameters of 0.15 mm line spacing, 150 um nozzle height, and 50 extrusion amount. After verifying the conductivity of each traces. Solder paste was dispensed on the component pads, and all the SMD components were placed onto along with a DIP socket. In the way, entire 3D-PCB can be implemented in the reflow process without damaging any components. Finally, an LCD screen was plugged into the dip sockets (Figure 3.34). The whole fabrication process is no more than 8 hours.

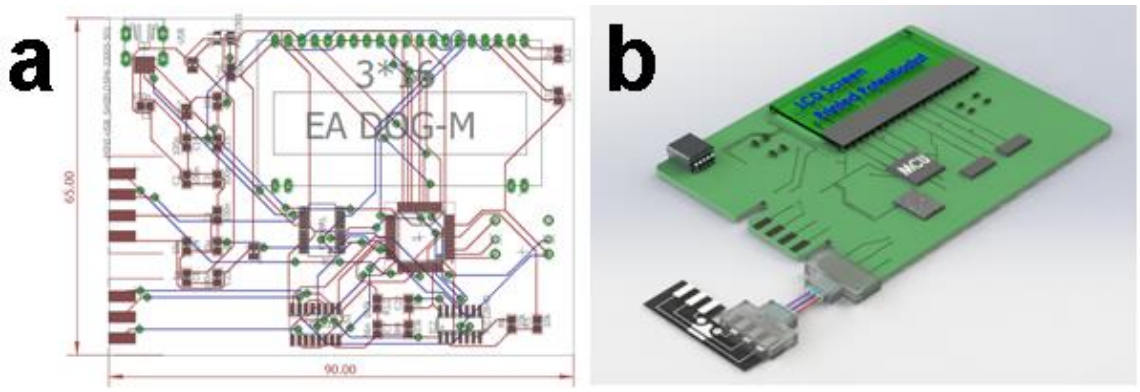

Figure 3.35. (a) latest PCB layout in EagleCAD (b) proposed connection feature between 3D-PCB potentiostat and sensor

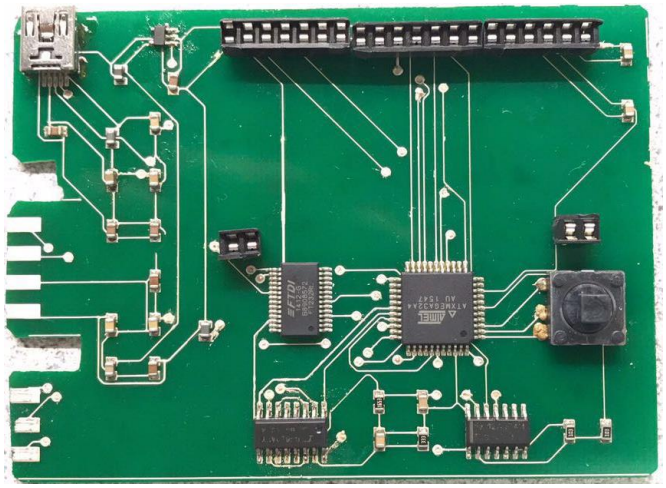

Figure 3.36. The final 3D-PCB p4otentiostat with SMD components and DIP sockets

Chapter 4.

Characterization of 3D Printed Electrochemical System

4.1. Characterization of 3D printed Lactate Sensor

Proposed 3D-printed lactate sensor's electrochemical behavior is verified with Cyclic Voltammetry (CV) test performed on a commercial electrochemical analyzer (CHI 1205B, CH Instruments Inc.) before using the 3D-printed potentiostat. Cyclic voltammetry is a typical voltammetric technique where the linear potential ramp is applied between electrodes. Redox current pattern typically shows a duck shape. Lactate solutions are prepared in PBS (pH = 7.0) with 5 mM, 10 mM, and 15 mM concentration. 20 μL-lactate solutions were dropped evenly via micropipette onto the sensor test area with a scan rate of 100 mV/s to the WE versus the RE. The generated currents in the measurement range from -2 V to 2 V is analyzed. The current-potential data on a computer is obtained. Figure 4.1(a) shows a group of typical cyclic voltammograms at different lactate concentrations. The graphs of the cyclic voltammograms reveal a typical reversible redox reaction. Receptively, cathodic peak current ((I_{pc}) and anodic peak current (I_{pa}) are located at 0.25 V and -0.5 V. Therefore, the operating potential of the lactate sensor is selected according to the CV results. The operational potential is 0.25 V for all the subsequent since the oxidation peak is found at 0.25V.

The amperometric response of the biosensor upon addition of lactate with different concentrations is presented. Current response rises linearly as the concentration increases from 0 to 15 mM (Figure 4.2a). Sensor response reaches to 90 % of the constant value within 60 seconds. Moreover, sensor's durability and stability are also important properties. The amperometric response is investigated on the same lactate sensor after 24 hours. The respond current keep in same order of a few tens of μA (Dash curves in Figure 4.2b). Therefore, the proposed lactate sensor can readily implement with a 3D-printed potentiostat.

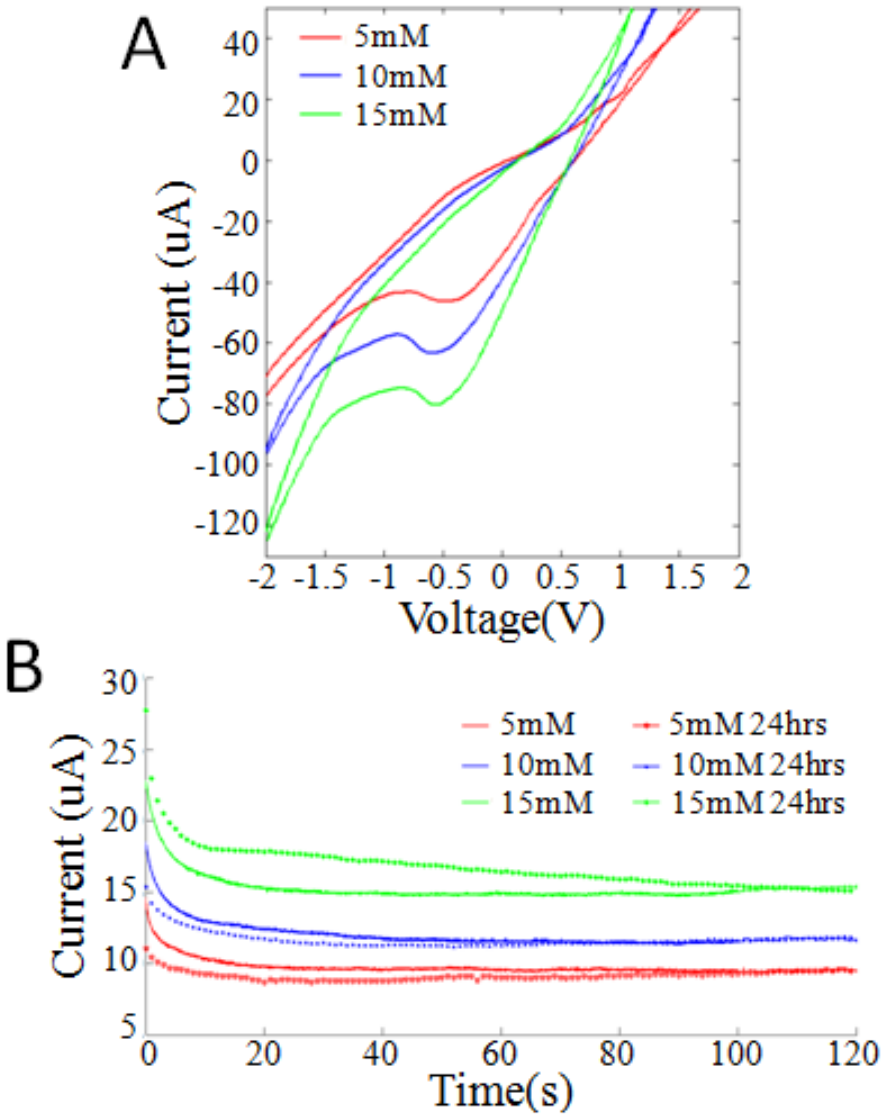

Figure 4.1. Lactate biosensor charetericaztion test results: (a) cyclic voltammetry curve using 5,10,and 15mM lactate solution. (b) Amperometric measurements in new condition and in 24 hours.

4.2. Cyclic Voltammetry for Redox Analysis

In order to verify the 3D-printed potentiostat system, a comparative test was investigated depending on different scan rates using the fabricated 3D-printed potentiostat (Figure 4.2). CV test was executed with 15 mM lactate which the potential value was sweeping from -1.6 V to 1.6 V with five scan rates (50 mV/s, 100 mV/s, 200 mV/s, 300 mV/s, and 400 mV/s). In cyclic voltametry, the Randle-Seycik equation indicates the effects of concentrations of electroactive species and scan rate on the peak current. When the concentration of lactate is constant, the redox peak current in a cyclic voltammetry is

proportional to the square roots of scan rate. Higher CV scan rates give rise to higher redox current. The analyzed result shows that the relationship between the scan rate and peak current fits the Randles-Sevcik equation.

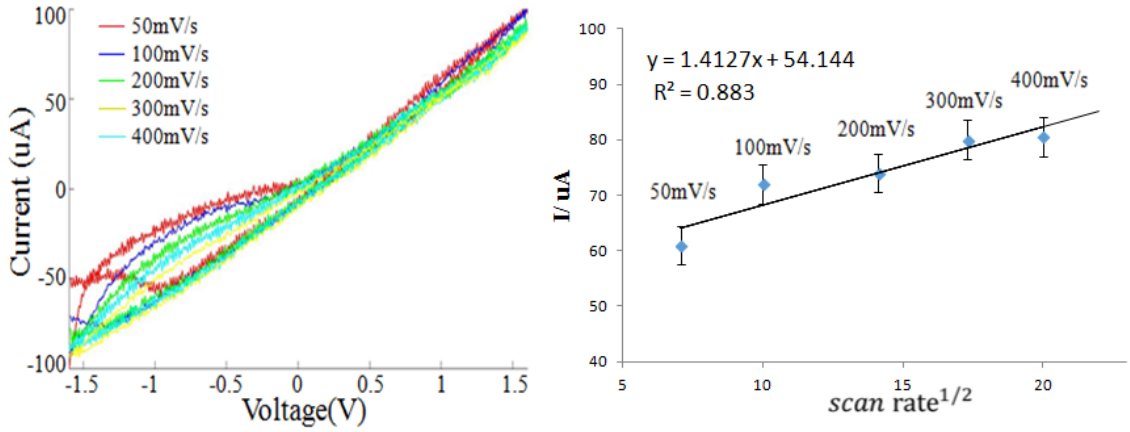

Figure 4.2. (left) cyclic voltammograms measurement of 15 mM Lactic Acid solution at different scan rates from 50mV/s to 400mV/s, (right) linear relation between absolute value of anodic current peak and square root of scan rate

According to the results, it appears that the total current increases with increasing scan rate. This can be explained by considering the size of the diffusion layer and the time taken to record the scan. The Cyclic voltammogram will take a shorter time to record as the scan rate is increased. Therefore the size of the diffusion layer above the electrode surface will be different depending upon the voltage scan rate used. In a slow voltage scan, the diffusion layer will grow much further from the electrode in comparison to a fast scan. Consequently, the reactant flux to the electrode surface is smaller at slow scan rates than it is at faster scan rates. As the current is proportional to the flux towards the electrode, the magnitude of the current will be lower at slow scan rates and higher at high rates. The quantitative detail of this behavior is described as Randles-Sevcik equation. In this equation, the peak current i_p can be predicted using equation (2.12). Moreover, it is clear that the peak occurs at the same voltage and this is a characteristic of electrode reactions which have rapid electron transfer kinetics.

Furthermore, in order to characterize the 3D-PCB potentiostat electronics performance. CV and amperometric tests were performed using the 3D-PCB potentiostat and the conventional PCB potentiostats which mentioned in section 3.31 under same conditions. The CV scan rate is 100 mV/s, and the potential sweep range is from -1.6 V to 16.V. The lactate solutions are measured in 5 mM, 10 mM, and 15 mM concentration.

Figure 4.3a shows the CV test curve from conventional PCB potentiostat. Moreover, Figure 4.3b shows the CV from 3D-PCB potentiostat. Both CV test curves show a typical duck shape with significant reduction peak at the potential of -0.5 V. Nevertheless; it is evident that CV curves that from 3D-printed potentiostat have larger noise oscillations than the potentiostat made by conventional PCB. Overall, the CV data with two potentiostats: conventional PCB and 3D-printed PCB show very similar regarding peak currents, peak potentials, and current densities characteristics expect the signal to noise.

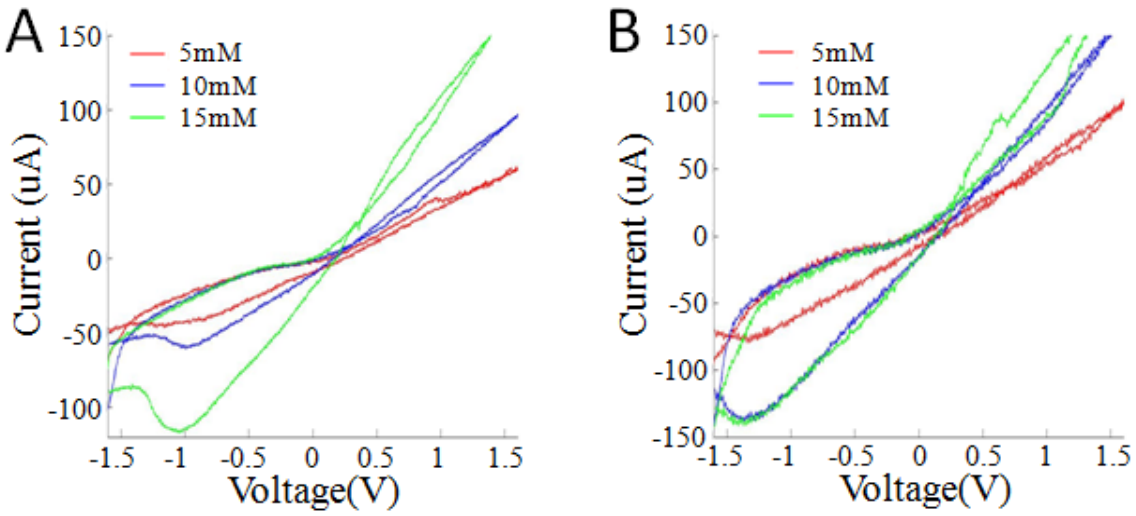

Figure 4.3. Cyclic voltammetry measurements of lactic acid at 100mV/s scan rate via (a) proposed potentiostat design using conventional PCB fabrication method (b) proposed potentiostat design using 3D printing method

4.3. Amperometric i-t curve and Calibration

Amperometric i-t curve measures the current at a fixed working electrode potential, and the resulting current from the electrode is monitored as a function of time. This current-time curve represents the change in the concentration gradient. As time goes, the reactant depletes at the working electrode surface, and the slope of the response decreases as well. A constant 0.25 V potential is applied between WE and RE in the amperometric response test based on previous CV results. All In vitro experiments were carried out by drop casting and bearing off 50 µL of the solution with different concentrations on the sensor each time. The amperometric response by using conventional PCB (Figure 4.5a) and 3D-PCB potentiostat (Figure 4.5b) are presented respectively. Current response rises linearly as the lactate concentration increases from 0 to 20 mM in both potentiostat devices. Current response rises as the concentration increases from 0 mM to 25 mM. Sensor response reaches to 90% of its final steady value within 60 seconds (response time).

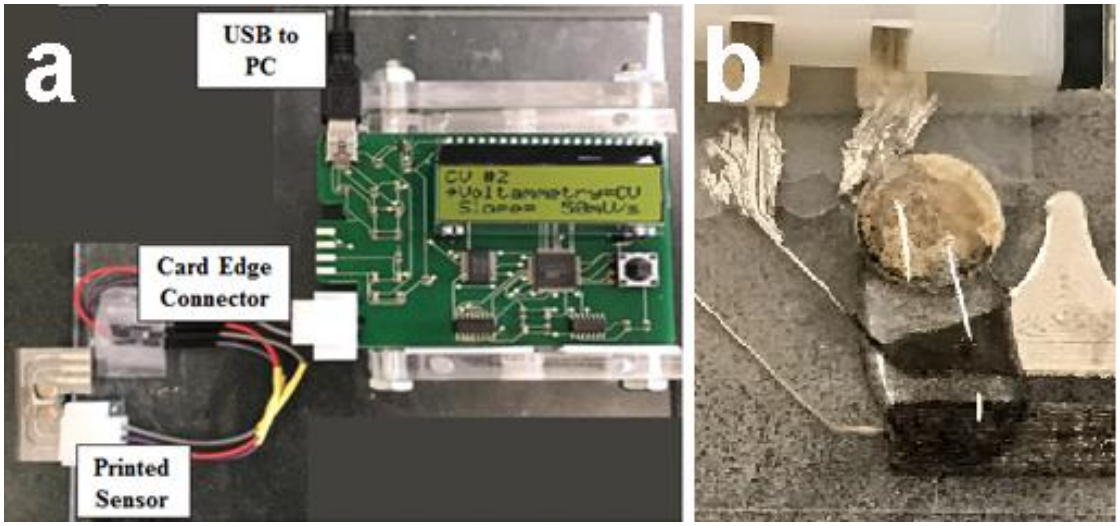

Figure 4.4. (a) test setup for 3D-PCB potentiostat prototype with lactate sensor (b) zoom in the image of drop cast of lactate acid solution on the sensor

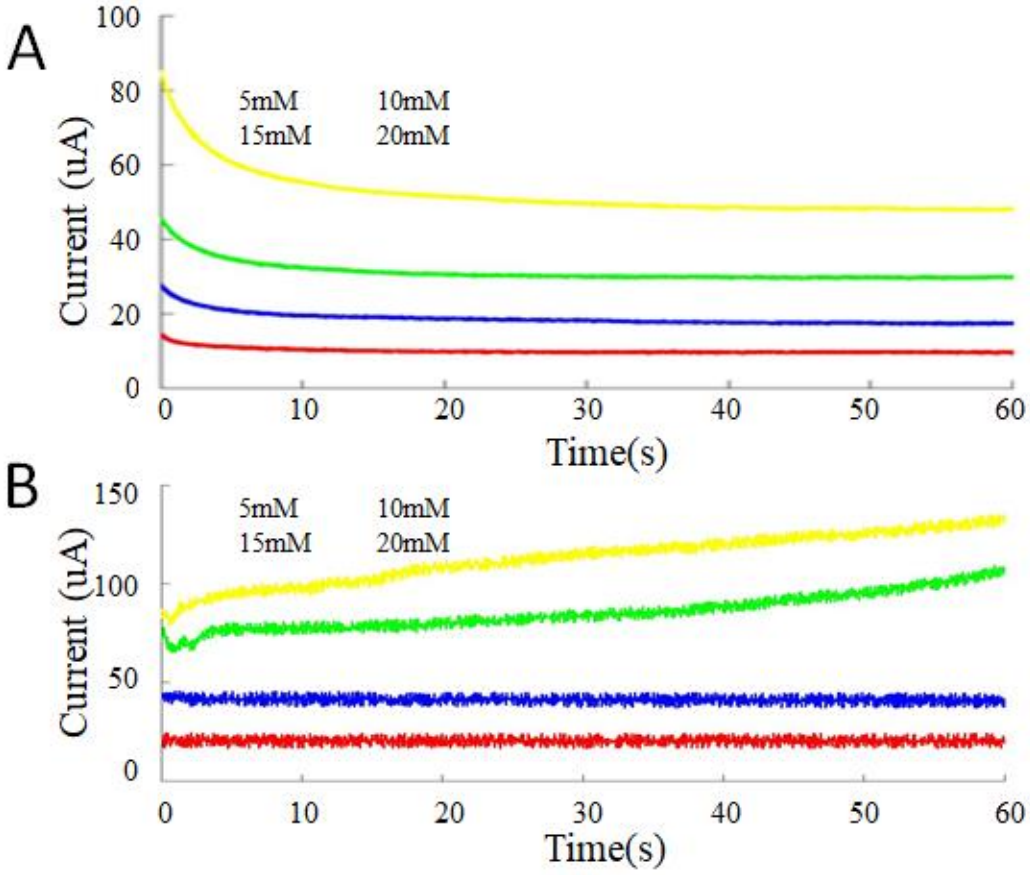

Figure 4.5. Amperometric measurements within lactate solutions. (a) proposed potentiostat design using conventional PCB fabrication method (b) proposed potentiostat design using a 3D printing method

Obviously, the measured currents from 3D PCB potentiostat are higher than the current from potentiostat on conventional PCB, as well as the signal noise. There are two reasons: Firstly, sintered AgNP's electrical conductivity is lower than coppers'. Therefore, there is more resistivity lost on the 3D PCB potentiostat along the circuit trace. When measuring the same amount of driving current, the converted voltage is larger due to the large resistance. Secondly, unlike the copper pad which IC components can be soldered homogeneously, AgNP pad has poorer solder ability. Poorly soldered structures between IC component pins and 3D PCB pad increase the resistivity lost significantly as well. Therefore, minimizing the resistivity lost along the 3D PCB trace and solder structure can deliver better measurement performance.

Chapter 5.

Conclusion and Future Work

5.1. Conclusion

The primary purpose of this work was to investigate and demonstrate the use of 3D printing technology to fabricate an electrochemical device combined with 3D printed potentiostat PCB, along with a flexible lactate biosensor for noninvasive continuous lactate measurement.

- 3D printing technology integration

The main techniques of 3D printing were studied, each advance and limitations in the different fabricating processes were discussed. Direct Ink Writing (DIW) was selected as the best 3D printing method to fabricate PCB and sensor. A novel 3D ink printer(V-ONE) was utilized as the PCB printing platform. A pure additive manufacture procedure demonstrates the ability to print single layer double sides PCB by dispensing a high viscosity AgNP ink. Printing parameters were investigated. Thus this 3D PCB printing platform can generate PCBs which meet most design standard compared with traditional PCBs. The proposed PCB 3D printing method by printing silver ink to generate circuit significantly accelerate the fabrication process of conventional electronic PCB. The lead time for electronics prototyping can be reduced to hours.

- Development of Potentiostat

A functional potentiostat was developed base on 'CheapStat' open source structure. The circuit was re-designed with the addition of trans-impedance amplifier as the electrochemical current converter for better sensitivity and accuracy. PCB layout was simplified as lean as possible with only necessary ICs for CV and amperometry functions. Two potentiostats were fabricated using both conventional method and proposed 3D printing method for the purpose of comparison.

- 3D printing of sensor electrode

Sensor electrode was fabricated using 3D printing technique. The steps followed towards the development of the concept and fabrication of flexible sensing platform for lactate monitoring. All three electrodes were fabricated on PET substrate using silver nanoparticle.

- Demonstration of 3D printed electrochemical system

A fully 3D printed sensor and sensor module system with printed PCB-based potentiostat has been demonstrated. The printed lactate biosensor shows a linear amperometric response linear dependence with lactate concentration of 1~20 mM/L during the in-vitro experiments. Integrated with the printed lactate biosensor, cyclic voltammetry and amperometric are demonstrated. Experimental results show that the performance of the 3D-PCB based potentiostat is reliable as that of conventionally fabricated PCB.

5.2. Future Works

This work was an attempt as to demonstrate the possibility of using 3D printing technology to fabricate PCB system for electrochemical applications. Future work aims to improve AgNP conduct ink material's electrical and mechanical property. Both analog and high frequency digital applications can be achieved when the resistivity reduction is minimized. Maximizing printing speed without compromising print quality will be a problem of interest, and it will involve developing an optimal printing sequence to minimize printing artifacts. In addition, usage of computational methods can optimize the fabrication accuracy and 3D PCB success rate. For example, developing an automatic drilling mechanism will improve the 3D printed PCB quality and reduce chance of fail. Flexible electronics circuit printing is another area of interest; the conductive ink was demonstrated using low sintering temperature. Thereby complex circuit could be printed not only on rigid board but also on a flexible substrate with multi-layer features.

References

[1] Hull, Charles W. "Apparatus for production of three-dimensional objects by stereolithography." U.S. Patent No. 4,575,330. 11 Mar. 1986.

[2] Singh, Rupinder. "Three dimensional printing for casting applications: A state of art review and future perspectives." Advanced Materials Research. Vol. 83. Trans Tech Publications, 2010.

[3] Lewis, Jennifer A., et al. "Direct ink writing of three-dimensional ceramic structures." Journal of the American Ceramic Society 89.12 (2006): 3599-3609.

[4] Barnatt, Christopher. 3D printing: the next industrial revolution. ExplainingTheFuture. com, 2013.

[5] Gooding, J. Justin. "Nanostructuring electrodes with carbon nanotubes: A review on electrochemistry and applications for sensing." Electrochimica Acta50.15 (2005): 3049-3060.

[6] Robertson, Christopher T. Printed circuit board designer's reference: basics. Prentice Hall Professional, 2004.

[7] Gross, Bethany C., et al. "Evaluation of 3D printing and its potential impact on biotechnology and the chemical sciences." (2014): 3240-3253.

[8] MacDonald, Eric, and Ryan Wicker. "Multiprocess 3D printing for increasing component functionality." Science 353.6307 (2016): aaf2093.

[9] Dimension, N. (2017). *3D PCB Printer Readiness Survey: The Results!*. [online] Nano-di.com. Available at: http://www.nano-di.com/blog/printer-readiness-survey-results-april-2016 [Accessed 7 Aug. 2017].

[10] Israel : Survey Uncovers High Costs, Risks Associated with Prototyping PCBs Off-Site.” MENA Report, Albawaba (London) Ltd., Apr. 2016.

[11] EETimes. (2017). *When 3D Printing Meets PCBs | EE Times*. [online] Available at: http://www.eetimes.com/author.asp?doc_id=1329449 [Accessed 7 Aug. 2017].

[12] Vadgama, P., et al. "The glucose enzyme electrode: is simple peroxide detection at a needle sensor acceptable?." *Hormone and metabolic research. Supplement series* 20 (1988): 20-22

[13] Parolo, Claudio, and Arben Merkoçi. "based nanobiosensors for diagnostics." *Chemical Society Reviews* 42.2 (2013): 450-457.

[14] Li, Huaqing, et al. "Multi-channel electrochemical detection system based on LabVIEW." *Information Acquisition, 2004. Proceedings. International Conference on*. IEEE, 2004.

[15] Gao, Wei, et al. "Fully integrated wearable sensor arrays for multiplexed in situ perspiration analysis." *Nature* 529.7587 (2016): 509-514.

[16] Zhao, Chen, Martin M. Thuo, and Xinyu Liu. "A microfluidic paper-based electrochemical biosensor array for multiplexed detection of metabolic biomarkers." *Science and technology of advanced materials* 14.5 (2013): 054402.

[17] Imani, Somayeh, et al. "A wearable chemical–electrophysiological hybrid biosensing system for real-time health and fitness monitoring." *Nature communications* 7 (2016): ncomms11650.

[18] Sanghavi, Bankim J., et al. "Nanomaterial-based electrochemical sensing of neurological drugs and neurotransmitters." *Microchimica Acta* 182.1-2 (2015): 1-41.

[19] Stević, Zoran, Zoran Andjelković, and Dejan Antić. "A New PC and LabVIEW package based system for electrochemical investigations." *Sensors* 8.3 (2008): 1819-1831.

[20] Cruz, Andres Felipe Diaz, et al. "A low-cost miniaturized potentiostat for point-of-care diagnosis." *Biosensors and Bioelectronics* 62 (2014): 249-254.

[21] MacDonald, Eric, and Ryan Wicker. "Multiprocess 3D printing for increasing component functionality." *Science* 353.6307 (2016): aaf2093.

[22] Abrar, Md Abu, et al. "Bendable Electro-chemical Lactate Sensor Printed with Silver Nano-particles." *Scientific reports* 6 (2016): 30565.

[23] Wang, Joseph. *Analytical electrochemistry*. John Wiley & Sons, 2006.pp. 29-42, 67-85.

[24] Chem.libretexts.org. (2016). [online] Available at: http://chem.libretexts.org/Textbook_Maps/Analytical_Chemistry_Textbook_Maps/Map%3A_Analytical_Chemistry_2.0_(Harvey)

[25] D. C. Harris, "Quantitative Chemical Analysis," pp. 270-320, 348-372, 2007.

[26] Zoski, Cynthia G., ed. *Handbook of electrochemistry*. Elsevier, 2006.

[27] Community.asdlib.org. (2017). *Reference Electrodes | Image and Video Exchange Forum*. [online] Available at: http://community.asdlib.org/imageandvideoexchangeforum/2013/07/31/reference-electrodes [Accessed 8 Aug. 2017].

[28] Wang, Joseph. *Analytical electrochemistry*. John Wiley & Sons, 2006. 115-136, 165-185, 2006.

[29] Harvey, David. Modern analytical chemistry. Vol. 381. New York: McGraw-Hill, 2000.

[30] Cottrell, F. G. "Residual current in galvanic polarization regarded as a diffusion problem." Z. phys. Chem 42 (1903): 385-431.

[31] Clark, Leland C., and Champ Lyons. "Electrode systems for continuous monitoring in cardiovascular surgery." *Annals of the New York Academy of sciences* 102.1 (1962): 29-45.

[32] Mabeck, Jeffrey T., and George G. Malliaras. "Chemical and biological sensors based on organic thin-film transistors." *Analytical and bioanalytical chemistry* 384.2 (2006): 343-353.

[33] Baughman, Ray H., Anvar A. Zakhidov, and Walt A. De Heer. "Carbon nanotubes--the route toward applications." science 297.5582 (2002): 787-792.

[34] Evans, Dennis H., et al. "Cyclic voltammetry." (1983): 290.

[35] Wang, Joseph. "Electrochemical glucose biosensors." Chemical reviews 108.2 (2008): 814-825.

[36] YouTube. (2017). *A level. S.5 Immobilisation of enzymes Ms Cooper*. [online] Available at: https://www.youtube.com/watch?v=f163ohXmKEI [Accessed 8 Aug. 2017].

[37] Khan, M. A., A. A. Al-Jalal, and I. A. Bakhtiari. "'Decoking'of a'coked'zeolite catalyst in a glow discharge." *Analytical and bioanalytical chemistry* 377.1 (2003): 89-96.

[38] Nunes, Lázaro Alessandro Soares, and Denise Vaz de Macedo. "Saliva as a diagnostic fluid in sports medicine: potential and limitations." *Jornal Brasileiro de Patologia e Medicina Laboratorial* 49.4 (2013): 247-255.

[39] MacLean, Dave A., Jens Bangsbo, and Bengt Saltin. "Muscle interstitial glucose and lactate levels during dynamic exercise in humans determined by microdialysis." *Journal of Applied Physiology* 87.4 (1999): 1483-1490.

[40] Thomas, Nicole, Ilkka Lähdesmäki, and Babak A. Parviz. "A contact lens with an integrated lactate sensor." *Sensors and Actuators B: Chemical* 162.1 (2012): 128-134.

[41] Marek, E. M., et al. "Measurements of lactate in exhaled breath condensate at rest and after maximal exercise in young and healthy subjects." *Journal of breath research* 4.1 (2010): 017105.

[42] Biagi, Simona, et al. "Simultaneous determination of lactate and pyruvate in human sweat using reversed-phase high-performance liquid chromatography: a noninvasive approach." *Biomedical Chromatography*26.11 (2012): 1408-1415.

[43] Derbyshire, Philip J., et al. "Lactate in human sweat: a critical review of research to the present day." *The Journal of Physiological Sciences* 62.6 (2012): 429-440.

[44] Coyle, Shirley, et al. "On-body chemical sensors for monitoring sweat." *Wearable and autonomous biomedical devices and systems for smart environment*. Springer Berlin Heidelberg, 2010. 177-193.

[45] Kreyden, Oliver P., and E. Paul Scheidegger. "Anatomy of the sweat glands, pharmacology of botulinum toxin, and distinctive syndromes associated with hyperhidrosis." *Clinics in dermatology* 22.1 (2004): 40-44.

[46] Stefaniak, Aleksandr B., and Christopher J. Harvey. "Dissolution of materials in artificial skin surface film liquids." *Toxicology in Vitro* 20.8 (2006): 1265-1283.

[47] Harvey, Christopher J., Ryan F. LeBouf, and Aleksandr B. Stefaniak. "Formulation and stability of a novel artificial human sweat under conditions of storage and use." *Toxicology in Vitro* 24.6 (2010): 1790-1796.

[48] Sato, Kenzo, and Richard L. Dobson. "Glucose metabolism of the isolated eccrine sweat gland: II. The relation between glucose metabolism and sodium transport." *Journal of Clinical Investigation* 52.9 (1973): 2166.

[49] Green, J. M., et al. "Sweat lactate response between males with high and low aerobic fitness." *European journal of applied physiology* 91.1 (2004): 1-6.

[50] Romero, Marcelo Ricardo, et al. "Amperometric biosensor for direct blood lactate detection." *Analytical chemistry* 82.13 (2010): 5568-5572.

[51] Ambrosi, Adriano, and Martin Pumera. "3D-printing technologies for electrochemical applications." *Chemical Society Reviews* 45.10 (2016): 2740-2755.

[52] Crump, S. Scott. "Apparatus and method for creating three-dimensional objects." U.S. Patent No. 5,121,329. 9 Jun. 1992.

[53] Wegst, Ulrike GK, et al. "Bioinspired structural materials." *Nature materials*14.1 (2015): 23-36.

[54] Zhu, Cheng, et al. "Highly compressible 3D periodic graphene aerogel microlattices." *Nature communications* 6 (2015): 6962.

[55] Hull, Charles W. "Apparatus for production of three-dimensional objects by stereolithography." U.S. Patent No. 4,575,330. 11 Mar. 1986.

[56] Bogue, Robert. "3D printing: the dawn of a new era in manufacturing?." *Assembly Automation* 33.4 (2013): 307-311.

[57] He, Yong, et al. "Developments of 3D printing microfluidics and applications in chemistry and biology: a review." *Electroanalysis* 28.8 (2016): 1658-1678.

[58] Choi, Jae-Won, et al. "Fabrication of 3D biocompatible/biodegradable micro-scaffolds using dynamic mask projection microstereolithography." *Journal of Materials Processing Technology* 209.15 (2009): 5494-5503.

[59] Feygin, Michael. "Apparatus and method for forming an integral object from laminations." U.S. Patent No. 4,752,352. 21 Jun. 1988.

[60] Rosen, David, and Lee Weiss. "Layered manufacturing: current status and future trends." *Ann, Arbor* 1001 (2001): 48109.

[61] Deckard, Carl R. "Method and apparatus for producing parts by selective sintering." U.S. Patent No. 4,863,538. 5 Sep. 1989.

[62] Ko, Seung H., et al. "All-inkjet-printed flexible electronics fabrication on a polymer substrate by low-temperature high-resolution selective laser sintering of metal nanoparticles." *Nanotechnology* 18.34 (2007): 345202.

[63] Gothait, Hanan. "Apparatus and method for three dimensional model printing." U.S. Patent No. 6,259,962. 10 Jul. 2001..

[64] Muth, Joseph T., et al. "Embedded 3D printing of strain sensors within highly stretchable elastomers." *Advanced Materials* 26.36 (2014): 6307-6312.

[65] Park, Yong-Lae, Bor-Rong Chen, and Robert J. Wood. "Design and fabrication of soft artificial skin using embedded microchannels and liquid conductors." *IEEE Sensors Journal* 12.8 (2012): 2711-2718.

[66] Frutiger, Andreas, et al. "Capacitive soft strain sensors via multicore–shell fiber printing." *Advanced Materials* 27.15 (2015): 2440-2446.

[67] Saari, Matt, et al. "Fabrication and Analysis of a Composite 3D Printed Capacitive Force Sensor." *3D Printing and Additive Manufacturing* 3.3 (2016): 136-141

[68] Suaste-Gómez, Ernesto, et al. "Developing an ear prosthesis fabricated in polyvinylidene fluoride by a 3D printer with sensory intrinsic properties of pressure and temperature." *Sensors* 16.3 (2016): 332.

[69] Lin, Ying-Kai, et al. "Using Three-Dimensional Printing Technology to Produce a Novel Optical Fiber Bragg Grating Pressure Sensor." *Sens. Mater*28 (2016): 389-394.

[70] Rivadeneyra, Almudena, et al. "Improved manufacturing process for printed cantilevers by using water removable sacrificial substrate." *Sensors and Actuators A: Physical* 235 (2015): 171-181.

[71] Macdonald, Eric, et al. "3D printing for the rapid prototyping of structural electronics." *IEEE Access* 2 (2014): 234-242.

[72] Krachunov, Sammy, and Alexander J. Casson. "3D Printed Dry EEG Electrodes." *Sensors* 16.10 (2016): 1635.

[73] Cho, Sung-Joon, et al. "3D printed multi-channel EEG sensors for zebrafish." *SENSORS, 2015 IEEE*. IEEE, 2015.

[74] Adams, Jacob J., et al. "Conformal printing of electrically small antennas on three-dimensional surfaces." *Advanced Materials* 23.11 (2011): 1335-1340.

[75] Nassar, I., H. Tsang, and T. Weller. "3D printed wideband harmonic transceiver for embedded passive wireless monitoring." *Electronics Letters*50.22 (2014): 1609-1611.

[76] Nassar, Ibrahim T., et al. "A High-Efficiency, Miniaturized Sensor Node With 3-D Machined-Substrate Antennas for Embedded Wireless Monitoring." *IEEE Sensors Journal* 15.9 (2015): 5036-5044.

[77] Lopez, Aida Garcia, Rohit Chandra, and Anders J. Johansson. "Optimization and fabrication by 3D printing of a volcano smoke antenna for UWB applications." *Antennas and Propagation (EuCAP), 2013 7th European Conference on*. IEEE, 2013.

[78] Mandon, Céline A., Loïc J. Blum, and Christophe A. Marquette. "Adding biomolecular recognition capability to 3D printed objects." *Analytical chemistry* 88.21 (2016): 10767-10772.

[79] Lind, Johan U., et al. "Instrumented cardiac microphysiological devices via multimaterial three-dimensional printing." *Nature materials* 16.3 (2017): 303-308.

[80] Sauerbrunn, Elizabeth, et al. "Thermal imaging using polymer nanocomposite temperature sensors." *physica status solidi (a)* 212.10 (2015): 2239-2245.

[81] Wickberg, Andreas, et al. "Three-dimensional micro-printing of temperature sensors based on up-conversion luminescence." *Applied Physics Letters*106.13 (2015): 133103.

[82] Li, Bo, et al. "Inkjet printed chemical sensor array based on polythiophene conductive polymers." *Sensors and Actuators B: Chemical* 123.2 (2007): 651-660.

[83] Kulkarni, Milind V., et al. "Ink-jet printed conducting polyaniline based flexible humidity sensor." *Sensors and Actuators B: Chemical* 178 (2013): 140-143.

[84] Song, Edward, et al. "Inkjet printing of conductive polymer nanowire network on flexible substrates and its application in chemical sensing." *Microelectronic Engineering* 145 (2015): 143-148.

[85] Naydenova, Izabela, et al. "Hybrid sensors fabricated by inkjet printing and holographic patterning." *Chemistry of Materials* 27.17 (2015): 6097-6101.

[86] Chen, Pochiang, et al. "Inkjet printing of single-walled carbon nanotube/RuO 2 nanowire supercapacitors on cloth fabrics and flexible substrates." *Nano Research* 3.8 (2010): 594-603.

[87] Yang, Li, et al. "A novel conformal RFID-enabled module utilizing inkjet-printed antennas and carbon nanotubes for gas-detection applications." *IEEE Antennas and Wireless Propagation Letters* 8 (2009): 653-656.

[88] Kim, Jiseok, and Woo Soo Kim. "Stretching silver: Printed metallic nano inks in stretchable conductor applications." *IEEE Nanotechnology Magazine* 8.4 (2014): 6-13.

[89] Macdonald, Eric, et al. "3D printing for the rapid prototyping of structural electronics." *IEEE Access* 2 (2014): 234-242.

[90] Franke, Jörg, ed. *Three-Dimensional Molded Interconnect Devices (3D-MID): Materials, Manufacturing, Assembly and Applications for Injection Molded Circuit Carriers*. Carl Hanser Verlag GmbH Co KG, 2014.

[91] Palmer, J. A., P. Yang, and D. W. Davis. *Rapid prototyping of high density circuitry*. Society of Manufacturing Engineers, 2000.

[92] Medina, Frank, et al. "Hybrid manufacturing: integrating direct-write and stereolithography." *Proceedings of the 2005 solid freeform fabrication* (2005): 129-143.

[93] Navarrete, Misael, et al. *Integrated layered manufacturing of a novel wireless motion sensor system with GPS*. TEXAS UNIV AT EL PASO WM KECK CENTER FOR 3D INNOVATION, 2007.

[94] Lopes, Amit, et al. "Expanding rapid prototyping for electronic systems integration of arbitrary form." *17th Annual Solid Freeform Fabrication Symposium, University of Texas at Austin, Austin, TX, Aug*. 2006.

[95] Zhou, Nanjia, et al. "Gigahertz Electromagnetic Structures via Direct Ink Writing for Radio-Frequency Oscillator and Transmitter Applications." *Advanced Materials* 29.15 (2017).

[96] Siggard, Erik J., et al. "Structurally embedded electrical systems using ultrasonic consolidation (UC)." *Proceedings of the 17th solid freeform fabrication symposium*. 2006.

[97] Nair, V., et al. "3D stacked embedded component system-in-package for wearable electronic devices." *Radio and Wireless Symposium (RWS), 2017 IEEE*. IEEE, 2017.

[98] Espalin, David, et al. "3D Printing multifunctionality: structures with electronics." *The International Journal of Advanced Manufacturing Technology* 72.5-8 (2014): 963-978.

[99] Olivas, Richard, et al. "Structural electronics through additive manufacturing and micro-dispensing." *International Symposium on Microelectronics*. Vol. 2010. No. 1. International Microelectronics Assembly and Packaging Society, 2010.

[100] Munakata, Riki. "Cubesat design specification rev. 12." *The CubeSat Program, California Polytechnic State University* 1 (2009).

[101] Boschetto, A., V. Giordano, and F. Veniali. "Surface roughness prediction in fused deposition modelling by neural networks." *International Journal of Advanced Manufacturing Technology* 67 (2013).

[102] Malone, Evan, and Hod Lipson. "Freeform fabrication of ionomeric polymer-metal composite actuators." *Rapid Prototyping Journal* 12.5 (2006): 244-253..

[103] Malone, Evan, Megan Berry, and Hod Lipson. "Freeform fabrication and characterization of Zn-air batteries." *Rapid Prototyping Journal* 14.3 (2008): 128-140.

[104] Janaki Ram, G. D., et al. "Use of ultrasonic consolidation for fabrication of multi-material structures." *Rapid Prototyping Journal* 13.4 (2007): 226-235.

[105] Park, Jae Sung, Mohamad Rezaei, and Woo Soo Kim. "Sustained Percolation in Stretched Silver Nanowire Networks for Stretchable Inter-Connection Applications." *Advanced Engineering Materials* 16.7 (2014): 905-908.

[106] Stratasys.com. (2017). *Smart Parts: Additive Manufacturing for Integrated Electro-mechanical Devices | Stratasys*. [online] Available at: http://www.stratasys.com/resources/webinars/smart-parts.aspx [Accessed 8 Aug. 2017].

[107] Paulsen, Jason A., et al. "Printing conformal electronics on 3D structures with Aerosol Jet technology." *Future of Instrumentation International Workshop (FIIW), 2012*. IEEE, 2012.

[108] Singh, Yadunath. "Electrical resistivity measurements: a review." *International journal of modern physics: Conference series*. Vol. 22. World Scientific Publishing Company, 2013.

[109] Rowe, Aaron A., et al. "CheapStat: an open-source,“Do-It-Yourself” potentiostat for analytical and educational applications." *PloS one* 6.9 (2011): e23783.

[110] Robertson, Christopher T. *Printed circuit board designer's reference: basics*. Prentice Hall Professional, 2004.

Appendix A.

Early electrodes design setup

First attempt of printing electrode on epoxy board without using card edge connection design. Thin copper wires were manually soldered on printed electrodes. The high temperature from solder gun damaged most electrodes

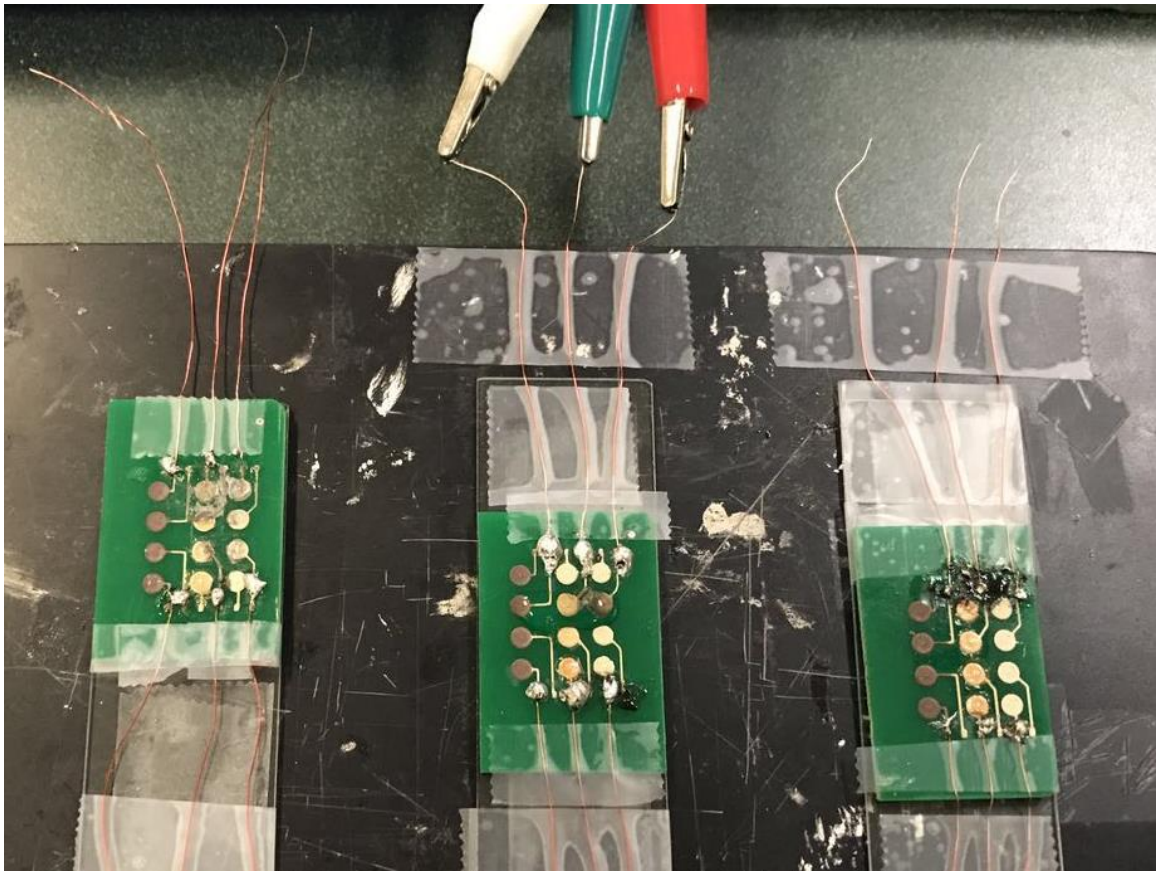

Appendix B.

Programming Setup

To program the AVR microcontroller, original source file of C was converted to a hex file using WinAVR. WinAVR is a suite of executable, open source software development tools for the Atmel AVR series of RISC microprocessors hosted on the Windows platform. It includes the GNU GCC compiler for C and C++. This hex is the firmware code, in order to burn the firmware into the MCU, a AVR mkII programmer was connected between laptop and the MCU using DPI mode. The connection is shown in bottom figure. Pin 33,34,8,38 on the MCU was PDI_DATA,PDI_CLK,VCC, and GND respectively.

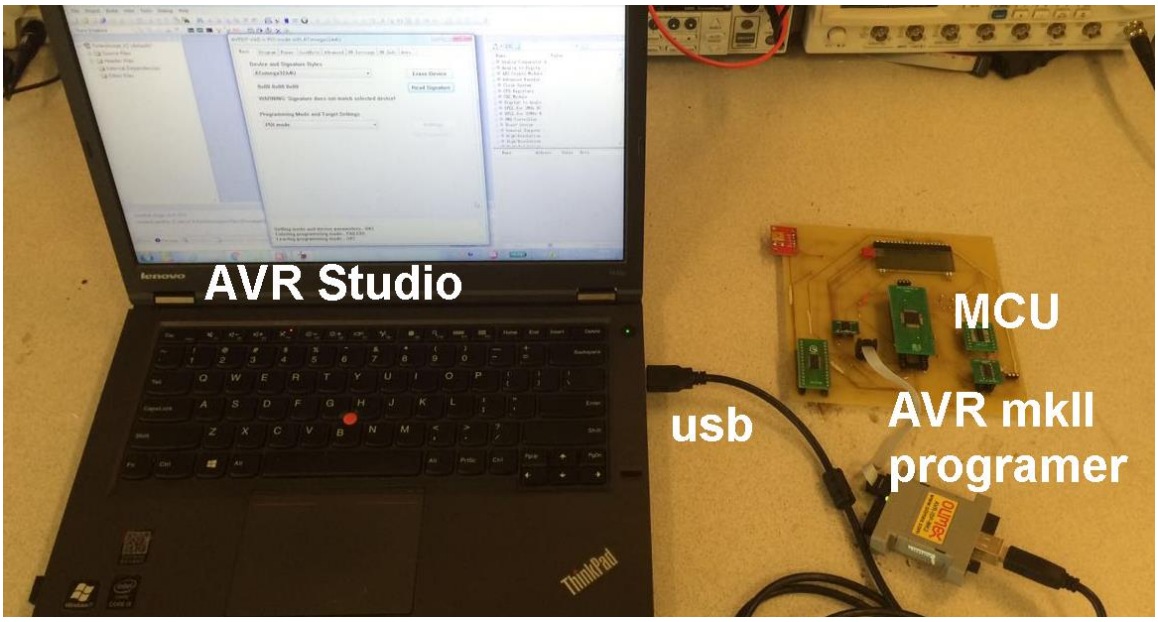

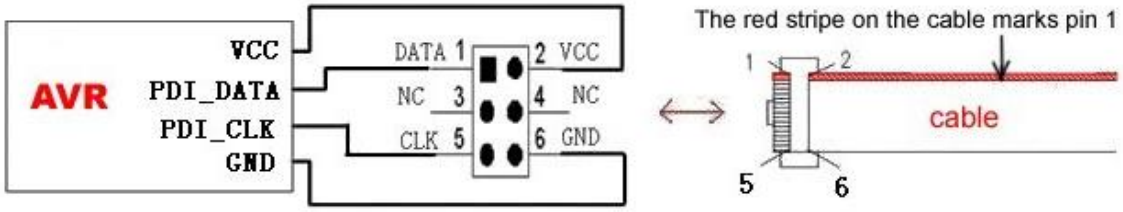

Appendix C.

Potentiostat Circuit Design Detail

Part 1

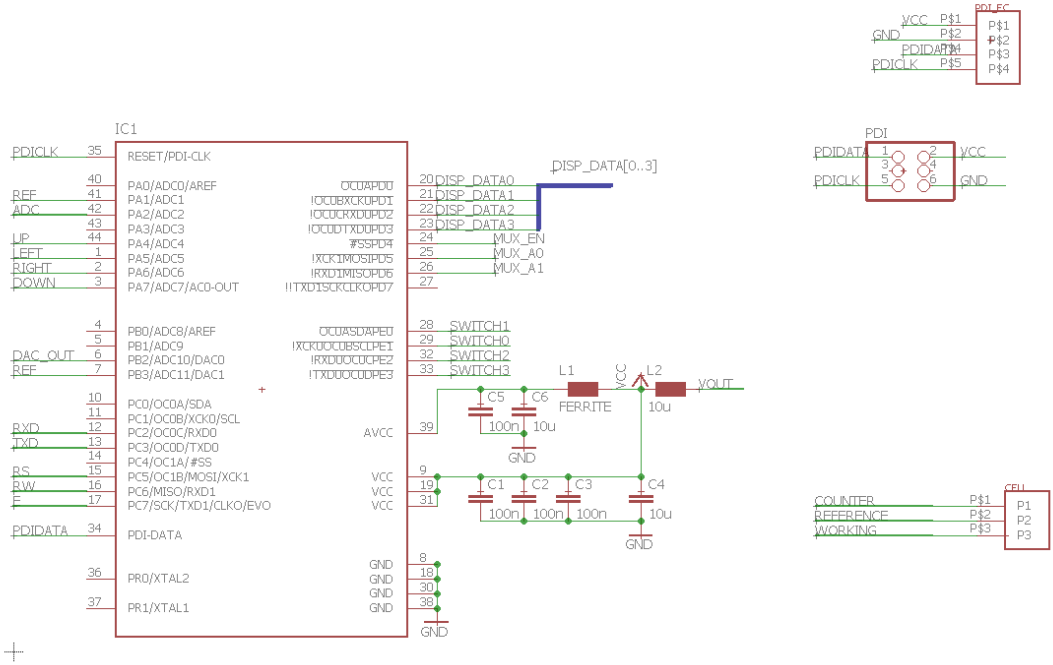

Part 2

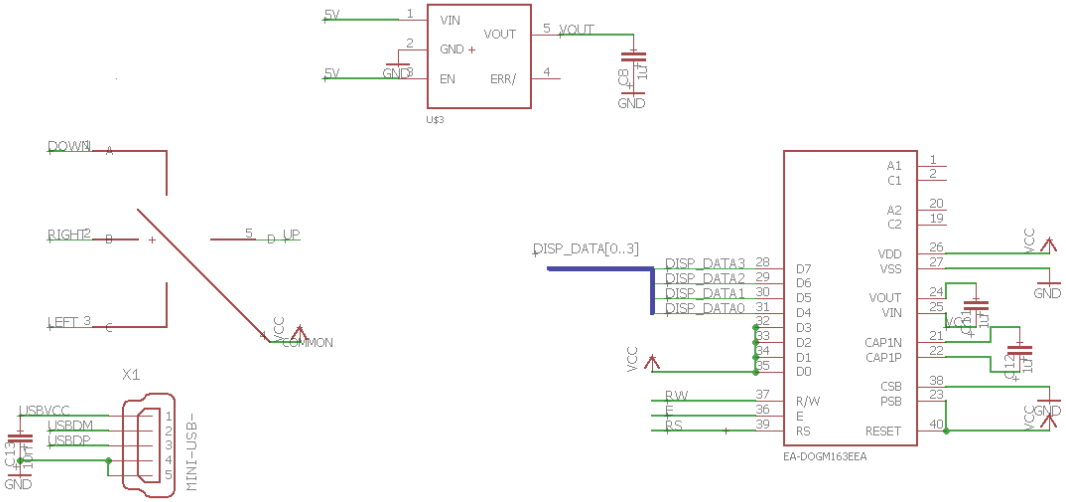

Part 3

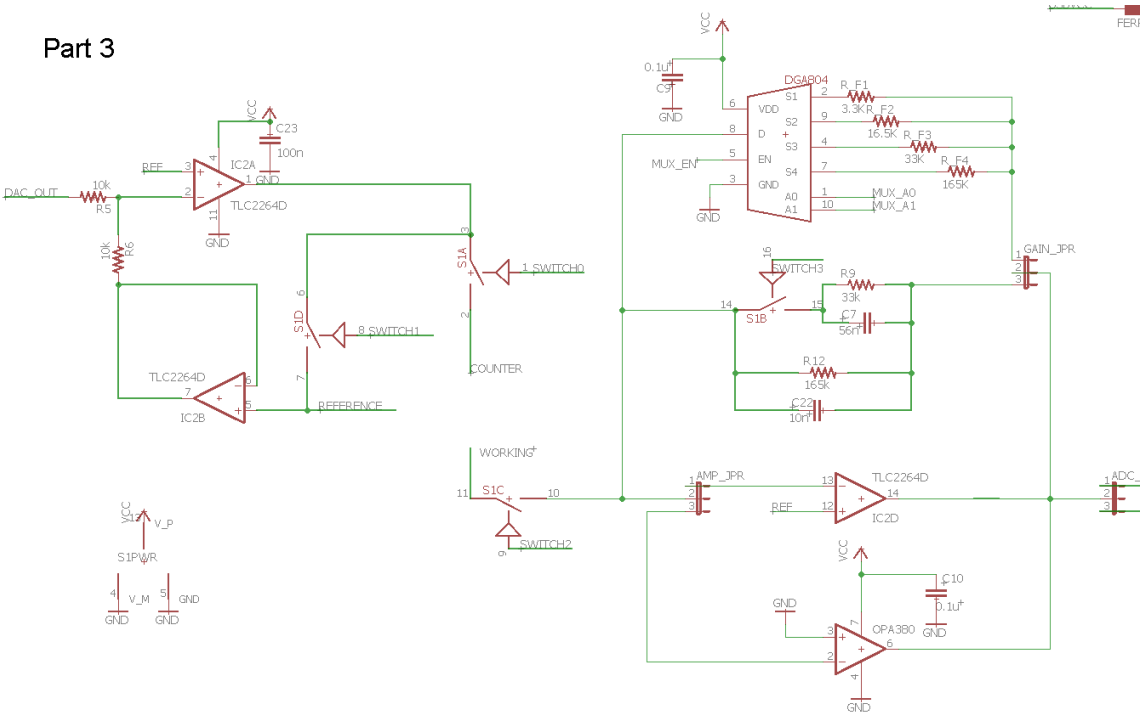
VCC
C23
100n
REF
IC2A
TLC2264D
GND
DAC_OUT
10k
R5
10k
R6
S1A
1 SWITCH0
S1D
8 SWITCH1
COUNTER
TLC2264D
IC2B
REFERENCE
WORKING
S1C
10
SWITCH2
V_P
S1PWR
V_M
GND
0.1u
C3
DGA804
R_F1
3.3K
R_F2
16.5K
R_F3
33K
R_F4
165K
MUX_EN
MUX_A0
MUX_A1
SWITCH3
S1B
R9
33k
C7
56n
R12
165K
C22
10n
GAIN_JPR
AMP_JPR
TLC2264D
IC2D
REF
ADC_
C10
0.1u
OPA380
GND

Part 4

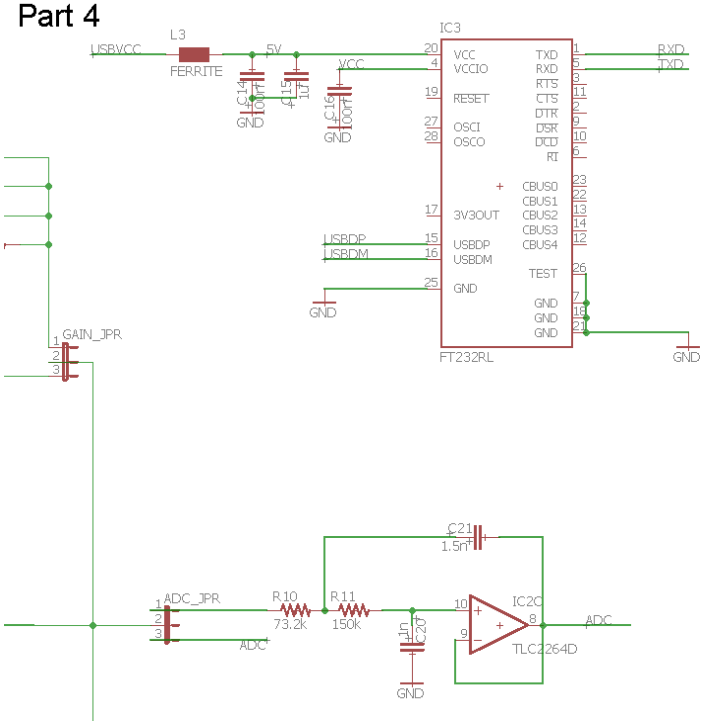
IC3
USBVCC
L3
FERRITE
5V
VCC
C14
10n
C15
1u
C16
100n
VCC
VCCIO
RESET
OSCI
OSCO
3V3OUT
USBDP
USBDM
GND
TXD
RXD
RTS
CTS
DTR
DSR
DCD
RI
CBUS0
CBUS1
CBUS2
CBUS3
CBUS4
TEST
GND
FT232RL
RXD
TXD
GND
GAIN_JPR
C21
1.5n
ADC_JPR
R10
73.2k
R11
150k
C20
1n
IC2C
TLC2264D
ADC
ADC
GND

Appendix D.

Microcontroller code

```
#define F_CPU 2000000UL //CPU frequency
#define TIMER TCC0 //timer to use
#define DAC_CONINTVAL DAC_CONINTVAL_1CLK_gc //DAC settings
#define DAC_REFRESH DAC_REFRESH_16CLK_gc
#define ADC_PRESCALER ADC_PRESCALER_DIV8_gc //ADC sampling speed
#define ADC_OFSET 0
#define EEPROM_SIZE 1024 //in bytes
#define PROFILES_LENGTH 11 //max number of profiles, limited by memory
#define SWV_BUFFER_SIZE 16 //must be <=16
#define SWV_MAX_DATAPOINTS 1000
#define CV_BUFFER_SIZE 16 //must be <=16
#define CV_MAX_DATAPOINTS 1500
#define LSV_BUFFER_SIZE 16 //must be <=16
#define LSV_MAX_DATAPOINTS 1500
#define CA_MAX_DATAPOINTS 1500
#define ACV_POINTSPERCYCLE 50
//#define DEBUG
//#define DUBUGSIZE
//#define DEBUG_INDEX_STOP 1000
//user interface
#define SWV 0
#define CV 1
#define ACV 2
#define LSV 3
#define CONSTVOLT 4
#define CA 5

#define PROFILE_SEL 0
#define PROFILE_OPT 1
#define PROFILE_TEST 2
#define PROFILE_EDIT 3
#define PROFILE_RESULTS 4
#define EDIT_NOSEL 0
#define EDIT_SEL 1
#define OPT_START 0
#define OPT_EDIT 1
#define RANGE_10UA 1
#define NGE_50UA 2
#define UP 0
#define LEFT 1
#define RIGHT 2
#define DOWN 3
#define INVALID 4
#define bit_get(p,m) ((p) & (m))
//structure to store the profile - 29 bytes
typedef struct {
        char name[15];
        uint8_t type;
        int16_t op1;
```

```
		int16_t op2;
		int16_t op3;
		int16_t op4	int16_t op5;
		int16_t op6;
		uint8_t curr_range;
	} profile;
	//profiles are located in both EEPROM and RAM
	profile EEMEM profilesEE[PROFILES_LENGTH];
	profile profiles[PROFILES_LENGTH];
	int buttonHandler(profile profiles[PROFILES_LENGTH], uint8_t* status, uint8_t*
profile_index, uint8_t* profile_opt_index, uint8_t* profile_edit_index, uint8_t*
profile_edit_sel,int16_t* length);
	int16_t SWV_test (char* name, int16_t freq, int16_t start, int16_t stop, int16_t height,
int16_t increment, uint8_t curr_range);
	int16_t CV_test (char* name, int16_t slope, int16_t start, int16_t stop, int16_t scans,
int16_t sample_rate, uint8_t curr_range);
	int16_t ACV_test (char* name, int16_t freq, int16_t height, int16_t cycles, int16_t start,
int16_t stop, int16_t incr, uint8_t curr_range);
	int16_t LSV_test (char* name, int16_t wait, int16_t start, int16_t stop, int16_t slope,
int16_t sample_rate, uint8_t curr_range);
	int16_t CONSTVOLT_test (char* name, int16_t voltage, int16_t time);
	int16_t CA_test (char* name, int16_t wait_time, int16_t step_voltage, int16_t step_width,
int16_t quiet_time, int16_t sample_rate, uint8_t steps, uint8_t curr_range);
	USART_data_t USART_data;
	void send_string(char* string);
	int main()
	{
		uint8_t status;
		uint8_t profile_index;
		uint8_t profile_opt_index;
		uint8_t profile_edit_index;
		uint8_t profile_edit_sel;
		uint8_t index;
		char temp_string[16];
		uint8_t i;
		int16_t length;
	PORTD.DIRSET = PIN4_bm;
		PORTD.PIN4CTRL = PORT_OPC_WIREDANDPULL_gc;
		PORTD.OUTSET = PIN4_bm;
		SPI_MasterInit(&spiMasterD,
			&SPIC,
			&PORTD,
			false,
			SPI_MODE_0_gc,
			SPI_INTLVL_OFF_gc,
			false,
			SPI_PRESCALER_DIV4_gc);*/
	//4 DIR SWITCH
		//setup pins as input
		PORTA.DIRCLR = PIN4_bm;
		PORTA.PIN4CTRL = PORT_OPC_PULLDOWN_gc;
		PORTA.DIRCLR = PIN5_bm;
		PORTA.PIN5CTRL = PORT_OPC_PULLDOWN_gc;
		PORTA.DIRCLR = PIN6_bm;
		PORTA.PIN6CTRL = PORT_OPC_PULLDOWN_gc;
		PORTA.DIRCLR = PIN7_bm;
```

```
		PORTA.PIN7CTRL = PORT_OPC_PULLDOWN_gc;
		//PORTE.INT0MASK = 0;
	//DAC
		DAC_DualChannel_Enable( &DACB,DAC_REFSEL_AVCC_gc,false,DAC_CONI
NTVAL,DAC_REFRESH);
		//1.65V reference
		while (DAC_Channel_DataEmpty(&DACB, CH1) == false) {}
			DAC_Channel_Write(&DACB,2048,CH1);
		//intitial
		while (DAC_Channel_DataEmpty(&DACB, CH0) == false) {}
			DAC_Channel_Write(&DACB,2048,CH0);
	//USART
		//TX as output
		PORTC.DIRSET = PIN3_bm;
		//RX as input
		PORTC.DIRCLR = PIN2_bm;
		USART_InterruptDriver_Initialize(&USART_data, &USARTC0,
USART_DREINTLVL_LO_gc);
		// USARTD0, 8 Data bits, No Parity, 1 Stop bit.
		USART_Format_Set(&USARTC0, USART_CHSIZE_8BIT_gc,
USART_PMODE_DISABLED_gc, false);
			//enable interrupts
		USART_RxdInterruptLevel_Set(&USARTC0, USART_RXCINTLVL_LO_gc);
		//BUAD RATE to 9600
		USART_Baudrate_Set(&USARTC0, 12 , 0);
		USART_Rx_Enable(&USARTC0);
		USART_Tx_Enable(&USARTC0);
	//ADC
	// Move stored calibration values to ADC A.
		ADC_CalibrationValues_Load(&ADCA);
	// Set up ADC A to have signed conversion mode and 12 bit resolution.
		ADC_ConvMode_and_Resolution_Config(&ADCA, ADC_ConvMode_Signed,
ADC_RESOLUTION_12BIT_gc);
	// Set sample rate.
		ADC_Prescaler_Config(&ADCA, ADC_PRESCALER);
	// Set reference voltage on ADC A to be VCC internal
		ADC_Reference_Config(&ADCA, ADC_REFSEL_VCC_gc);
		//configure input mode to
differentialADC_Ch_InputMode_and_Gain_Config(&ADCA.CH0,ADC_CH_INPUTMODE_DIFF_g
c,ADC_DRIVER_CH_GAIN_NONE);ADC_Ch_InputMode_and_Gain_Config(&ADCA.CH1,ADC_
CH_INPUTMODE_DIFF_gc,ADC_DRIVER_CH_GAIN_NONE);
		//configure pinsADC_Ch_InputMux_Config(&ADCA.CH0,
ADC_CH_MUXPOS_PIN0_gc,
ADC_CH_MUXNEG_PIN1_gc);ADC_Ch_InputMux_Config(&ADCA.CH1,
ADC_CH_MUXPOS_PIN2_gc, ADC_CH_MUXNEG_PIN1_gc);
		//enable adc
		ADC_Enable(&ADCA)
		//settings in lcdconf.h
		lcdInit();
		lcdInit();
		lcdClear();
		lcdHome();
		lcdPrintData("CheapStat",9);
		_delay_ms(1000);
	//USER INTERFACE
		status = PROFILE_SEL;
```

```
		profile_index = 0;
		profile_opt_index = OPT_START;
		profile_edit_index = 0;
		profile_edit_sel = EDIT_NOSEL;
	//PROFILES (EEPROM)
	//copy profiles from EEPROM to SRAM
		for(i = 0; i < PROFILES_LENGTH; i++)
	eeprom_read_block((void*)&(profiles[i]), (const void*)&(profilesEE[i]), sizeof(profile));

		//INTERRUPTS
		////////////////////////////////
		PMIC.CTRL |= PMIC_LOLVLEX_bm;
		sei();
		//END INITIALIZATION
	//////////////////////////////////////MAIN LOOP/////////////////////////////////////////////////
	while(1){
	int16_t CV_test (char* name, int16_t slope, int16_t start, int16_t stop, int16_t scans,
int16_t sample_rate, uint8_t curr_range){
		uint16_t step_time;
		uint16_t steps_per_sample;
		uint16_t steps_taken;
		uint16_t ramps;
		uint16_t samples;
		uint16_t i,j,k;
		bool up;
		int16_t current_DAC, min_DAC, max_DAC;
	//storing ADC results
		int16_t current[CV_MAX_DATAPOINTS];
		int16_t result_buffer[CV_BUFFER_SIZE];
	//check limits
		if(start<-1600 || start>1600 || stop<-1600 || stop>1600 || slope>5000 || slope<10 ||
sample_rate<1 || sample_rate>1600){
			lcdClear();
			lcdHome();
			lcdPrintData("outside limits",14);
			return -1;
		}
		//determine starting direction and calculate
		if((stop-start)>0)
		{
			up=true;
			min_DAC = (int16_t) (round(start*(4096.0/3300))+2048);
			max_DAC = (int16_t) (round(stop*(4096.0/3300))+2048);
		}
		else
		{
			up=false;
			max_DAC = (int16_t) (round(start*(4096.0/3300))+2048);
			min_DAC = (int16_t) (round(stop*(4096.0/3300))+2048);
		}

		ramps = 2*scans;

		steps_per_sample = (uint16_t) (round(sample_rate*(4096.0/3300)));

		samples = 2*scans*((max_DAC-min_DAC)/steps_per_sample);
```

```
	if(samples > CV_MAX_DATAPOINTS)
	{
		lcdClear();
		lcdHome();
		lcdPrintData("too many data points",20);
		return -1;
	}

	//2,000,000 [cycles/sec] * 1/slope [sec/mV] * 3300/4096 [mv/index]
	if(slope > 30)
	{
		step_time = (uint16_t) (round(2000000*(1.0/slope)*(3300.0/4096)));
		TIMER.CTRLA = TC_CLKSEL_DIV1_gc;
	}
	else{
		step_time = (uint16_t) (round(500000*(1.0/slope)*(3300.0/4096)));
		TIMER.CTRLA = TC_CLKSEL_DIV4_gc;
	}


	if(up)
		current_DAC = min_DAC;
	else
		current_DAC = max_DAC;

	i = 0;
	j = 0;
	steps_taken = 0;
	k = 0;

	for(k = 0; k < CV_BUFFER_SIZE; k++)
		result_buffer[k] = 0;

	//change switches
	PORTE.OUTSET = PIN1_bm; //switch0
	PORTE.OUTSET = PIN2_bm; //switch2
	if(curr_range == RANGE_10UA)
		PORTE.OUTCLR = PIN3_bm; //switch3
	else
		PORTE.OUTSET = PIN3_bm; //switch3
	//_delay_ms(50);
	PORTE.OUTCLR = PIN0_bm; //switch1

	while (DAC_Channel_DataEmpty(&DACB, CH0) == false) {}
		DAC_Channel_Write(&DACB,current_DAC,CH0);
	_delay_ms(250);

while(1)
{
	//set DAC and trigger timer
	while (DAC_Channel_DataEmpty(&DACB, CH0) == false) {}
		DAC_Channel_Write(&DACB,current_DAC,CH0);
	TIMER.CNT = 0;

	//calculate next DAC value
```

```
		if(up)
			current_DAC++;
		else
			current_DAC--;

		//decision making
		if(up && current_DAC >= max_DAC)
		{
			up = false; //switch to going down
			ramps--;
			if(ramps==0)
				break;
		}
		else if(!up && current_DAC <= min_DAC)
		{
			up = true; //switch to going up
			ramps--;
			if(ramps==0)
				break;
		}

		current[i] = 0;
		//ADC measurements
		while(TIMER.CNT<step_time) {
			ADC_Ch_Conversion_Start(&ADCA.CH1);
			while(!ADC_Ch_Conversion_Complete(&ADCA.CH1) &&
TIMER.CNT<step_time) {}

			if(current[i] == 0)
				current[i] =
ADC_ResultCh_GetWord_Signed(&ADCA.CH1,ADC_OFFSET);
			else
				current[i] = (current[i] +
ADC_ResultCh_GetWord_Signed(&ADCA.CH1,ADC_OFFSET)) >> 1;
		}

		steps_taken++;
		if(steps_taken >= steps_per_sample)
		{
			steps_taken = 0;
			i++;
		}
	}

		PORTE.OUTSET = PIN0_bm; //switch1
		//PORTE.OUTCLR = PIN0_bm; //switch1
		PORTE.OUTCLR = PIN1_bm; //switch0
		PORTE.OUTCLR = PIN2_bm; //switch2
		PORTE.OUTCLR = PIN3_bm; //switch3
		current_DAC = 2048;
		while (DAC_Channel_DataEmpty(&DACB, CH0) == false) {}
			DAC_Channel_Write(&DACB,current_DAC,CH0);

		//start output to USB
		do{} while(!USART_IsTXDataRegisterEmpty(&USARTC0));
		USART_PutChar(&USARTC0, CV);
```

```
	for(j = 0; j < 15; j++)
	{
		do{} while(!USART_IsTXDataRegisterEmpty(&USARTC0));
		USART_PutChar(&USARTC0, name[j]);
	}
	do{} while(!USART_IsTXDataRegisterEmpty(&USARTC0));
	USART_PutChar(&USARTC0, slope>>8);
	do{} while(!USART_IsTXDataRegisterEmpty(&USARTC0));
	USART_PutChar(&USARTC0, slope);
	do{} while(!USART_IsTXDataRegisterEmpty(&USARTC0));
	USART_PutChar(&USARTC0, start>>8);
	do{} while(!USART_IsTXDataRegisterEmpty(&USARTC0));
	USART_PutChar(&USARTC0, start);
	do{} while(!USART_IsTXDataRegisterEmpty(&USARTC0));
	USART_PutChar(&USARTC0, stop>>8);
	do{} while(!USART_IsTXDataRegisterEmpty(&USARTC0));
	USART_PutChar(&USARTC0, stop);
	do{} while(!USART_IsTXDataRegisterEmpty(&USARTC0));
	USART_PutChar(&USARTC0, scans>>8);
	do{} while(!USART_IsTXDataRegisterEmpty(&USARTC0));
	USART_PutChar(&USARTC0, scans);
	do{} while(!USART_IsTXDataRegisterEmpty(&USARTC0));
	USART_PutChar(&USARTC0, sample_rate>>8);
	do{} while(!USART_IsTXDataRegisterEmpty(&USARTC0));
	USART_PutChar(&USARTC0, sample_rate);
	do{} while(!USART_IsTXDataRegisterEmpty(&USARTC0));
	USART_PutChar(&USARTC0, curr_range);
	do{} while(!USART_IsTXDataRegisterEmpty(&USARTC0));
	USART_PutChar(&USARTC0, i>>8);
	do{} while(!USART_IsTXDataRegisterEmpty(&USARTC0));
	USART_PutChar(&USARTC0, i);

	for(j = 0; j < i; j++)
	{
		do{} while(!USART_IsTXDataRegisterEmpty(&USARTC0));
		USART_PutChar(&USARTC0, current[j]>>8);
		do{} while(!USART_IsTXDataRegisterEmpty(&USARTC0));
		USART_PutChar(&USARTC0, current[j]);
	}

	do{} while(!USART_IsTXDataRegisterEmpty(&USARTC0));
		USART_PutChar(&USARTC0,CV);

	return i;
}
int16_t CONSTVOLT_test (char* name, int16_t voltage, int16_t time) {

	uint16_t elapsed;
	int16_t current_DAC;

	//check limits
	if(voltage<-1600 || voltage>1600 || time<0 || time>9999)
	{
		lcdClear();
		lcdHome();
		lcdPrintData("outside limits",14);
```

```
		return -1;
	}

	current_DAC = (int16_t) (round(voltage*(4096.0/3300))+2048);

	//init timer
	TIMER.CTRLA = TC_CLKSEL_DIV1024_gc;

	//change switches
	PORTE.OUTSET = PIN1_bm; //switch0
	PORTE.OUTSET = PIN2_bm; //switch2
	PORTE.OUTSET = PIN3_bm; //switch3
	PORTE.OUTCLR = PIN0_bm; //switch1

	//apply voltage
	while (DAC_Channel_DataEmpty(&DACB, CH0) == false) {}
		DAC_Channel_Write(&DACB,current_DAC,CH0);


	//start timer
	TIMER.CNT = 0;

	elapsed = 0;
	while(elapsed < time) {

		//wait for 1 sec
		while(TIMER.CNT<1953) {}

		//reset timer
		TIMER.CNT = 0;

		//increment elapsed
		elapsed++;

	}


	PORTE.OUTSET = PIN0_bm; //switch1
	PORTE.OUTCLR = PIN1_bm; //switch0
	PORTE.OUTCLR = PIN2_bm; //switch2
	PORTE.OUTCLR = PIN3_bm; //switch3

	current_DAC = 2048;
	while (DAC_Channel_DataEmpty(&DACB, CH0) == false) {}
		DAC_Channel_Write(&DACB,current_DAC,CH0);

	return elapsed;
}
```